UNIVERSITÀ DI PISA

Dipartimento di Fisica ”Enrico Fermi”

Corso di Laurea Magistrale in Fisica

Beam diagnostic and calibration tools for the MEGII experiment.

Relatori:

Prof.ssa Angela Papa

Candidato:

Giovanni Dal Maso

Matricola 531444

Anno Accademico 2019/2020

Contents

Introduction

In the framework of high energy physics there are two major approaches to research at accelerator facilities: the energy frontier, which aims to directly produce new physics events through direct or indirect detection of new particles; the intensity frontier, which aims to detect deviations from the theoretical values of physics quantities, such as branching ratios, due to beyond SM physics.

One of the most promising sectors to detect physics beyond Standard Model at the intensity frontier is CLFV (Charged Lepton Flavour Violation)[1, 2, 3].
The most stringent limit in this sector, and also the strongest bound on any forbidden particle decay, to date was set by the MEG collaboration on the $\mu^+ \rightarrow e^+\gamma$ decay at Paul Scherrer Institut (PSI), which produces the most intense low energy muon beam ($> \ 10^8$ μ/s): $\mathcal{B}(\mu^+ \rightarrow e^+\gamma) \ < 4.2 \times 10^{-13}$ (90% CL)[4].
Since 2013 the MEG collaboration have undertaken a major detector upgrade to increase the above sensitivity up to $5{\times}10^{-14}$[5]. In order to do so, among the others, it is important to measure the rate of stopped muons R_{μ^+} with high precision.

In this thesis I present the design, simulation and tests of two new fast beam monitoring tools based on plastic scintillator coupled to silicon photomultipliers (SiPMs) able to measure the most intense continuous muon beam in the world (up to $10^8\mu/s$). The simulations are based on GEANT4. A custom code have been written to include the response of the photosensors and the full electronics chain, up to the waveform digitizer, with a frequency up to 5 GSample/s. The reconstructed algorithms are based on the waveform analysis and are the same used for the real data. The first proof-of-principle as obtained during dedicated beam tests of both detectors working in the final conditions will be described, showing that expected performances can be achieved. The use of SiPMs lets the detector work in high magnetic field (here up to 1.25 T) without loss in performances:

- SciFi[5, 6, 7]: a scintillating fiber grid coupled at each end to a SiPM. It is a quasi non-invasive beam monitor and lets measure, online, beam shapes and beam rate higher than 10^8 μ/s. It is able to perform particle ID through energy deposit, if the particles to be monitored aren't minimum ionizing particles, or through Time Of Flight (TOF) measurements. SciFi is directly mounted along the beam line and it works in vacuum;
- MatriX: a scintillating crystal matrix coupled to SiPMs. It is a destructive beam monitor, designed to measure shapes and rates of narrower beams than the previous detector: in fact it will be used at the center of the MEGII magnet. It is able to perform particle ID either through energy deposit or TOF.

The typical exposure time is of the order of a few seconds.

In every experiment it is also important to monitor the status of the detectors and to have a data-driven check on the performances of the detector and a data-driven analysis near the signal region. In MEGII there are many ways to calibrate and monitor the apparatus. An important calibration source is the Charge EXchange reaction (CEX) p(π^-, π^0)n[5] used to calibrate the Liquid Xenon calorimeter: the π^0 decays in two photons which are monochromatic in the rest frame of the π^0 but not in the laboratory frame, where energies are uniformly distributed between 54.9 and 82.9 MeV. Cutting on the angle between the two photons in the laboratory frame it is possible to tag the two photons and then measure events with energies near the MEGII signal region ($\sim$52.8 MeV).
For this calibration method it is necessary to change from a muon beam to a pion beam, optimized with its dedicated target, a Liquid Hydrogen one. The Liquid Hydrogen target is used to calibrate the MEGII Liquid Xenon calorimeter through the CEX reaction. Another part of my work consisted in evaluating the performances of the new Liquid Hydrogen target via detailed Monte Carlo simulation based on GEANT4.

The analysis of the simulations output is always performed using the ROOT toolkit routines for minimization[8].

Chapter 1

The MEGII Experiment

The MEGII experiment aims to detect the decay $\mu^+ \to e^+\gamma$, which is forbidden in the Standard Model (massless neutrinos) of particle physics. In the following chapter I will briefly introduce the theoretical framework of Charged Lepton Flavour Violation (CLFV) and the experimental set-up of the MEGII experiment.

1.1 The Standard Model

The Standard Model of particle physics (SM) is the most accurate and predictive theory to date, in the frame of particle interactions. It is a gauge theory based on the group SU(3)$_C\times$ SU(2)$_L\times$ U(1)$_Y$[9]: the group SU(2)$_L\times$U(1)$_Y$ describes the electroweak interaction; the group SU(3)$_C$ describes the strong interactions.

The theory is composed of 25 elementary fields:

- 12 fermions: these are the components of matter and are divided in leptons and quarks. The leptons interact only through electroweak interaction, and are divided in charged leptons (e, μ, τ) and neutral leptons (ν_e, ν_μ, ν_τ). The quarks interact through electroweak and strong interactions and are divided in up quarks (u, c, t), and down quarks (d, s, b). All of them are assumed to be massless.

- 12 bosons: these are the mediators of the interactions. They are: γ, Z, $W^\pm$, the mediators of the electroweak interaction; the 8 gluons (g) mediators of the strong interactions. All of them are assumed to be massless as well.

- Higgs: it is a scalar weak isospin doublet field responsible for the non-zero masses of the electroweak bosons and of the charged fermions.

Fig. 1.1 shows a list of the SM particles.

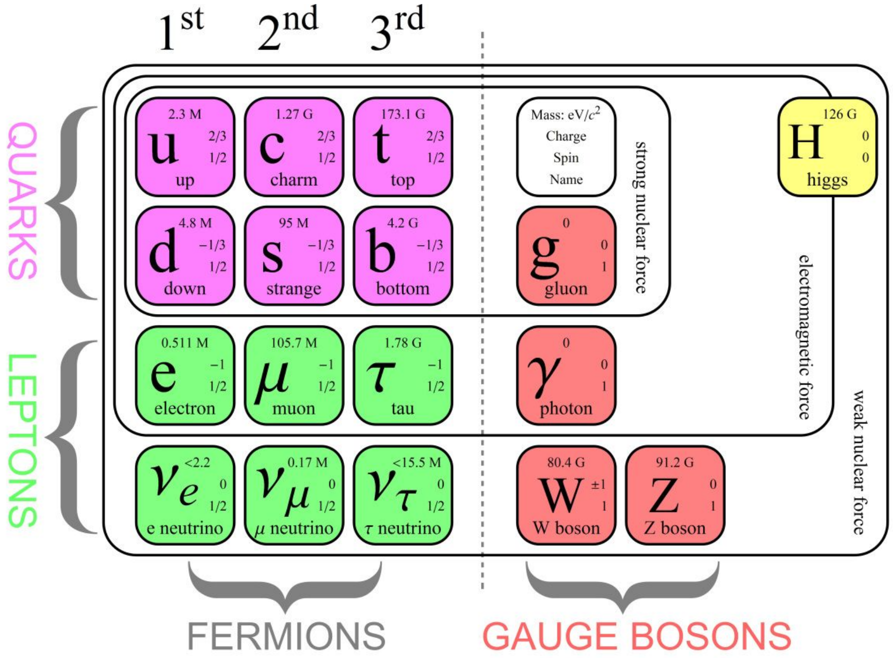

Figure 1.1: *Standard Model particles.*

The Lagrangian of the theory can be written as the sum of three contributions:

$$\begin{aligned}
\mathcal{L}_{SM} &= \mathcal{L}_{gauge} + \mathcal{L}_{Higgs} + \mathcal{L}_{Yukawa} \\
\mathcal{L}_{gauge} &= F^a_{\mu\nu} F^{a\mu\nu} + i\overline{\psi}\gamma^\mu D_\mu \psi + |D_\mu H|^2 \\
\mathcal{L}_{Higgs} &= \mu^2 H^\dagger H - \lambda (H^\dagger H)^2 \\
\mathcal{L}_{Yukawa} &= g^\ell_{i,j} \overline{\ell}_{i,R} H^\dagger \ell_{j,L} + g^U_{i,j} \overline{U}_{i,R} \tilde{H}^\dagger U_{j,L} + g^D_{i,j} \overline{D}_{i,R} H^\dagger D_{j,L} + h.c.
\end{aligned} \tag{1.1}$$

The gauge term describes the free fermion and boson fields, their interactions and the coupling with the Higgs field. $F^a_{\mu\nu}$ is the gauge -field strength tensor, defined as:

$$F^a_{\mu\nu} = D_\mu G^a_\nu - D_\nu G^a_\mu - c f_{acb} G^b_\mu G^c_\nu \tag{1.2}$$

where G^a_μ are the gauge vector fields, and f_{abc} are the structure constants of the group. D_μ is the covariant derivative:

$$D_\mu = \partial_\mu + ig_s\frac{\lambda^a}{2}G^a_\mu + ig\frac{\tau^a}{2}A^a_\mu + ig'Q_Y B_\mu \tag{1.3}$$

where λ^a are the generators of SU(3) (a = 1, 8, Gell-Mann matrices), τ^a are the generators of SU(2) (a = 1, 3, Pauli matrices), g_s, g, g' are the coupling of strong, weak and electromagnetic interactions. Q_Y is the weak hypercharge, defined similarly to the Gell-Mann-Nishijima formula:

$$Q_Y = 2(Q - T_3) \tag{1.4}$$

with Q the electric charge and T_3 the third component of weak isospin.

The Higgs term describes the Higgs potential with $\mu^2 > 0$. It has infinite degenerate minima corresponding to a non-zero vacuum expectation value equal to $\sqrt{\mu^2/2\lambda}$. This term introduces the spontaneous symmetry breaking that causes the mix between B^μ and $W^{0,\mu}$ into A$^\mu$ and Z^0, and the mass terms of the gauge bosons[10].

The Yukawa term connects the left-handed (weak isospin doublet) and right-handed component (weak isospin scalar) of the fermions through the Higgs doublet, giving them mass.

1.1.1 Muon decay

The Lagrangian that describes the dynamics of a muon is[11]:

$$\begin{aligned}\mathcal{L}_\mu = \; & e\bar{\mu}\gamma^\nu\mu A_\nu + \\ & -\tfrac{g}{\sqrt{2}}(\bar{\nu}_\mu\gamma^\nu\mu_L W^+_\nu + \bar{\mu}_L\gamma^\nu\nu_\mu W^-_\nu) + \\ & -\sqrt{g^2+g'^2}\Big(\bar{\mu}_L\gamma^\nu\Big(-\tfrac{1}{2} + sin^2\theta_W\Big)\mu_L + \bar{\mu}_R\gamma^\nu sin^2\theta_W\mu_R\Big)Z^0_\nu + \\ & -\tfrac{m_\mu}{\nu}\bar{\mu}\mu H\end{aligned} \tag{1.5}$$

From top to bottom, each line represents the: electromagnetic interaction, the charged current interaction, the neutral current interaction and the Yukawa interaction.
Fig. 1.2 shows the tree level Feynman diagram of the muon decay.

The muon decay time is:

$$\tau_\mu = 2.1969811(22)\mu s[12] \tag{1.6}$$

Tab. 1.1 shows the decay channels and the respective branching ratios.

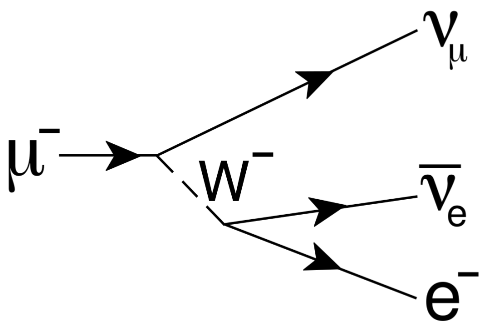

Figure 1.2: *Tree level diagram of muon decay process.*

Decay channel	Branching Ratio	CL
$\mu^- \to e^- \bar{\nu}_e \nu_\mu$	$\sim 100\%$	
$\mu^- \to e^- \bar{\nu}_e \nu_\mu \gamma$	(6.0±0.5) 10^{-8}(for E_γ >40 MeV)	
$\mu^- \to e^- \bar{\nu}_e \nu_\mu e^- e^+$	(3.4 ± 0.4) 10^{-5}	
$\mu^- \to e^- \nu_e \bar{\nu}_\mu$	$< 1.2\%$	90%
$\mu^+ \to e^+ \gamma$	$< 4.2\,10^{-13}$	90%
$\mu^- \to e^- e^+ e^-$	$< 1.0\,10^{-12}$	90%
$\mu^- \to e^- 2\gamma$	$< 7.2\,10^{-11}$	90%

Table 1.1: Muon decay channels and their branching ratios[12].

1.2 Charged Lepton Flavour Violation

1.2.1 Neutrino oscillations

Charged Lepton Flavour Violation is strictly forbidden in the SM with massless neutrinos. But a decay such as $\mu \to e\gamma$ could be possible through neutrino oscillations: Fig.1.3 shows one of the Feynman diagram contributing to the process.

The presence of massive neutrinos leads to the following expression of the branching ratio:

$$\mathcal{B}(\mu \to e\gamma) = \frac{3\alpha}{32\pi} \Big| \sum_{i,j=1,2,3} U^*_{\mu i} U_{ej} \frac{\Delta m^2_{ij}}{m^2_W} \Big|^2 \simeq 10^{-55} - 10^{-54} \tag{1.7}$$

where U_{ij} is the Pontecorvo-Maki-Nakagawa-Sakata (PMNS) matrix[13, 14] and Δm^2_{ij} is the difference between the squared masses of the i-th and j-th generation neutrinos.

The expected value for this process inside the extended SM with massive neutrinos framework is about forty orders of magnitude smaller than the sensitivity of present-day experiments[15].

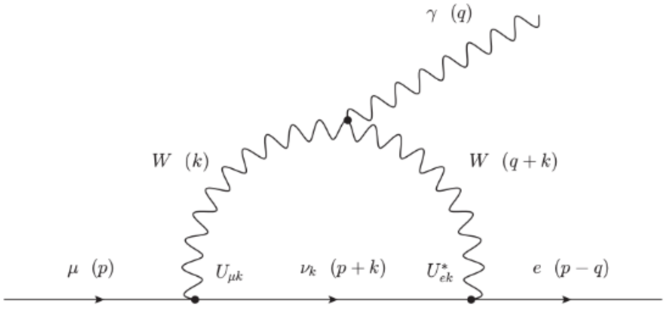

Figure 1.3: *Feynman diagram contributing to* $\mu \to e\gamma$ *process through neutrino oscillations.*

1.2.2 Beyond Standard Model Physics

Even if the SM is a successful theory in terms of description of particles interactions, it is commonly intended to be a low energy approximation of a more general theory capable of explaining some of the major issues of the theory and experimental hints of new physics [9]:

- naturalness and hierarchy problem: the Higgs mechanism gives an elegant solution to the problem of the gauge bosons masses, but it needs an "unnatural" fine tuning $\sim \mathcal{O}^{-34}$ of the Higgs mass, if considering a cutoff constant $\Lambda \sim M_{Planck}$;
- dark matter and dark energy: from cosmological measurements it is known that only the 5% of the universe is composed of ordinary matter, which is described by the SM. The 27 $\%$ is composed of Dark Matter and the remaining 68$\%$ is composed of Dark Energy, whose components and nature are unknown;
- matter-antimatter asymmetry: CP violation in weak interactions cannot explain the absence of anti-matter in the observable universe;
- origin of neutrino masses.

A candidate that could fix the naturalness problem and provide a Dark Matter candidate is supersymmetry (SUSY), which introduces a new gauge symmetry in which all the elementary particles have their own supersymmetric partners: the theory predicts the existence of a SUSY bosonic particle for each SM fermionic particle and a SUSY fermionic partner for each SM bosonic particle.

In the frame of Great Unification Theories (GUT), the coupling of the SM interactions unify in a unique coupling constant, corresponding to a unique gauge group containing the SM group. Possible candidates for the GUT group could be SU(5) or SO(10).

SUSY and SUSY GUT theories predict CLFV: they become possible because, even if at Planck, or GUT, scale the slepton (leptons SUSY-partners) mass matrix is diagonal in the flavour space, radiative correction may introduce non-null off-diagonal elements at the electroweak scale depending on the SUSY-partners mass scale.

Fig. 1.4 shows an the predicted $\mathcal{B}(\mu \to e\gamma)$ as a function of the right-handed slepton mass for different values of $tan\beta$ and the gaugino mass M_2[11].

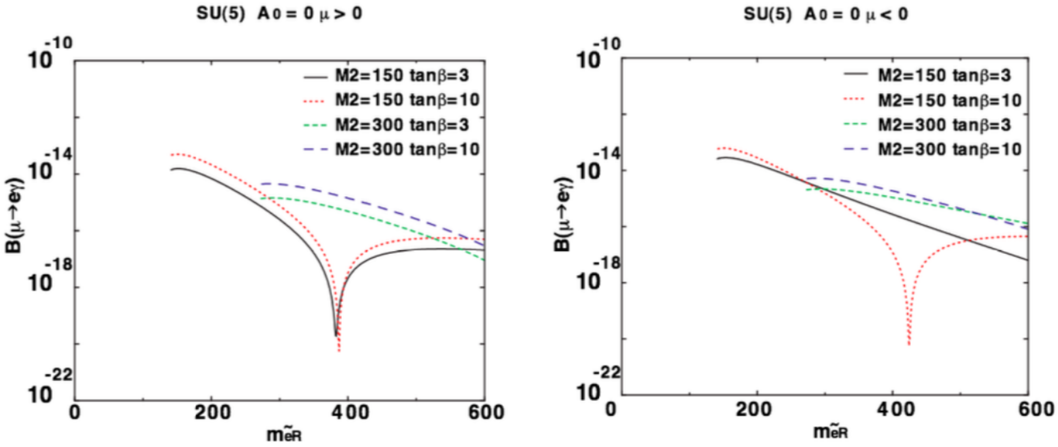

Figure 1.4: *Predicted ratios for the* $\mu^+ \to e^+\gamma$ *decay in the SU(5) SUSY GUT theory evaluated by Kuno and Okada in [11]. The branching ratios are evaluated as a function of the right-handed slepton mass at different* $tan\beta$ *and gaugino mass* M_2 *values.*

1.3 Process fenomenology

The search for the $\mu \to e^+\gamma$ decay is an important instrument in order to provide a clear experimental evidence of new physics and to identify the scale of physics beyond SM if discovered: as briefly exposed above, to make the decay possible, it is necessary to introduce new particles and interactions in the model, and the value of the branching ratio depends on the scale of new physics, making it possible to test scales up to 10^3 TeV with a sensitivity of 10^{-14} on this process.

But the signature of this process, and the backgrounds themselves, does not depend on the model: it is a two-body decay where a positron and a photon are produced back to back (the μ^+ is at rest), with energy equal to half of the muon mass ($m_\mu/2 =$52.8 MeV).

In order to distinguish the signal process from the background, it is necessary to measure the photon energy E_γ, the positron momentum p_{e^+}, their relative angle $\Theta_{e^+\gamma}$ and timing $t_{e^+\gamma}$ with the highest precisions. So, the number of expected signals for a given ratio $\mathcal{B}$ depends on the stopping muon rate R_{μ^+}, the measurement time T, the solid angle Ω subtended by the photon and positron detectors, the efficiencies of these detectors (ϵ_γ, ϵ_{e^+}) and the efficiency of the selection criteria ϵ_s:

$$N_{sig} = R_{\mu^+} \times T \times \Omega \times \mathcal{B} \times \epsilon_\gamma \times \epsilon_{e^+} \times \epsilon_s \tag{1.8}$$

The background can be distinguished in physical, due to the Radiative Muon Decay (RMD) $\mu \rightarrow e^+\nu_e\bar{\nu}_\mu\gamma$, and accidental, due to the coincidence between a Michel decay and a high energy photon coming from RMD, annihilation in-flight (AIF) or bremsstrahlung from Michel positrons. In the next paragraph the main characteristics of the backgrounds will be discussed.

1.3.1 Physical background

The background caused by the RMD process is due to events with high energy photons and low energy neutrinos, where the positron and the photon are emitted back to back. As already stated, the RMD branching ratios for $E_\gamma >$ 40 MeV is (6.0 ± 0.5) 10^{-8}, which is not negligible with respect to the expected branching ratios of the signal process.

Fig. 1.5 shows the RMD differential branching ratio as a function of the photon energy and branching ratios in terms of energy resolution as calculated in [11]. The variables used are defined as follows:

$$x = \frac{2E_{e^+}}{m_\mu}, \quad y = \frac{2E_\gamma}{m_\mu}, \quad z = \pi - \Theta_{e^+\gamma}. \tag{1.9}$$

with E_{e^+} is the energy of the emitted positron. The branching ratios are evaluated with respect to the FWHM of x and y, δx and δy, imposing that the resolution on z satisfies $\delta z <$

$2\sqrt{\delta x \delta y}$.

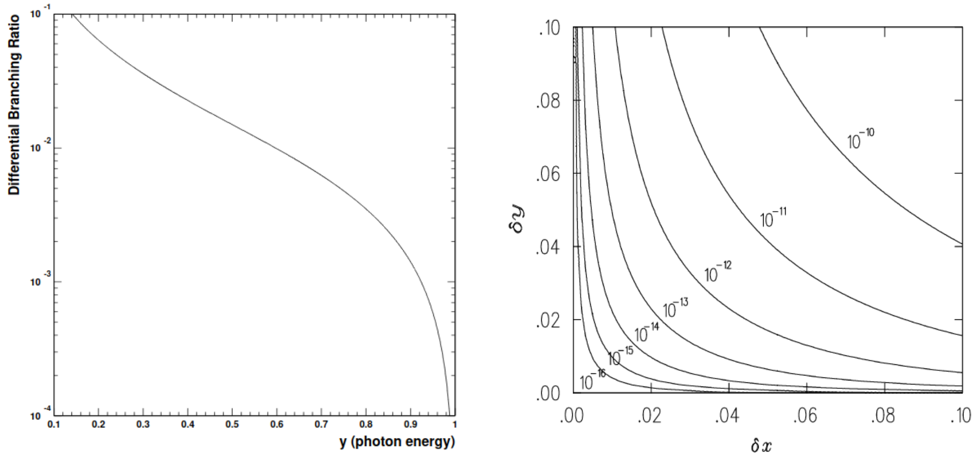

(a) Normalized energy spectrum for an RMD photon

(b) Expected RMD branching ratio as a function of δx and δy. $\delta z < 2\sqrt{\delta x \delta y}$

Figure 1.5: *RMD branching ratio dependence as evaluated in [11].*

The contribution in MEGII is expected to be smaller than 10^{-14}.

1.3.2 Accidental background

The major contribution to the background is composed of accidental background. The number of accidental events depends on the resolutions and on the stopping rate as follows:

$$N_{acc} \propto R_{\mu^+}^2 \times \Delta E_\gamma^2 \times \Delta p_{e^+} \times \Delta\Theta_{e^+\gamma}^2 \times \Delta t_{e^+\gamma} \times T \tag{1.10}$$

where Δ indicates the resolution on the measured quantity. As it can be seen, the dependence on the stopping rate is quadratic, while the physic background is linear in the stopping rate. During the MEG physics run, the beam rate could not be used at its maximum intensity because of the high accidental background that would have been produced and because the drift chambers could not have sustained such a high stopping rate. An important consequence of the MEGII sensitivity goal and upgrade is that the beam intensity will be maintained at a value higher by a factor two, from 3 10^7 to 7 10 ^{7} μ/s, with respect to the MEG configuration[5]. This needs an improvement of the general performances of the apparatus, upgrading the MEG detectors or even substituting them.

1.4 Experimental apparatus

The MEG apparatus was installed in the ΠE5 beam line at Paul Scherrer Institut (PSI), in Switzerland, and the data-taking has been completed in 2013. In the last years many upgrades where performed in order to increase the sensitivity reached by MEG collaboration by an order of magnitude. An important ingredient is the muon beam intensity, which will be higher during the data-taking than in MEG: the PSI accelerator complex and the details about the ΠE5 beam line will be discussed in the next chapter.
All the MEG detectors underwent upgrades, and in the following paragraphs the major changes and the expected resolutions will be exposed.

Fig. 1.6 shows the MEGII apparatus.

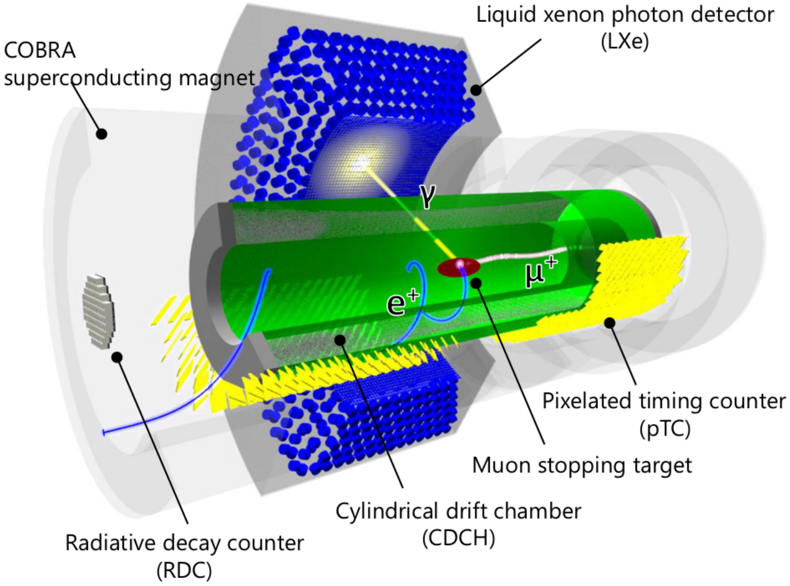

Figure 1.6: *3D schematic view of MEGII signal event.*

The apparatus consists of: a Liquid Xenon calorimeter(LXe), to measure the energy, the direction and the time of flight of the photon; a positron spectrometer composed of a Cylindrical Drift CHamber (CDCH) and a superconducting solenoid named COBRA (COnstant Bending RAdius) to track the positron and measure its momentum; a pixelated Timing Counter (pTC), to both measure the positron time of flight and improve the track reconstruction performed by the spectrometer. Another important detector is the Radiative Decay Counter (RDC), which was not present in MEG and that will be used to identify the low-energy positrons from RMD with high energy photons, to reduce the accidental background.

1.4.1 The target

In order to make easier the measurement and the reconstruction of the events, the muons are stopped in a thin target.
The upgraded target is a 140 μm thick polyethylene disc tilted by 15 deg w.r.t. the beam direction. The old MEG target was tilted by a higher angle, 22 deg, and was thicker, a 205 μm polyethylene-polyester film: this changes will reduce positron multiple scattering and the amount of AIF and bremsstrahlung photons inside the acceptance of the apparatus.

1.4.2 The Liquid Xenon calorimeter

The LXe calorimeter has been upgraded to improve the resolution and fix some of the major issues of the old version[5, 16]. It is a 900 ℓ C-shaped tank 38.5 cm deep, corresponding to ~ 14 radiation lengths (X_0 = 2.7 cm), in order to completely contain the showers originating from the photon passage through Liquid Xenon.
The scintillation process is possible thanks to the recombination and formation of the excited Xe_2^*, which is followed by ionisation. This dimer does not exist at ground state, letting the calorimeter be transparent to the scintillation light.

The light is collected by 4092 Multi-Pixel Photon Counters (MPPC, see Fig. 1.7) on the inner face and 668 2-inch PMTs on the other sides. In the previous version of the detector, the inner face was covered of the same PMTs on the other sides, and this caused one of the major issues of the calorimeter: due to the lack of coverage and to the higher photon density and the disuniformity on the inner face, there was a non-negligible difference in the resolutions between energy measurements on gammas interacting directly in front of a PMT or in the dead space among PMTs. Each MPPC consists of four 6×6 mm^2 sensors connected in series to reduce the effective capacitance of the total element and increase the timing accuracy.

Fig. 1.8 shows a view of the old and new versions of the calorimeter. Fig. 1.9 and 1.10 show the difference in resolution between the old and new version of the LXe calorimeter in terms of position reconstruction and energy resolution at different interaction depths.

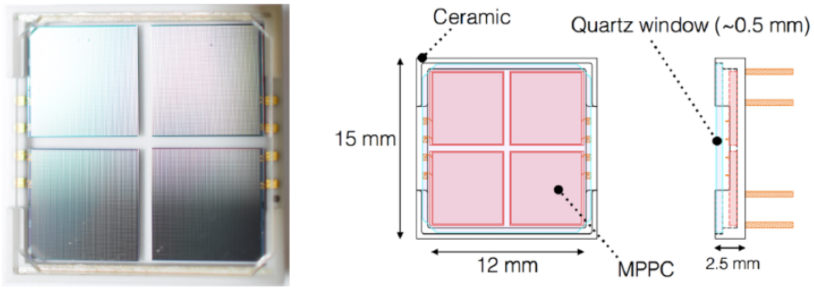

Figure 1.7: *Custom MPPCs used in the MEGII LXe calorimeter. On the left the picture of a MPPC. On the right the schematic view of a MPPC.*

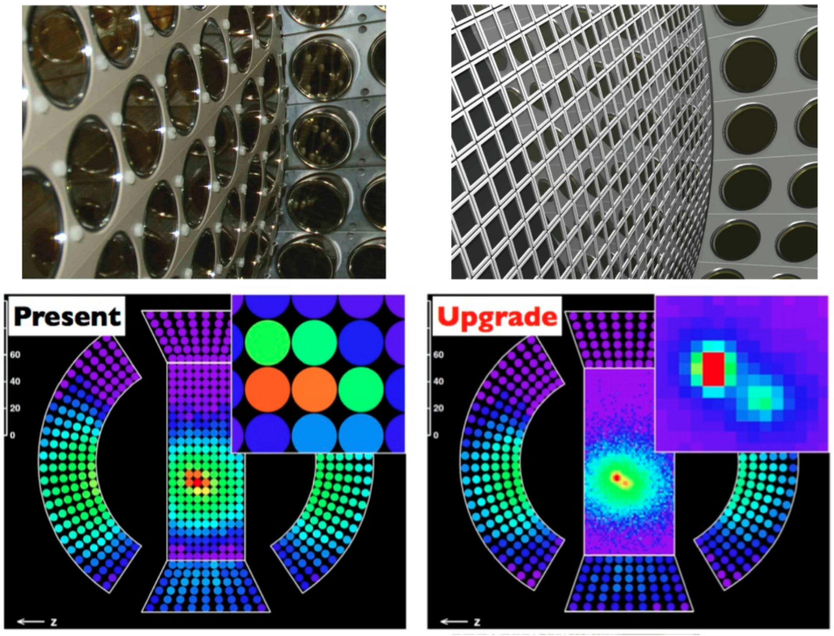

Figure 1.8: *In the top panels the inner face view of the old (left) and new (right) version of the calorimeter. In the bottom panels an example of scintillation light collection as detected by the old (left) or new (right) version of the calorimeter.*

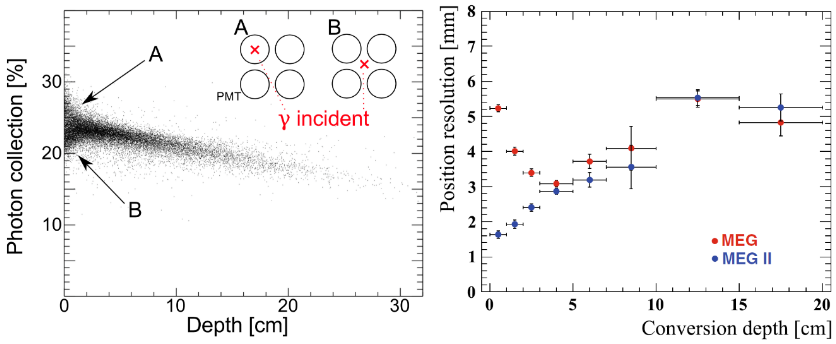

Figure 1.9: *On the left the photon collection efficiency as a function of the γ first conversion depth. On the right the position resolution for the MEG and MEGII versions of the LXe calorimeter as a function of the first conversion depth.*

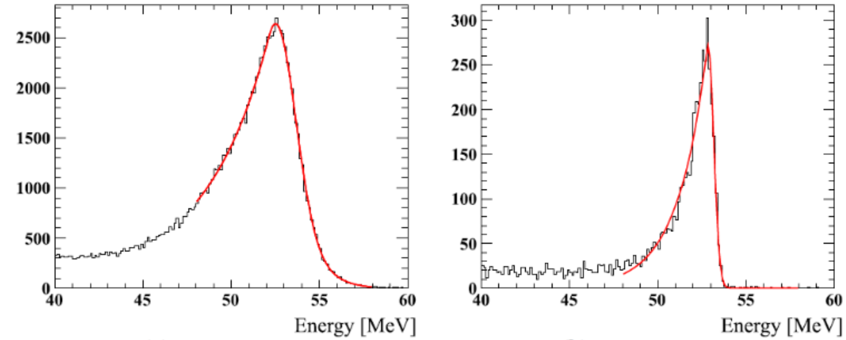

(a) MEG ($w < 2$ cm) **(b)** MEG II ($w < 2$ cm)

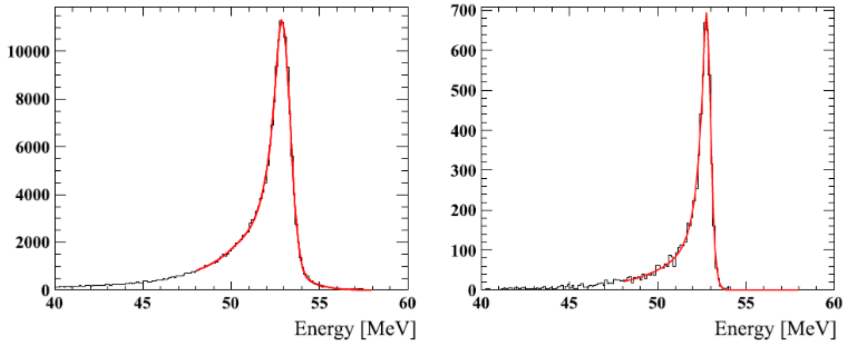

Figure 1.10: *LXe energy response for a signal γ. In the left panels the MEG response, while In the right panels the MEGII response. In the top panels the response in shallow γ conversion (depth $<$ 2 cm), while in the bottom panels the response in deep γ conversion (depth $>$ 2 cm).*

1.4.3 The Cylindrical Drift Chamber

MEGII uses a cylindrical shaped single volume drift chamber that will substitute the old drift chamber[5, 17]. The wires are positioned, in a stereo configuration for longitudinal hit localization, inside a volume filled with a 90/10 $\%$ He-Isobutane gas mixture. The total radiation length is 1.5 10^{-3} X_0, allowing for a single hit resolution below 120 μm, a momentum resolution of 130 KeV/c and angular resolutions $\simeq$ 5.5 mrad in the azimuthal angle and $\simeq$ 4 mrad in the polar angle.

The solenoidal magnetic field produced by the COBRA superconducting magnet, varies from 1.27 T at the center to 0.49 T at either ends. The gradient is designed to guarantee a bending radius of positrons weakly depending on the polar angle. It is also designed to remove quickly spiralling positrons sweeping them outside the spectrometer to reduce the track density inside the tracking volume.

1.4.4 The Pixelated Timing Counter

The new pixelated Timing Counter[18] consists of 512 elements composed of a plastic scintillating tile ($100{\times}40 \times 5\text{mm}^3$ or $100{\times}50 \times 5\text{mm}^3$ sized, depending on the longitudinal position in the pTC) coupled with multiple SiPMs. Each tile has a time resolution of $\sim$ 75 ps, but the actual resolution depends on the number of tiles hit by the positron after is passage. The resolution improves with a factor $1/\sqrt{N_{hit}}$, where the number of hit N_{hit} is estimated, and also experimentally confirmed, to be $\sim$ 9. Fig. 1.11 shows a single tile and the complete detector.

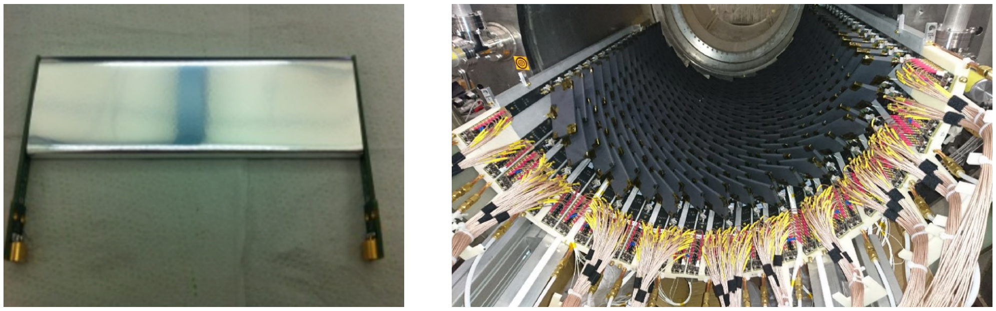

(a) Single pTC tile

(b) Downstream side of pTC inside COBRA

Figure 1.11: *pTC view.*

1.4.5 The Radiative Decay Counter

The Radiative Decay Counter is a new detector devoted to the revelation of low energy RMD positrons in order to tag high energy gammas in the LXe as potential accidental background events. This is possible thanks to the COBRA magnet field, that swipes away from the tracking area the low energy positrons, that are confined at smaller radius and that can be then revealed at the downstream end of the apparatus. Fig. 1.12 shows the detection of an RMD event with the RDC.

It is expected to detect $\simeq 42\%$ of the RMD γ background and to improve the sensitivity on the $\mu^+ \to e^+\gamma$ search of a 15 $\%$ factor.

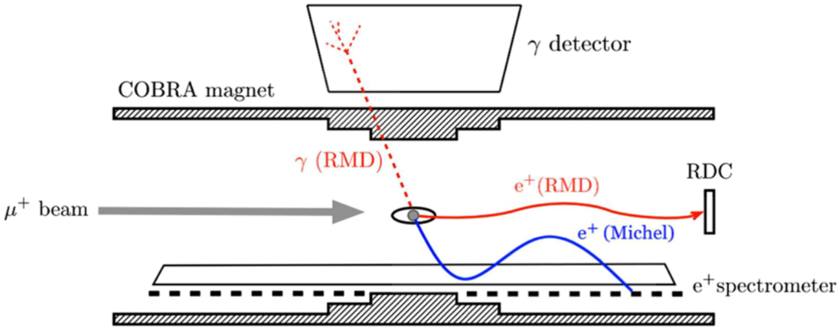

Figure 1.12: *Schematic view of the detection of RMD with the RDC.*

It consists of 12 plastic scintillators coupled to MPPCs, devoted to timing measurements, and 76 LYSO crystals[19] coupled to one MPPC, used for calorimetry measurements. Fig. 1.13 shows a schematic view of the elements.

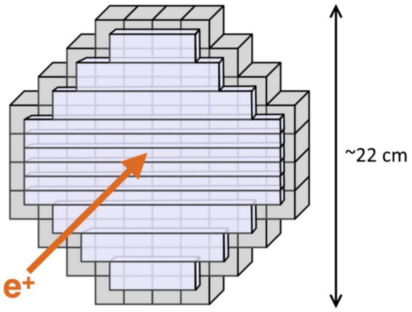

Figure 1.13: *Schematic view of the RDC. The horizontal long plates in front are the plastic scintillator bars, and the cubes behind are the LYSO crystals.*

1.4.6 The Trigger and DAQ systems

The MEGII upgrade leads to an increase in the total read out channel of a factor 3 and a muon stopping rate increase of a factor 2. The requirement for an efficient offline pile-up reconstruction and rejection is the availability of full waveform information. The DAQ system has to provide state-of-the-art time and charge resolution and a sampling speed in the GSPS range[5]. In the following paragraphs TDAQ system of the MEGII experiment will be introduced.

DAQ

The new system integrates the basic trigger and DAQ (TDAQ) functionalities onto the same electronics board, the WaveDREAM Board (WDB). Fig. 1.14 shows a schematics and a picture of the WDB.

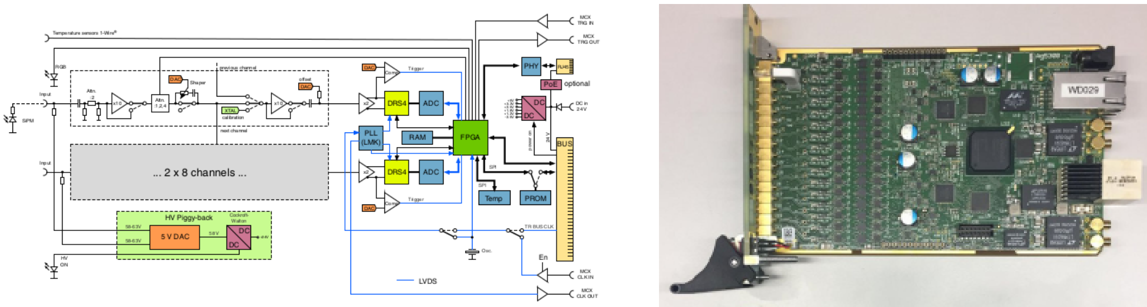

(a) WDB simplified schematics

(b) WDB picture

Figure 1.14: *WDB view.*

It contains 16 channels with variable gain amplification (0.5 to 100) and flexible shaping through a programmable pole-zero cancellation: pole-zero values go from 0 (off) to 7 (maximum) a.u.. Two DRS4 chips[20] are connected to two 8-channel ADCs, which are read out by a Field-Programmable Gate Array (FPGA) that performs complex trigger algorithm (sum of the input channels, threshold cuts, etc.). When a trigger occurs, the DRS4 chip is stopped and the internal analogue memory is digitized through the same ADCs previously used for the trigger.

The WDBs can supply up to 240 V per channel through the signal cables. This is possible through an ultra-low noise bias voltage generator based on a Greinacher multiplier.

Trigger

The trigger is based on a real time reconstruction algorithm that rely on the fast response detectors: LXe for γ observables and pTC for e^+ observables. The FPGA in the WDB performs the reconstruction of decay products observables, such as momenta, relative timing and direction, through logic equations.

1.4.7 Expected sensitivity

Tab. 1.2 collects the resolutions and efficiencies foreseen for MEGII compared to the MEG performances.

	MEG	MEGII
Resolutions		
δE_{e^+} [keV]	380	130
$\delta\theta_{e^+}$ [mrad]	9.4	5.3
$\delta\phi_{e^+}$ [mrad]	8.7	3.7
$\delta z_{e^+}/\delta y_{e^+}$ [mm]	2.4/1.2	1.6/0.7
δE_γ ($w > 2$ cm/$w < 2$ cm) [%]	2.4/1.7	1.1/1.0
$\delta u_\gamma/\delta v_\gamma/\delta w_\gamma$ [mm]	5/5/6	2.6/2.2/5
$\delta t_{e^+\gamma}$ [ps]	122	84
Efficiencies [%]		
Trigger	$\simeq 99$	$\simeq 99$
Photon	63	69
e^+ (tracking × matching)	30	70

Table 1.2: Comparison between MEGII and MEG performances.

In order to estimate the sensitivity a detailed MC simulation of the beam and detectors based on Geant4[21, 22, 23] was implemented. The output of the MC events are converted into simulated electronic signals, based on data collected with prototypes or final detectors. Pile-up is included. The expected sensitivity is shown in Fig. 1.15.

Assuming 20 weeks of DAQ time per year, it is possible to achieve a 6 10^{-14} sensitivity in 3 years.

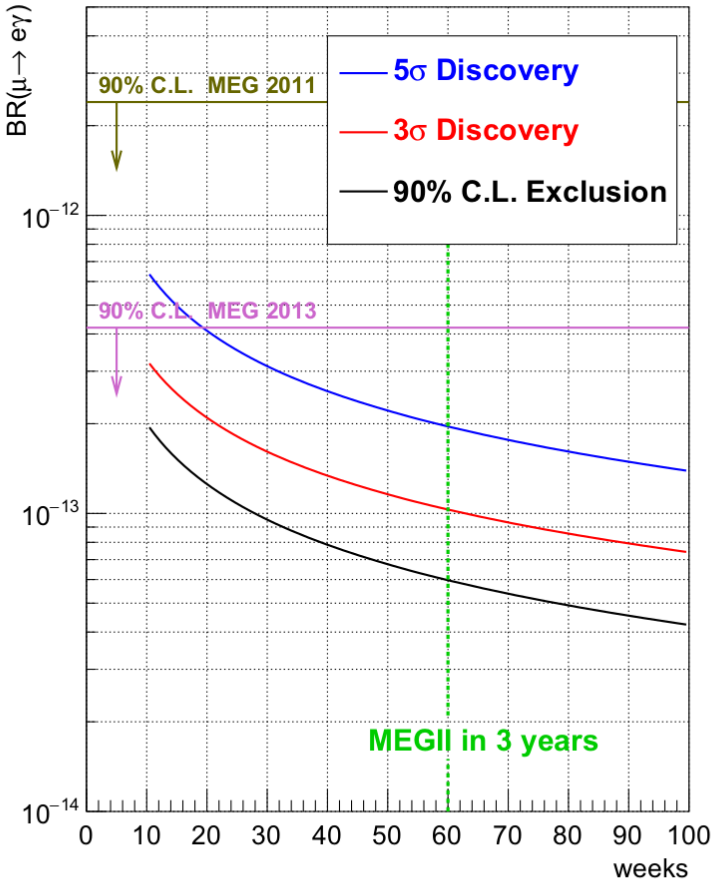

Figure 1.15: *Expected sensitivity and discovery potential of MEGII as a function of the DAQ time compared with the bounds set by MEG[4].*

Chapter 2

The ΠE5 beam line

The MEGII experiment was conceived in order to measure the rare decay mode $\mu^+ \to e^+\gamma$. It is trivial to say that in order to do so a high intensity muon beam is needed.

In the next chapter I will describe the Proton Accelerator Complex at PSI (see Fig. 2.1), the muon production mechanism and the characteristics of the beams delivered in the ΠE5 experimental area.

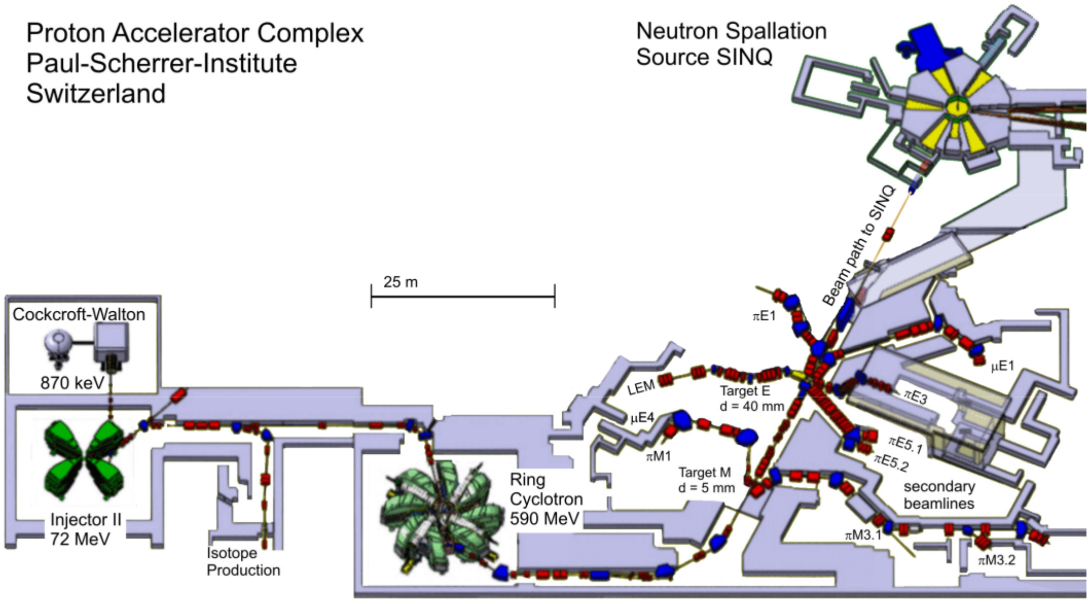

Figure 2.1: *Overview of the PSI high intensity accelerator complex.*

2.1 Proton beam at PSI

The PSI high intensity proton accelerator delivers a beam with 590 MeV kinetic energy and presently 1.4 MW average beam power[24]. The acceleration chain is performed starting from an Electron Cyclotron Resonance ion source (ECR), where Hydrogen is ionized. The so-obtained protons are firstly accelerated by a Cockcroft-Walton pre-accelerator and transported to a first isochronous cyclotron: the Injector II. The last step of the acceleration is performed at the principal machine: the RING cyclotron (see Fig. 2.1). The beam is produced in continuous wave (CW) mode at a frequency of 50.6 MHz.

The high intensity proton beam is used to produce pion and muon beam by interaction with two graphite targets that are realized as rotating wheels. Muons are produced through pion decay: the production mechanism will be described in details in the following paragraphs.

Only a fraction of the proton beam is used for muon and pion production, the remaining beam, roughly 1 MW, is then used to produce neutrons in a spallation target in the Swiss Spallation Neutron Source (SINQ) facility.

2.1.1 The Sector Cyclotron

A cyclotron is a machine that accelerates particles, confined in its volume through a magnetic field, with alternate electric fields. The electric field must be in phase with the rotation period of the beam. The period is defined by the inverse of the cyclotron resonance frequency:

$$f_{cyc} = \frac{\omega}{2\pi} = \frac{qB}{2\pi\gamma m} \tag{2.1}$$

where B is the magnetic field and q, m and γ are the charge, the mass and the Lorentz factor of the particle.

In case of relativistic particles, the frequency of the electric field must vary with the cyclotron frequency. Anyway, it is possible to maintain fixed the rotation period by introducing a gradient in the magnetic field, so that when the particle gains energy and the radius of its trajectory increases, the ratio of the magnetic field and the particle Lorentz factor, locally, has to remain constant: B must be proportional to γ.

The use of a single magnet limits the energies that can be reached, because higher energies means higher radius or fields, hitting a feasibility limit in terms of technology and cost. A sector cyclotron is realized modularly, involving the combination of sector shaped magnets and RF resonators forming a ring: this characteristic allows to reach energies up to 1 GeV. The radius increment per turn is:

$$\frac{dR}{dn_t} = \frac{R}{\gamma(\gamma^2 - 1)} \frac{U_t}{mc^2} \tag{2.2}$$

where U_t/mc^2 is the energy gain per turn over the rest energy and R is the orbit radius. Thus obtaining a large turn separation is increasingly difficult with higher beam energy, while a large extraction radius is desirable. It is important to achieve the highest possible energy gain per turn, to limit the number of turns before extraction: in practice the performance of high intensity cyclotrons is limited by extraction losses. At the extraction of RING the loss is kept at a 10^{-4} level. Fig. 2.2 shows a schematic view of the PSI RING and the radial beam profile as obtained through calculations (OPAL) and measurements.

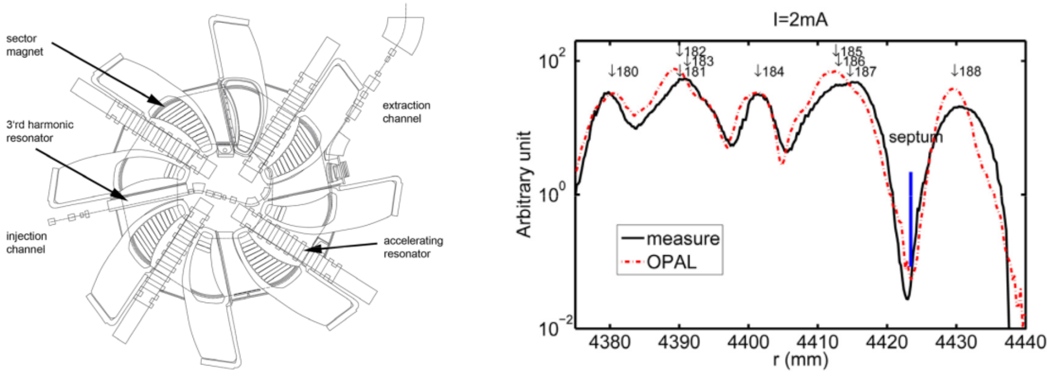

(a) Schematic top view of the PSI RING cyclotron

(b) Radial extraction profile with indicated numbers at extraction. The density is minimized at the location of the extraction electrode. The red dotted line is obtained with the tracking code OPAL.

Figure 2.2: *The PSI RING view.*

2.1.2 Beam parameters

In its complex, the proton acceleration facility consists of three acceleration stages. After the passage through the second target (E), which is 40 mm thick, there is a significant increase in emittance which results in an unavoidable loss at collimators after the target. Tab. 2.1 collects the selected beam parameters along the accelerator chain, while Fig. 2.3 shows the optics of the transfer line containing the targets[24].

	I_{beam} [mA]	E_k [MeV]	$\beta\gamma\epsilon_x$ [μm rad]	rel. loss
at p-source	25	0.06	0.13	
transfer to Inj II	10	0.87	1.3	
extraction to Inj II	2.2	72	2.5	$< 10^{-4}$
transfer to RING	2.2	72	2.5	$\simeq 2\ 10^{-3}$
extraction RING	2.2	590	7.5	$\simeq 2\ 10^{-4}$
transfer to SINQ	1.5	572	42	0.3

Table 2.1: Proton beam parameters at PSI along the acceleration chain.

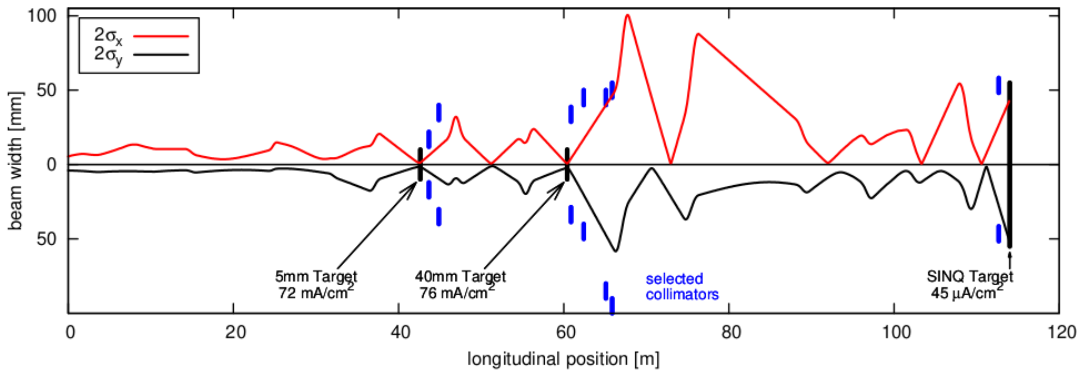

Figure 2.3: *Horizontal and vertical beam envelopes in the transfer line from RING cyclotron to SINQ. The two meson production targets and the SINQ spallation target are indicated with current densities. Selected collimators are shown.*

2.2 Target E

As already mentioned, along the transport line between RING and SINQ, there are two meson production targets: the target M and the target E. Target M feeds two lower intensity meson beam lines: a high resolution pion beam (ΠM1) and a beam dedicated to muon spin-resonance measurements (ΠM3). Target E provides five high intensity meson beam-lines: ΠE1 to ΠE5. The MEGII experiment is positioned inside the ΠE5 area.

Both target M and E are rotating wheels of polycrystalline graphite cooled by thermal radiation. Tab. 2.2 collects some parameters for the two targets. Fig. 2.4 shows the two targets.

Meson Production Target	M	E
Mean Diameter [mm]	320	450
Target Length [mm]	5.2	40
Target Width [mm]	20	6
Graphite Densty [g/cm^3]	1.8	1.8
Proton Beam Losses [%]	1.6	18
Power Deposition [kW/mA]	2.4	30
Irradiation Damage Rate [dpa/Ah]	0.11	0.1
Operating Temperature [K]	1100	1700
Rotational Speed [Turns/s]	1	1

Table 2.2: Some parameters for the meson production targets.

The rotation is crucial in the case of target E, because of the high energy deposit: each proton releases $\simeq$ 15 MeV of energy inside target E, leading to a power deposition $\simeq$ 66 kW when the proton current is at its maximum level (2.2 mA). The rotational motion allows to distribute the power over the whole target.
The proton beam impinges on the target E with parameters[25]:

- σ_x = 0.75 mm
- σ_y = 1.25 mm

- I_p = 2.2 mA

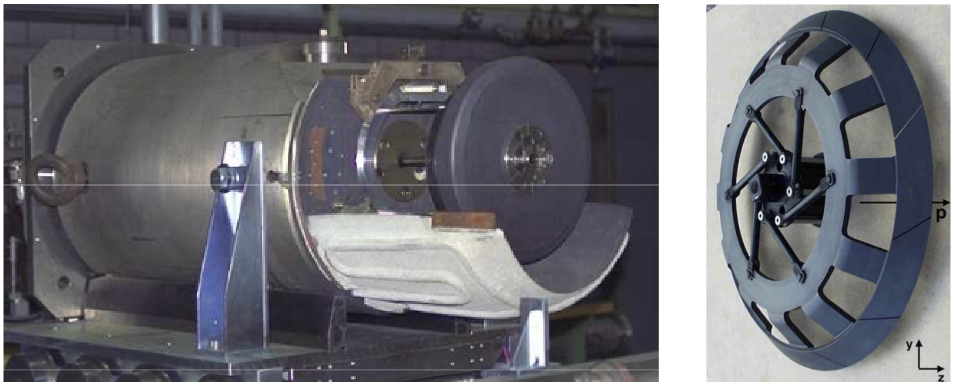

(a) Picture of the target M.

(b) Picture of the target E. The arrow indicates the direction of the proton beam.

Figure 2.4: *Meson production targets.*

The interaction between the protons and the nuclei in the target produces a huge amount of charged pions: a fraction of these pions are delivered along beam lines in the experimental areas; another part of these pions decays in muons. Depending on the initial energy and production vertex, the pions can decay outside the target or inside the target.

The pions that decay outside the target are both positively and negatively charged and produce the so-called cloud muons. The pions that decay inside the target are mostly positive, because of the high negative pion capture cross-section. When a pion decays inside the target, only muons produced near the surfaces can escape, because of their low initial energies (4 MeV): the so-called surface muons. Fig. 2.5 shows the two possible muon production mechanisms.

As already mentioned above, the radio-frequency period (equal to the proton bunch spacing) is $\simeq$ 20 ns. The pion decay time at rest is $\simeq$ 26 ns. Thus the resulting muon beam is almost continuous. This feature is very important for the MEGII experiment: considering a pulsed beam with the same mean beam rate as of the ΠE5 line, the instantaneous rate would be higher, leading to a higher number of accidental background events for the same number of signal events.

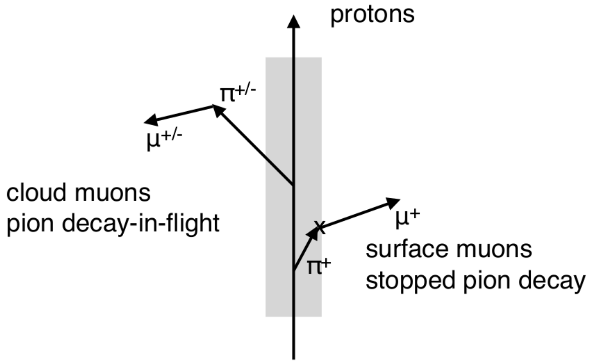

Figure 2.5: *Muon production at PSI.*

Tab. 2.3 collects the parameters for the backward and for the side faces of target E[25] for positive muons below the two-body decay momentum value (29.8 MeV). The coordinate system is the same as in Fig. 2.4. Parameters relative to the forward face are equal to the ones relative to the backward face with the exception of the muon flux, which is reduced to 1.2 10^{10} μ^+/s.

Backward face	Side faces
x_{rms} = 1.6 mm	z_{rms} = 10.9 mm
x'_{rms} = 668 mrad	z'_{rms} = 678 mrad
y_{rms} = 7.3 mm	y_{rms} = 7.9 mm
y'_{rms} = 677 mrad	y'_{rms} = 678 mrad
μ^+/p = 1.2 10^{-6}	μ^+/p = 8.3 10^{-6}
I_{μ^+} = 1.8 10^{10} μ^+/s	I_{μ^+} = 1.2 10^{11} μ^+/s

Table 2.3: Positive muons parameters depending on production surface with momentum below 29.8 MeV.

During fall 2019, an upgraded version target E was built and tested in order to increase the muon rate at production. Further details are discussed in the following paragraph.

2.2.1 Target E: upgrade

In order to increase the sensitivity on rare decay channels, it is mandatory to increase the intensity of particle beams. In the case of meson factories it can be done increasing the power of the primary beams or optimizing production targets and beam lines. The first possibility is not trivial to pursue when the primary beam powers are already in the MW-regime, as in the case of proton beam at PSI. For this reason a study on the optimization of the target E was performed, resulting in the production and test of a new target prototype in fall 2019[25]. The studies involved alternative materials performances and geometry optimization.

In terms of materials, it is important to study the pion yield and the relative muon yield. The relative muon yield scales as:

$$I_{\mu^+}^{rel} \propto n\sigma_{\pi^+}\left(\frac{dE}{dx}\right)_{\pi^+}\frac{1}{\left(\frac{dE}{dx}\right)_{\mu^+}}\frac{\rho_C(6/12)_C}{\rho_X(Z/A)_X} \propto \frac{1}{Z^{\frac{2}{3}}} \tag{2.3}$$

Fig. 2.6 shows the μ^+ and π^+ yield as a function of the target material Z.

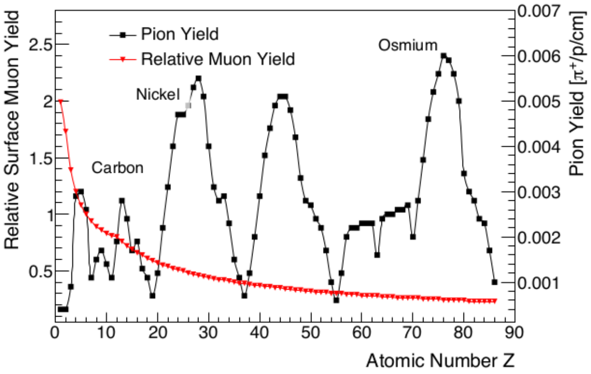

Figure 2.6: *The relative muon yield and absolute pion yield at a proton energy of 585 MeV as a function of atomic number Z. Liquid densities are assumed for elements that are gaseous at normal temperature and pressure.*

Due to the atomic number dependence of the relative muon yield, low Z materials are favoured. In terms of muon yield, Beryllium would be better than Carbon, but it is disfavoured in terms of safety reasons: due to high evaporation a Beryllium target would have to be bigger than a Carbon one in terms of radius, by a factor 10[26]. Carbon was chosen to build the new target.

In terms of geometry, different shapes were taken into account. Fig. 2.7 shows the different shapes considered and Tab. 2.4 collects the relative intensity with respect to the standard target E.

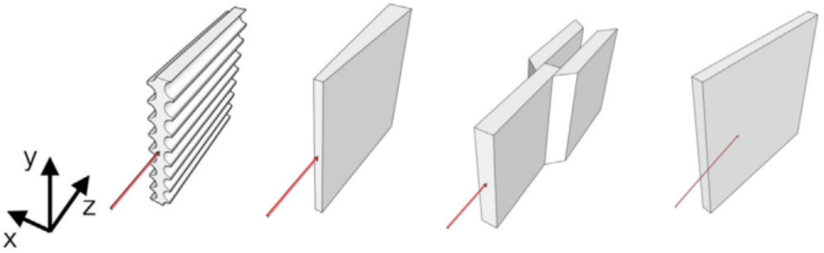

Figure 2.7: *Different geometries studied. From left to right: grooved, trapezoidal, fork and rotated slab targets. The red line marks the proton beam.*

Geometry	Sideways	Backwards	Forwards
Grooved	1.02	1.00	0.97
Trapezoid	1.15	0.98	0.79
Fork	1.45	1.14	0.79
Rotated slab	1.28	1.40	1.63

Table 2.4: Relative muon beam intensity with respect to the standard target E, for different target geometries (see Fig. 2.7).

The rotated slab target yield is the best overall enhancement and a mechanically simple solution. Fig. 2.8 shows the relative μ^+ rate of the rotated slab target at different rotation angles.

The tested configuration is shown in Fig. 2.9: the selected angle is 8 deg, with a relative rate enhancement roughly equal in all three directions. The measurements were performed using the vacuum prototype of the SciFi detector (see Ch. 3) confirming the expected performances.

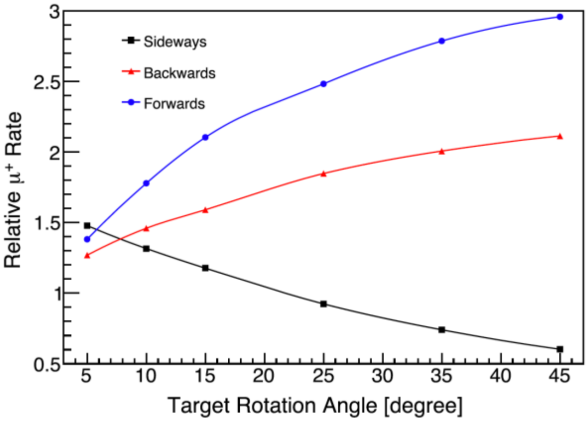

Figure 2.8: *Enhancement factors in the three directions studied as a function of the rotation angle of the slab target. The length of the slab is fixed at 150 mm.*

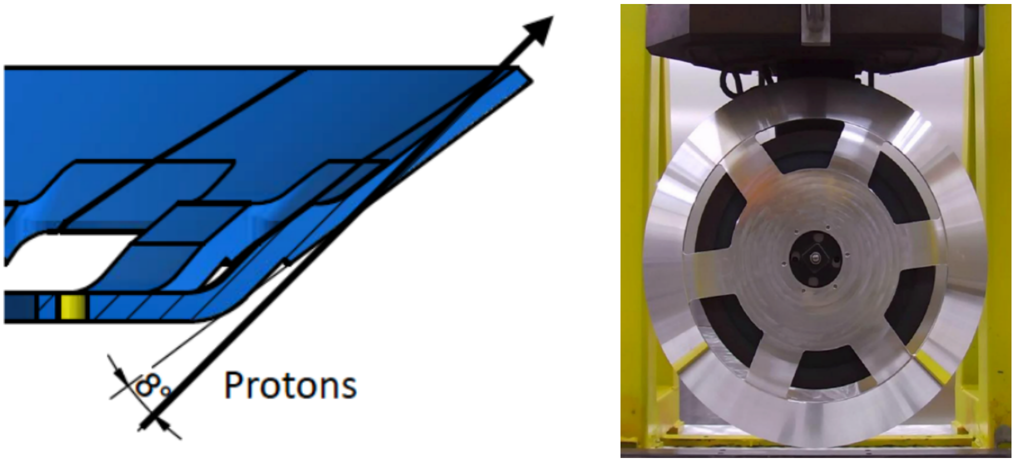

(a) Schematic of the slanted target.

(b) Picture of the target prototype.

Figure 2.9: *Slanted target prototype.*

2.3 ΠE5 beam line and MEG beam transport system

The ΠE5 beam line is a 165 deg backwards-oriented, windowless, high-acceptance (150 msr), low-momentum (< 120 MeV/c), dual-port π^-, μ^+ or e^+ channel. For the MEGII experiment the beam line is tuned at 28 MeV/c with a momentum bite of 5-7 $\%$ FWHM, depending on the opening of the momentum selecting slits placed in the front-part of the channel.

Fig. 2.10 shows a schematic of the ΠE5 beam line.

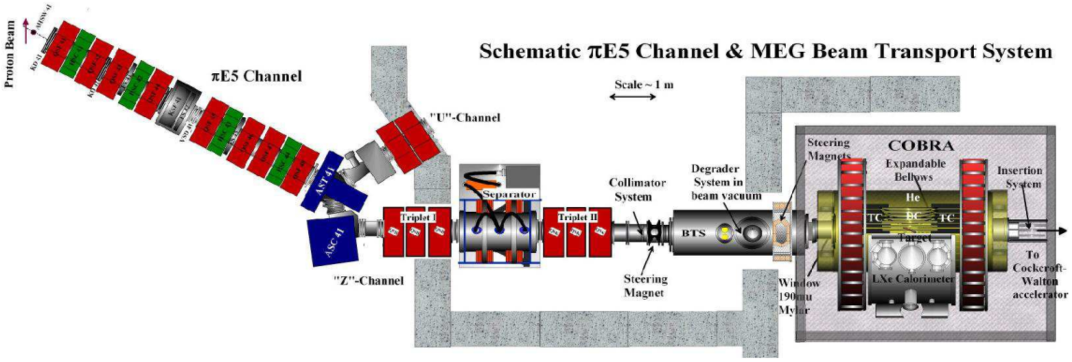

Figure 2.10: *Schematic of the* Π*E5 beam line and the MEG beam transport system.*

A low momentum muon beam is a suitable choice for MEGII, because of the strong dependence of the range straggling on the particle momentum[27]:

$$\Delta R = a\sqrt{(0.09)^2 + (3.5\Delta p_{\mu^+}/p_{\mu^+})^2} \times p_{\mu^+}^{3.5} \tag{2.4}$$

where ΔR is the range straggling, p_{μ^+} is the muon momentum and a is a constant depending on the stopping material.

In order to keep under control the range it is much more convenient to reduce the momentum rather than the momentum bite.

A quadrupole and sextupole channel connects the production target E to the ΠE5 area. The AST 41 dipole allows to deviate two experimental ports just by switching its polarity[28]: channel Z and channel U. The MEGII experiment is connected to port Z.

Quadrupole triplet-I provides an optimal high transmission through the Wien-filter, that produces a ±200 keV potential across the 19 cm gap of the electrodes. The mass separation is equivalent to an angular separation of +88 mrad between muons and positrons and of -

25 mrad between muons and pions. The combination of the Wien-filter with the quadrupole triplet II and a collimator system (11 X_0 of Pb equivalent) determines a separation quality between muons and positrons beams of 8.1 σ_μ, corresponding to a 12 cm physical separation at the collimator system[29]. Fig. 2.11 shows the separation quality measured during the 2015 Pre-Engineering Run.

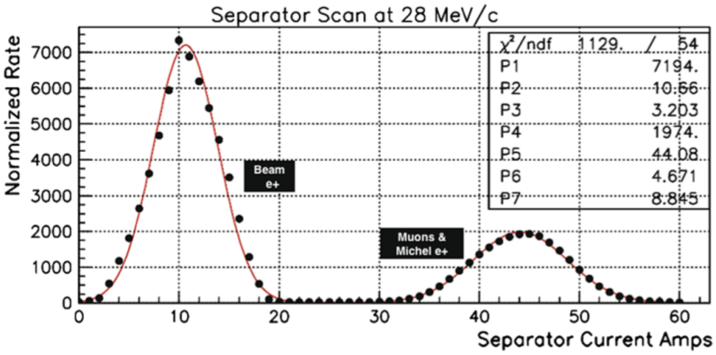

Figure 2.11: *Measurement of the separation quality with the Wien-filter during the 2015 Pre-Engineering Run.*

The beam is then delivered inside the superconducting COBRA magnet by the Beam Transport Solenoid (BTS).

Fig. 2.12 shows the measured muon spectrum at the collimator. Each point was obtained by optimising the whole beam line for the corresponding central momentum and measuring the full beam-spot intensity.

In the ΠE5 beam line the maximum muon beam rate is 1.5 10^8 μ^+/s.

2.3.1 The Beam Transport Solenoid

The BTS is a 2.8 m long iron-free superconducting solenoid, with a 38 cm warm-bore aperture, coupling directly to the beam line vacuum. Fig. 2.13 shows a picture of the BTS.

The maximum reachable magnetic field inside the BTS is 0.54 T at a current of 300 A. Three iron-free correction dipole magnets are used to compensate for a radial asymmetry in the fringe field caused by the interaction of the stray field from the large aperture, iron-free COBRA magnet with an iron component of the hall-floor foundations.

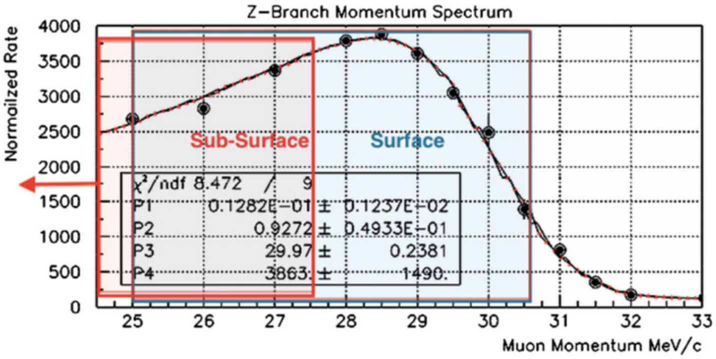

Figure 2.12: *ΠE5 muon spectrum at collimator. The fitting curve is a* $p^{3.5}$ *power function, folded with a gaussian momentum resolution corresponding to the momentum bite and a constant cloud muon contribution.*

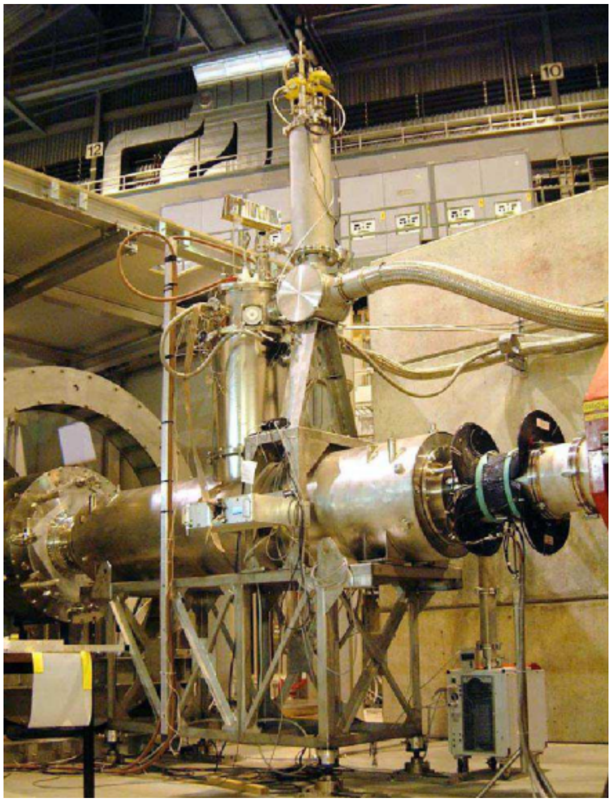

Figure 2.13: *A picture of the Beam Transport Solenoid (BTS) coupled to the beam line.*

A Mylar®degrader system is placed at the central focus of the BTS in order to minimise multiple Coulomb scattering.

2.3.2 Auxiliary particle beams

In order to measure the $\mu^+ \to e^+\gamma$ process branching ratio is very important to calibrate and monitor the apparatus status. In order to do so, two more particle beams are needed besides the muon beam: a quasi-monochromatic positron beam of 53 MeV/c ($\sigma^{beam}_{p_{e^+}} \sim 250$ keV/c, $I_{e^+} \sim 10^7$ e^+/s) to calibrate the spectrometer through Mott scattering[5] and a stopped negative pion beam of 70.5 MeV/c ($\sigma^{beam}_{p_{\pi^-}}/p_{\pi^-} \sim 3.5\%$, $I_{\pi^-} \sim 1.7\ 10^6$ π^-/s) for charge exchange $\pi^- p \to \pi^0 n$ (CEX) and radiative capture $\pi^- p \to \gamma n$ (RC) photons, used to calibrate the LXe calorimeter and check the full apparatus (see Ch. 5).

In the next paragraphs two new beam monitors will be introduced: a Scintillating Fiber grid (SciFi, see Ch. 3) and a matrix of scintillating elements (MatriX, see Ch. 4). These two detectors are designed to measure the beams between the BTS and COBRA (SciFi) and at COBRA center. Fig. 2.14 shows the positions of SciFi and MatriX along the ΠE5 beam line.

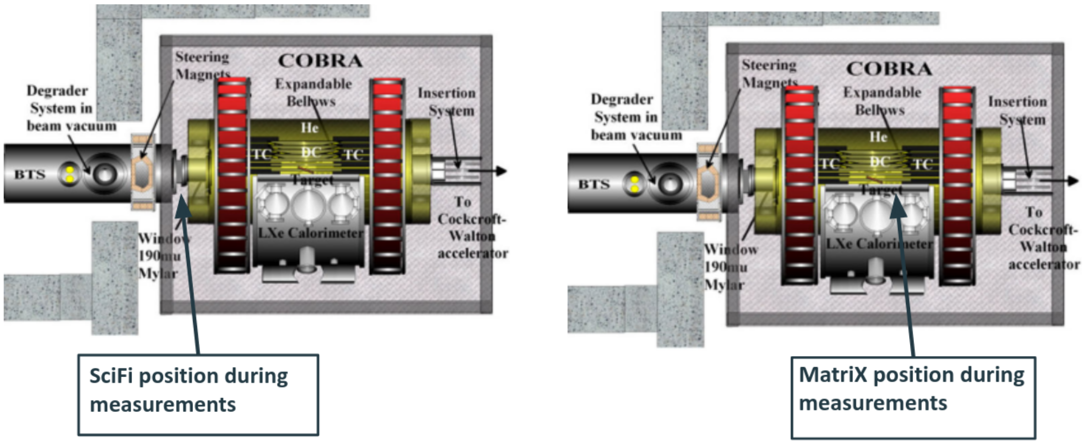

(a) SciFi position.

(b) MatriX position.

Figure 2.14: *Position along the ΠE5 beam line of the two new beam monitors.*

Chapter 3

Diagnostic tools: SciFi

As already mentioned in Ch. 1, it is important to measure the beam rate and the beam shape in the ΠE5 line with high precision and over the data taking period (Eq. 1.8, Eq. 1.10). Two online beam monitors are foreseen in the MEGII experiment: an ultra-thin CsI(Tl) luminophore foil beam monitor[5] and a quasi non-invasive, high rate beam monitoring tool based on scintillating fibers (SciFi[6]).

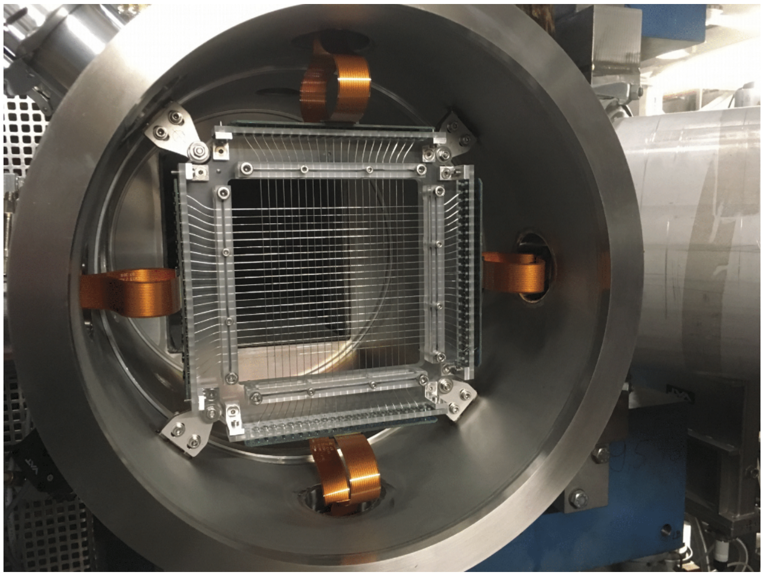

Figure 3.1: *SciFi (Scintillating Fibers) detector view.*

The SciFi detector is designed to measure the beam size between the BTS and COBRA (Fig. 3.2), where the beam is wider (μ^+ beam $\sigma_{x,y} \sim 20$ mm). In the following chapter I will be referring to SciFi measurements at collimator, because up to date the tests of the detector along the ΠE5 beam line were made majorly at collimator.

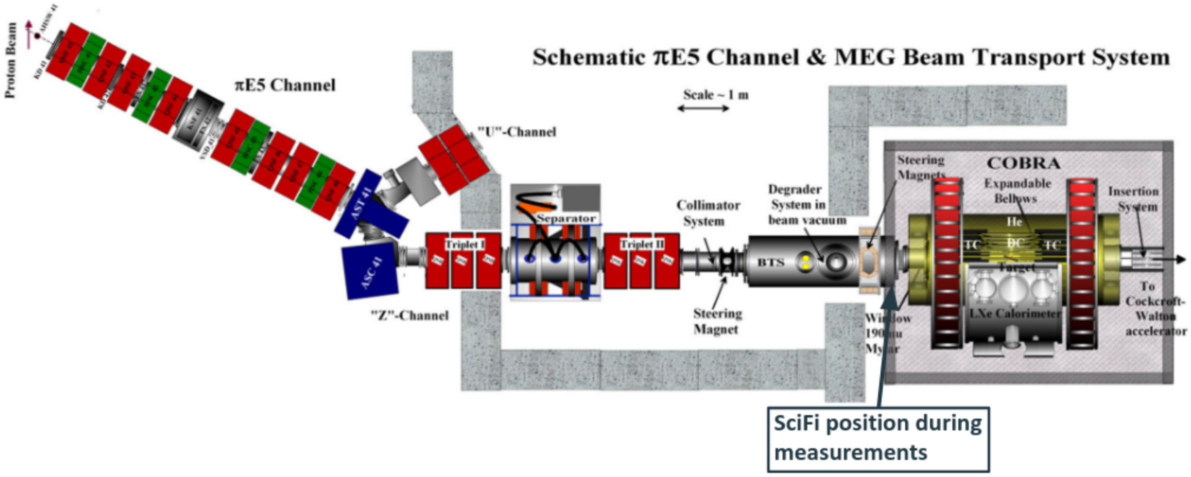

Figure 3.2: *SciFi position along the beam line.*

In the next chapter I will be introducing the SciFi detector (Fig. 3.1) and its Monte Carlo simulation implementation with the Geant4 toolkit[21, 22, 23].

3.1 Basic principle: brief introduction

SciFi is a beam monitor detector based on scintillating fibers coupled to silicon photomultipliers (SiPMs). When a charged particle passes through a scintillator it deposits energy due to ionization[30, 31] (Fig. 3.3). The energy gained by the electrons in the scintillator is then emitted as low energy photons (typically in the visible spectrum), distributed uniformly in solid angle[32].

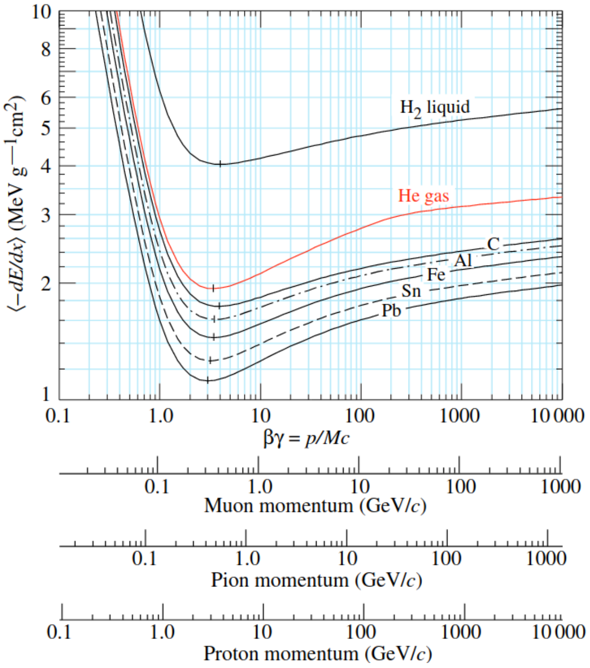

Figure 3.3: *Mean energy loss in liquid hydrogen, gaseous helium, carbon, aluminum, iron, tin and lead. Radiative effects are not included[12].*

Of course there wouldn't be any possibility to detect this light without shifting the energy levels of the scintillator's components: otherwise light would be reabsorbed by the atoms (or molecules) and energy would only be dissipated without any possibility of detection. Scintillators are classified according to the type of mechanism that let's the scintillator be transparent to scintillation light. The types of scintillator that will be considered are two:

- inorganic scintillators: the scintillator is doped with an element (activator) which aim is to introduce non homogeneities. The scintillator material is transparent to the light emitted by the activator[30, 31].

- organic scintillators: the scintillator is an organic molecule that, after electrons excitation, changes state with radiationless transitions and then emits light[30, 31].

The SciFi detector is composed of organic scintillator fibers (Saint-Gobain BCF-12[33]) with a square section. At each end of the fibers there is an S13360-1350CS Hamamatsu[34] SiPM coupled through optical grease (Saint Gobain BC-631[35]). In the next section, the details on the characteristics of the scintillating material and on the SiPM's working principle will be exposed.

Actually there are two SciFi prototypes: one with fibers 0.25 mm wide; one with fibers 0.5 mm wide. Assuming that the mean energy deposit in BCF-12 is almost the same as the one in Carbon, it is possible to estimate the number of photons at each end of the fibers, after the passage of the charged particle. The estimation is done considering minimum ionizing positrons, that are the particles with the lowest energy deposit among the particles considered in the simulation.

The number of scintillation photons produced is:

$$N_{ph} = \left\langle \frac{dE}{dx} \right\rangle \times \Delta x \times Y_{BCF-12} \simeq 2.2\,\text{MeV/cm} \times 0.25\,\text{mm} \times 8\,\text{Photons/KeV} \simeq 400 \tag{3.1}$$

Where $\left\langle \frac{dE}{dx} \right\rangle$ is the mean energy loss for minimum ionizing particles trough BCF-12, evaluated using carbon and hydrogen energy losses [36], and $\mathrm{Y}_{\mathrm{BCF-12}}$ is the scintillation yield of BCF-12[33].

The trapping efficiency of BCF-12 squared fibers is $\varepsilon_{\text{trap}}$ = 7.3 %[33].

The number of outgoing photons is therefore:

$$N_{ph,out} = \frac{N_{ph} \times \varepsilon_{trap}}{2} \simeq 15 \tag{3.2}$$

The value doubles if we consider 0.5 mm wide fibers.

Due to the small amount of photons arriving at the SiPM, the trigger is designed to accept only coincidence signals between SiPMs at the end of the same fiber. In the next sections of this chapter the performances of the current setup of SciFi and the information that can be obtained by coincidence between fibers will be discussed.

3.2 Single element: crystal fiber simulation

3.2.1 Single Element description

SciFi is a scintillating fibers grid composed of two layers of 21 5 mm spaced fibers each. The fibers are produced by Saint Gobain Crystal[33] and are coupled to SiPM at each end.

The minimum requests for the properties of the fibers are: high scintillation yield, low decay time, emission spectrum fitting the absorption spectrum of the photosensor, here the SiPM (this point will be discussed in the following section). The information about the specific fiber models considered is collected in Tab. 3.1: they are the fastest models that Saint Gobain produce and all of them were implemented in the simulation.

Scintillating fibers properties

Fiber	Emission Color	Emission Peak [nm]	Decay Time [ns]	1/e Length [m]	No. of photons per MeV
BCF-10	blue	432	2.7	2.2	~ 8000
BCF-12	blue	435	3.2	2.7	~ 8000
BCF-20	green	492	2.7	>3.5	~ 8000

Table 3.1: Saint Gobain scintillating specific fibers properties[33].

It is possible to obtain the models in Tab. 3.1 with a circular or square section: in order to obtain a more uniform response, only square section fibers were considered.

The fibers have a double cladding in order to improve the transport properties: the properties common to all three types of fiber are collected in Tab. 3.2.

In order to consider the saturation of the fibers due to the Birks effect[30], the value measured by Z. Jian-Fu et al.[37] for BC-408[38] has been used. In fact a measurement of this constant in literature for the Saint Gobain BCF fibers seems to be not available. The value used is:

$$k_B = 11.5\frac{\mathrm{mg}}{\mathrm{MeVcm^2}} \tag{3.3}$$

The same value has been used for the simulation of the MatriX detector as well in Ch. 4.

Multi-clad Fibers Properties	
Core material	Polystyrene
Core refractive index	1.60
Density	1.05 g/cm^3
No. of H atoms per cm^3 (core)	4.82 $\times 10^{22}$
No. of C atoms per cm^3 (core)	4.85 $\times 10^{22}$
Radiation length	42 cm
First cladding material	Acrylic
First cladding refractive index	1.49
First cladding thickness	4% of fiber size
Second cladding material	fluor-acrylic
Second cladding refractive index	1.42
Second cladding thickness	2% of fiber size
Cladding material	PMMA ($C_5H_8O_2$)
Cladding material density	1.2 g/cm^3
Trapping efficiency	7.3%

Table 3.2: Saint Gobain scintillating common fibers properties[33].

The emission spectra of the scintillating fibers considered are collected in Fig. 3.4. In order to include the emission spectra in the simulation a webapp named WebPlotDigitizer[39] has been used to convert the images extracted from the datasheet of the fibers in a list of coordinates. The emission spectra extracted this way and used in the simulation are collected in Fig. 3.5.

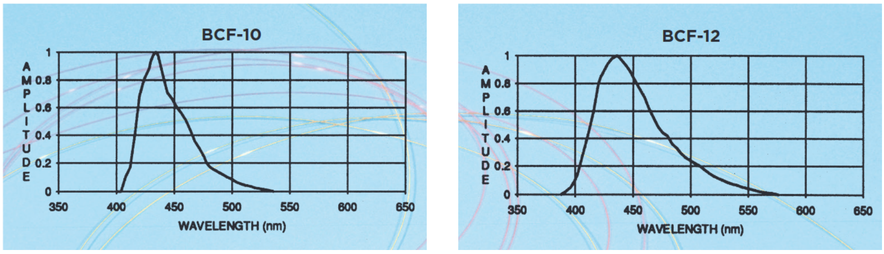

(a) BCF-10

(b) BCF-12

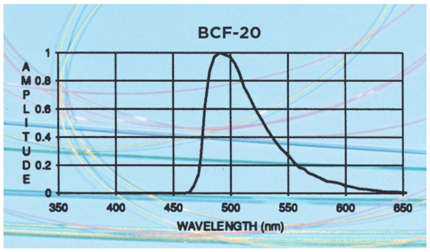

(c) BCF-20

Figure 3.4: Emission spectra of the considered fibers[33].

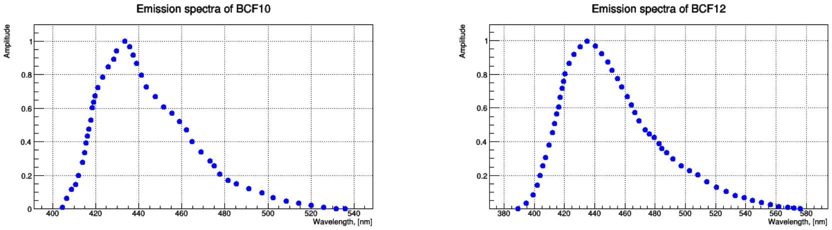

(a) BCF-10

(b) BCF-12

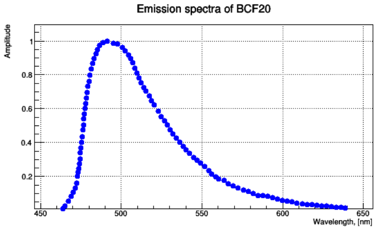

(c) BCF-20

Figure 3.5: Emission spectra of the considered fibers[33] extracted from the images in Fig. 3.4[39].

In the next paragraphs the first sanity checks on the simulation and the transport properties of the fibers will be discussed.

3.2.2 Sanity checks

In order to verify the correct functioning of the fiber modeling, simulations with the following specifications have been run:

- the fiber is hit perpendicularly at its center by primary particles;
- fiber sizes: 0.25 mm, 0.50 mm, 1.00 mm;
- fiber materials: BCF-10, BCF-12, BCF-20;
- primary particles: 2.2 and 52.8 MeV kinetic energy e^+, 70.5 MeV/c momentum π^-, 28 MeV/c momentum μ^+.

Fig. 3.6 collects the energy deposit mean dependence on primary particle $\beta\gamma$ and mean deviation due to multiple scattering dependence on primary particle momentum, as extracted from simulations.

The mean energy deposit is the arithmetic mean of the ratio between the energy deposit and the track length inside the fiber. Each sample is 10^3 events long.

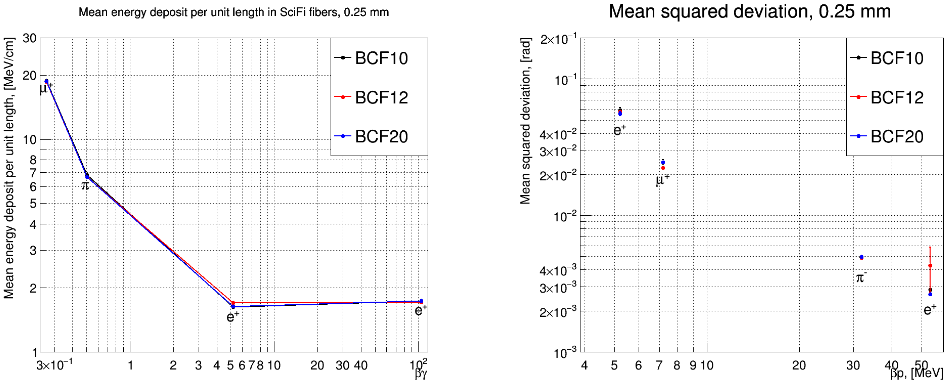

(a) 0.25 mm, mean energy deposit

(b) 0.25 mm, mean squared deviation

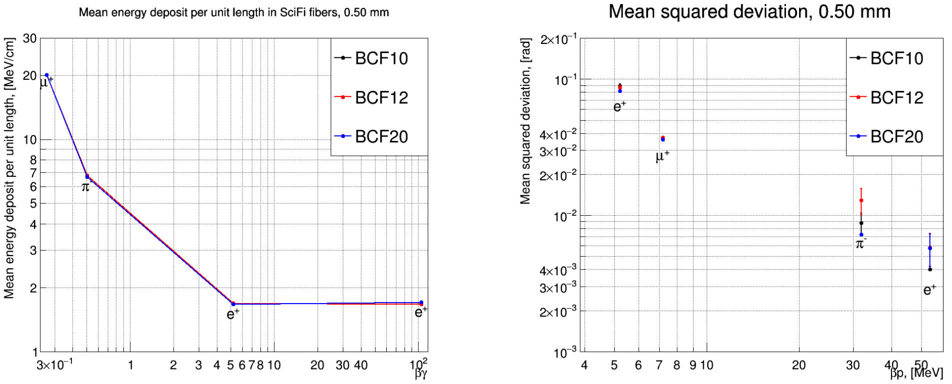

(c) 0.50 mm, mean energy deposit

(d) 0.50 mm, mean squared deviation

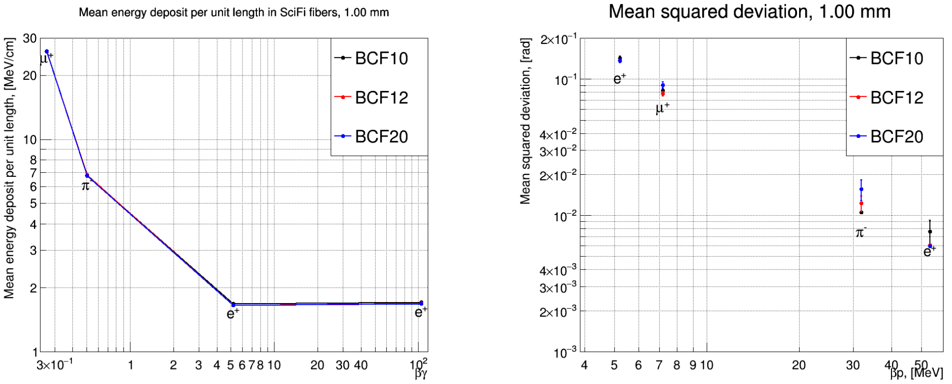

(e) 1.00 mm, mean energy deposit

(f) 1.00 mm, mean squared deviation

Figure 3.6: *Sanity checks for fibers modeling. The left panels collect the mean energy deposit per unit length at different $\beta\gamma$. The right panels collect the mean squared deviation of primary particles through fibers at different momenta. From top to bottom the panels refer to fibers with the following widths: 0.25 mm, 0.50 mm and 1.00 mm.*

3.2.3 Escaping photons fraction

Geant4 allows to treat the surfaces of volumes as non-polished. It is possible in fact to model a surface as not perfectly smooth but with stochastic impurities. The GLISUR model has been used, which allows to represent ground surfaces changing locally the orientation of an interface when an optical photon hits it. This model is parameterized through a variable whose name is *polish*: when *polish* is less than one, the surface is not polished. The values used in my simulation where measured by A. Papa[40].

- 0.985 between the core and the first cladding;
- 0.98 between the first and the second cladding;
- 0.5 between the second cladding and the outside volume (vacuum).

Fig. 3.7 collects the number of photons escaping the fiber through the end surfaces as a function of the fiber length. The primary particles used for these simulations are 2.2 MeV initial kinetic energy positrons. Each sample is 10^3 events long.

In each sample the emitted photon number distribution has been fitted with a Landau. Than the arithmetic mean of the ratio between the number of escaping photons and the total number of photons emitted was calculated. At the end the value obtained and the most probable value of the fitted Landau were multiplied. Fig. 3.7 collects only the results of the BCF-10 simulations: the results of the BCF-12 and BCF-20 fibers are collected in Ap. A.

The light output dependence on the fiber length has been fitted with the sum of two exponentials if the fiber was polished. If the fiber was non-polished, the fitting function was the sum of three exponentials. This exponential model actually is an easy phenomenological description of more complicated and hard to describe processes. Light propagates inside a fiber primarily via total internal reflection at the core-cladding, or cladding-cladding, interface. The main processes involved in light loss are: impurities at the interfaces, roughness, non-perfect fusion at the core-cladding interface and absorption inside the fiber core (Rayleigh scattering, chemical impurities and/or radiation induced traps).

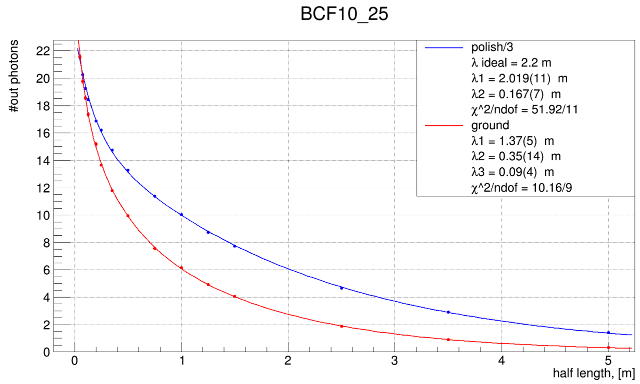

(a) 0.25 mm wide

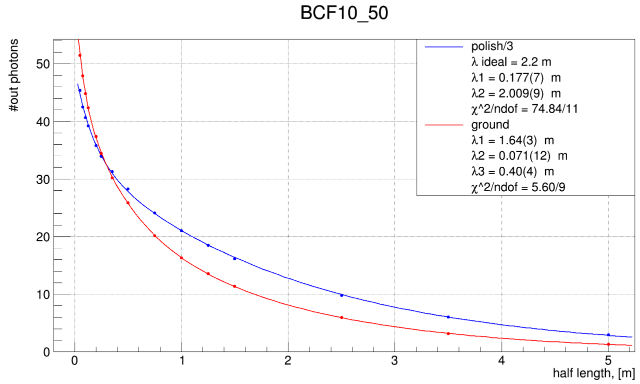

(b) 0.50 mm wide

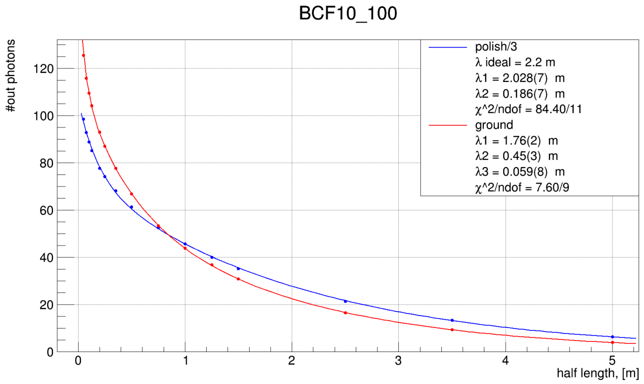

(c) 1.00 mm wide

Figure 3.7: *Light output of BCF-10 fibers as a function of fiber length. In blue the values, divided by a factor 3, related to the polished version of the fibers, while in red the values related to the non-polished version of the fibers. The blue fitting function is the sum of two exponentials. The red fitting function is the sum of three exponentials.*

As already mentioned, these processes can be modeled using a number of absorption lengths: the higher one is expected to be of the order of the bulk absorption length, while the lower ones depend on the amount of light promptly emitted towards the ends of the fiber.

In the simulation presented here only surfaces imperfections and bulk absorption are considered.

3.3 SiPM

A Silicon Photomultiplier (SiPM) is a solid-state photon sensor with the capability of detecting single photon[41]. The performances of the SiPMs are comparable to the photomultiplier tubes ones, with the advantage of insensitivity to high intensity magnetic fields, compact sizes, low operation voltage and good timing performance. SiPMs are used as photon sensors in the MEGII experiment pTC, LXe calorimeter, SciFi beam monitor, (MatriX) and DS RDC. In the next paragraphs the working principle and the signal modeling implementation in my simulation will be discussed.

3.3.1 Basic introduction and working principle

SiPMs consist of a matrix of typically $\mathcal{O}(1000)$ independent micro-cells (pixels) wich are connected in parallel[42]. Each pixel is formed out of a photodiode (APD, avalanche photodiode) and a quench resistor in series. The photodiode is operated a few volts above the breakdown voltage so that when a photon is absorbed in the depletion region an electrical breakdown occurs: the primary charge carriers (photoelectrons) are amplified (through Geiger discharge) with a high gain (G$\simeq 10^6$). Then the charge flows through the quenching resistor, restoring the initial condition. The output signal is proportional to the number of activated pixels.

APD physics

An APD is a diode that exploits high bias voltages in order to obtain high output signals following photoelectric events. This is possible due to the presence of a p-n junction and of an external reverse-bias voltage V_{bias}. Fig. 3.8 shows the typical p$^+$-p-n construction of an APD [43].

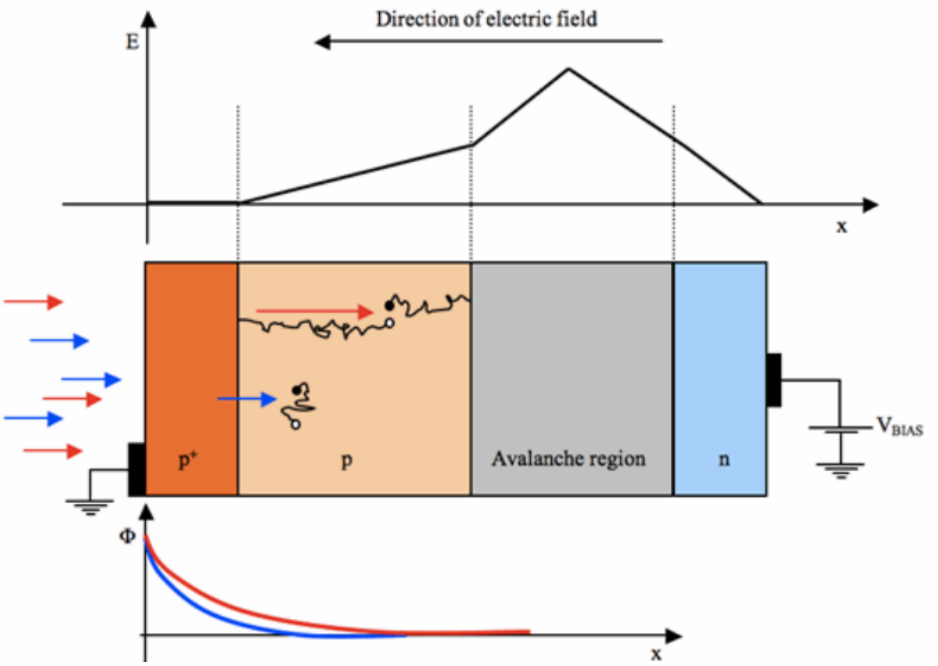

Figure 3.8: *Typical p$^+$-p-n construction of an APD[43]. In order from top to bottom: electric field profile in an APD due to p-n junction and reverse-bias voltage; APD scheme; photon flux vs depth scheme.*

When a photon, incident on the p$^+$ side, has an energy higher than the band gap energy E_G of the semiconductor used to manufacture the APD (typically silicon with E_G = 1.1 eV), an intrinsic photoelectric effect can occur, producing electron-hole e-h pairs. The characteristic depth of photon absorption depends on the type of the semiconductor and the wavelength of the light. Photon flux as a function of the depth z is:

$$\Phi(\lambda, z) = \Phi(\lambda, 0)e^{-\alpha(material,\lambda)z} \tag{3.4}$$

where λ is the wavelength of the photon and α is the absorption coefficient, whose inverse

δ is the penetration depth. α depends on the material and on λ. Fig. 3.9 shows the absorption dependence on wavelength for different semiconductors[43].

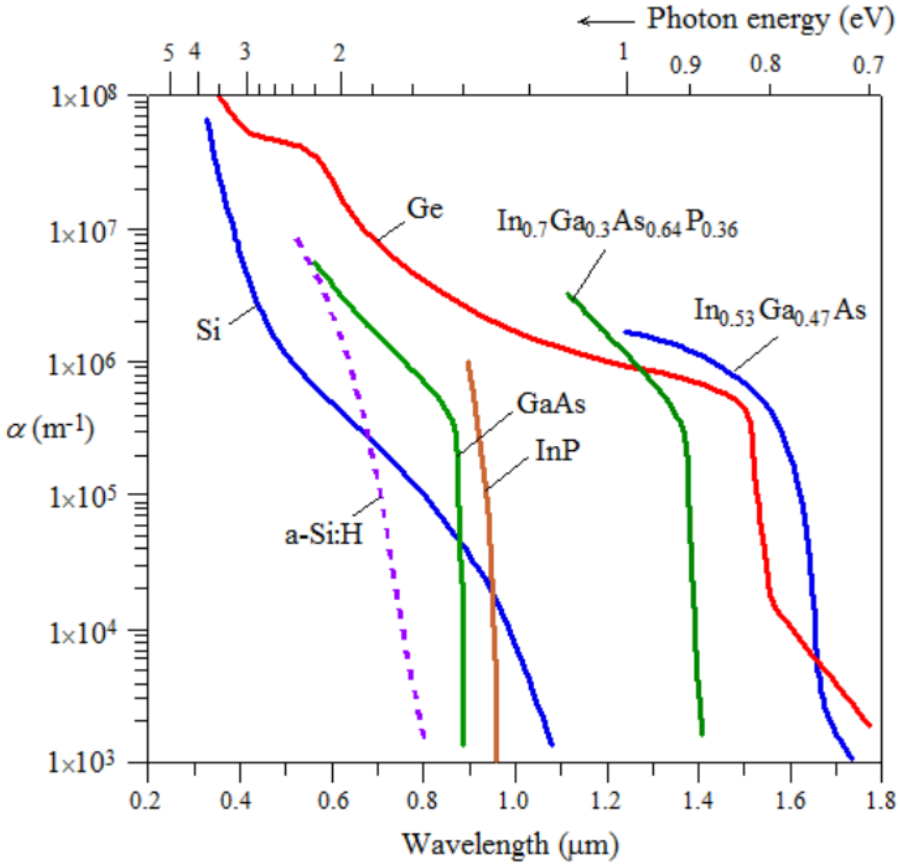

Figure 3.9: *Absorption coefficient, α, as a function of wavelength of incident light (bottom abscissa) or energy (top abscissa)[43].*

α decreases as the wavelength increases, so that, for lower energies the penetration depth is higher. In the visible spectrum δ varies from 0.08 μm (400 nm) to 3 μm (600 nm) (Fig. 3.9).

If an e-h pair is produced in a heavily doped p$^+$ region where the electric field is weak, the pair is likely to recombine non radiatively (thorough phonon ”emission”). If an e-h pair is produced close to or in the depletion region: here the electric field is strong enough to separate the pair and make the electron move toward the n region and the hole move towards the p$^+$ region. Due to lack of free charge carriers, in the depletion region the e-h is not likely to recombine, producing an electrical signal in the circuit containing the detector. The photon was detected.

The quantum efficiency, $\eta(\lambda)$, is defined as the ratio of the number of photo-generated e-h pairs per unit time, n_{e-h}, that produce an electrical signal, to the number of incident photons on a photo-sensitive surface per unit time, n_λ.

$$\eta(\lambda) = \frac{n_{e-h}}{n_\lambda} \tag{3.5}$$

Depending on V_{bias}, there is the possibility for the e-h pairs to trigger an avalanche: depending on the strength of the electric field in the depletion region, the electron or the hole can gain enough energy to produce other e-h pairs in the depletion region. This leads to an amplification of the output signal: the APD output current I_{APD} is related to the single e-h pair output current I_{ph} through the following equation:

$$I_{APD} = M \cdot I_{ph} \tag{3.6}$$

where M is the APD gain. Fig. 3.10 shows the gain M as a function of the bias voltage V_{bias}.

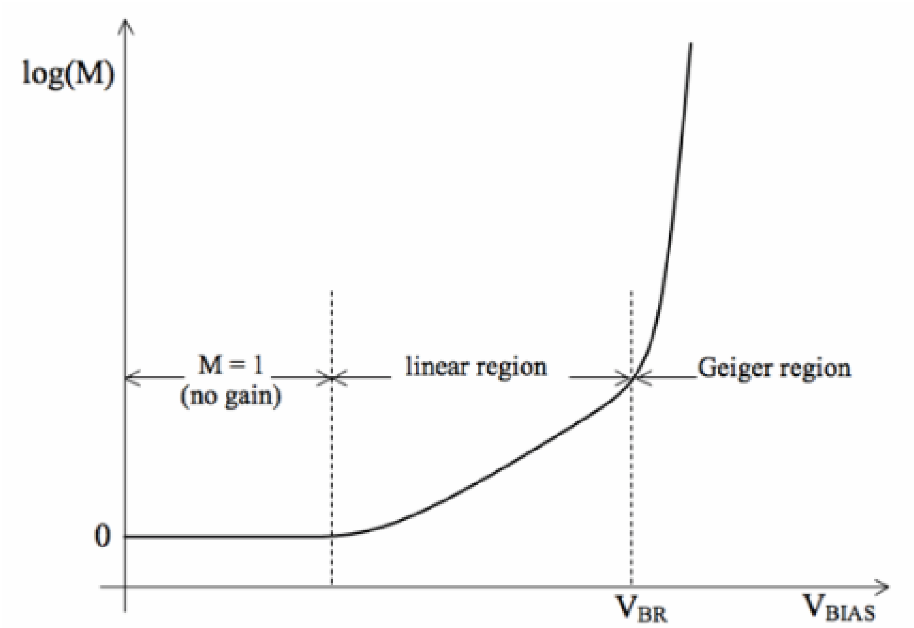

Figure 3.10: *APD gain M as a function of* V_{bias}*[43].*

There are three distinct regions in Fig. 3.10. In the ”no gain” region, M = 1 and the APD operates as a photodiode.

In the linear region, log(M) is linearly proportional to V_{bias}: here the charge carriers gain enough energy to ionize a lattice atom. The avalanche eventually ceases and the output signal gives information about the number of photons revealed.

In the Geiger region, the avalanche doesn't stop, it is self-sustained. In a steady state, the number of newly created pairs is equal to the number of pairs collected at the electrodes. To extinguish the avalanche it is necessary to reduce V_{bias} to at least V_{br} (the breakdown voltage). This way any information about the number of impinging photons is lost, the only information obtained is whether a photon was detected or not.

A SiPM is a matrix of APDs in parallel, all operating in Geiger mode: the output signal is then proportional to the number of fired pixels.

Electrical model and dynamic range

Due to its characteristics, a SiPM has a dynamic range whose upper limit is the total number of pixels. In fact, after a discharge, a pixel can't immediately reveal a photon. An electrical model for SiPM was produced by F. Corsi et al.[44] as shown in Fig. 3.11[41].

The SiPM is modeled by parallel connection of a firing pixel with the other inactive pixels. Each pixel is modeled by series connection of a switch and a quench resistor (R_q). Due to the small distance between the quench resistor and the diode, the parasitic capacitance between them (Cq) is not negligible. C_{pxl} is the pixel capacitance, C_s is the parasitic capacitance between the bias distribution lines on the SiPM surface to the silicon substrate. R_d is the diode resistance. R_s is the readout resistor, to convert the output current to voltage signals. R_{bias} and C_{bias} represent the biasing circuit and have typical values of 10 kΩ and 100 nF.

In Fig. 3.11, the inactive pixels are represented by a single inactive pixel with a quench resistance $R_{q,n} = R/(N-1)$, a parasitic capacitance $C_{q,n} = (N-1) \cdot C_q$ and a pixel capacitance $C_{pxl,n} = (N-1) \cdot C_{pxl}$, where N is the total number of pixels in the SiPM.

In Tab. 3.3 are collected the typical values of the electrical model components[45].

When a photon is absorbed, a photoelectron is emitted in the depletion region. In the electrical model this correspond to closing the switch S in the firing pixel. When the switch is closed, the voltage at node X V_x is V_{bias}, the voltage at the output is 0 and the current through R_d jumps to (V_{bias} - V_{br})/R_d. The charge stored in C_{pxl} discharged with a time constant

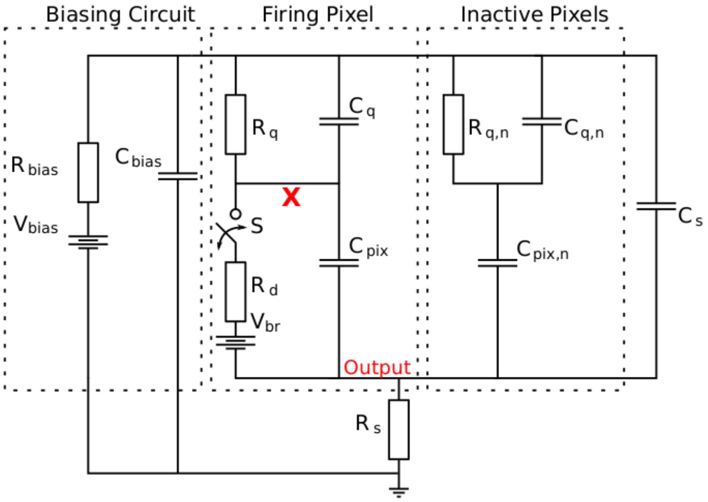

Figure 3.11: *Equivalent circuit of a SiPM[41].*

C_{pxl}	C_q	C_s	C_{bias}	R_d	R_q	R_{bias}	R_s	N
83.88 fF	5 fF	35 pF	100 nF	1 kΩ	150 kΩ	10 kΩ	50 Ω	1600

Table 3.3: Typical values of electrical model components for the Hamamatsu MPPC S13360 series[34][45].

$\tau_q \sim R_d \cdot (C_{pxl} + C_q)$, causing V_x and I_d to drop. When I_d goes below a few μA, the avalanche in the pixel quenches and S opens. Then, restoring V_{bias} at the X node needs a higher amount of time: for this process the time constant is $R_q \cdot (C_{pxl} + C_q)$, which is two orders of magnitude larger than τ_q (Tab. 3.3). The output voltage will have a tail depending on the pixel recovery time and on $R_s \cdot C_s$ as well.

As a reference, Fig. 3.12 shows the simulation based on this model by H. Chen [41]: they are base on the components of an S13360 3×3 mm^2 sensor size, 50 μm pixel pitch MPPC from Hamamatsu[45] (values in Tab. 3.3).

The SiPMs used in SciFi are from the same series simulated in Fig. 3.12, S13360, but a different model: 1.3×1.3 mm^2, 50 μm pixel pitch MPPC with a silicon resin window.

The typical recovery time for a pixel, based on the electrical model, is $\sim$ 13 ns. In the simulation a rejection window 20 ns long to emulate this effect has been considered.

The dependence of the number of pixels fired on the number of photons (here assumed to

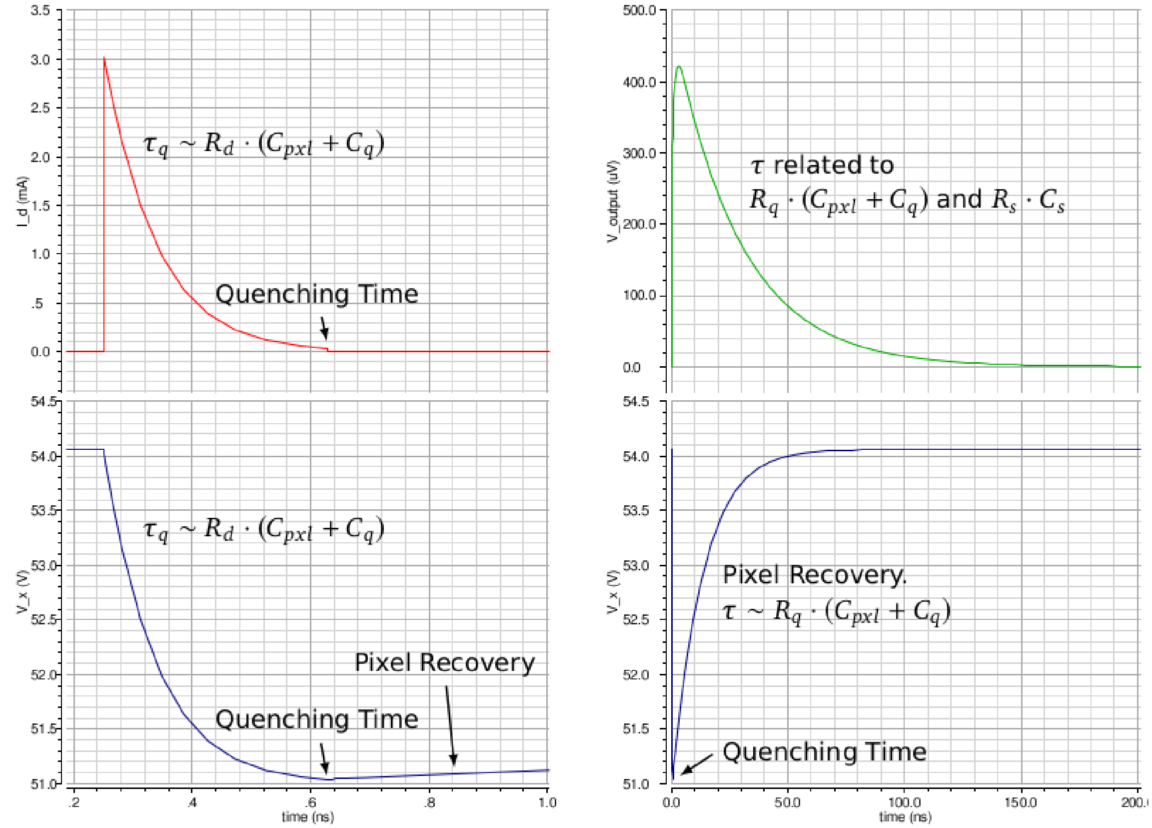

(a) I_d(up) and V_x(down) waveforms around the quenching time.

(b) V_{output}(up) and V_x(down) waveforms.

Figure 3.12: *SiPM response from simulation using the SiPM electrical model[41].*

be arriving homogeneously and simultaneously at the surface of the SiPM) is[41]:

$$N_{fired} = N_{pixel} \cdot (1 - e^{-\frac{N_{photon}\varepsilon_{PDE}}{N_{pixel}}}) \tag{3.7}$$

where N_{fired} is the number of fired pixels, N_{pixels} is the total number of pixels composing the SiPM, N_{photon} is the number of photon to be revealed and ε_{PDE} is the photon detection efficiency of the sensor. In Eq. 3.7 ε_{PDE} is assumed to be the same for all the arriving photons, but actually it depends on the photon wavelength.

In SciFi this saturation effect is completely negligible: the number of photons reveled by each of the SiPMs at the end of the fibers, is ~ 10, while the total number of pixel in an S13360-50CS Hamamatsu SiPM is 667. This effect won't be negligible for the MatriX detector, which collects higher amounts of light, and that will be described in the next chapter.

Dark noise events

A pixel can be activated even following the e-h pair production due to thermal processes: in fact, for an APD in Geiger mode, it is sufficient a single e-h pair to trigger the avalanche. Of course a single photon event can't be distinguished by this kind of processes, which is known as dark noise.

The rate for these events to happen depends on the SiPM model and on the operating temperature. The dark noise rate for an S13360-1350CS Hamamatsu SiPM is in the order of 90 kHz[34]. In the simulation, this effect has been implemented on a SiPM to SiPM basis: this will be discussed in detail in the following paragraphs.

3.3.2 Implementation specs

To simulate the SciFi detector, the program has been split into two different parts: one is implemented using the Geant4 toolkit and simulates the physics of the detector; one is a macro that processes the Geant4 level output in order to simulate the signals waveforms as they would be detected by the WaveDream boards[5].

Fig. 3.13 shows the Geant4 level flowchart of SciFi.

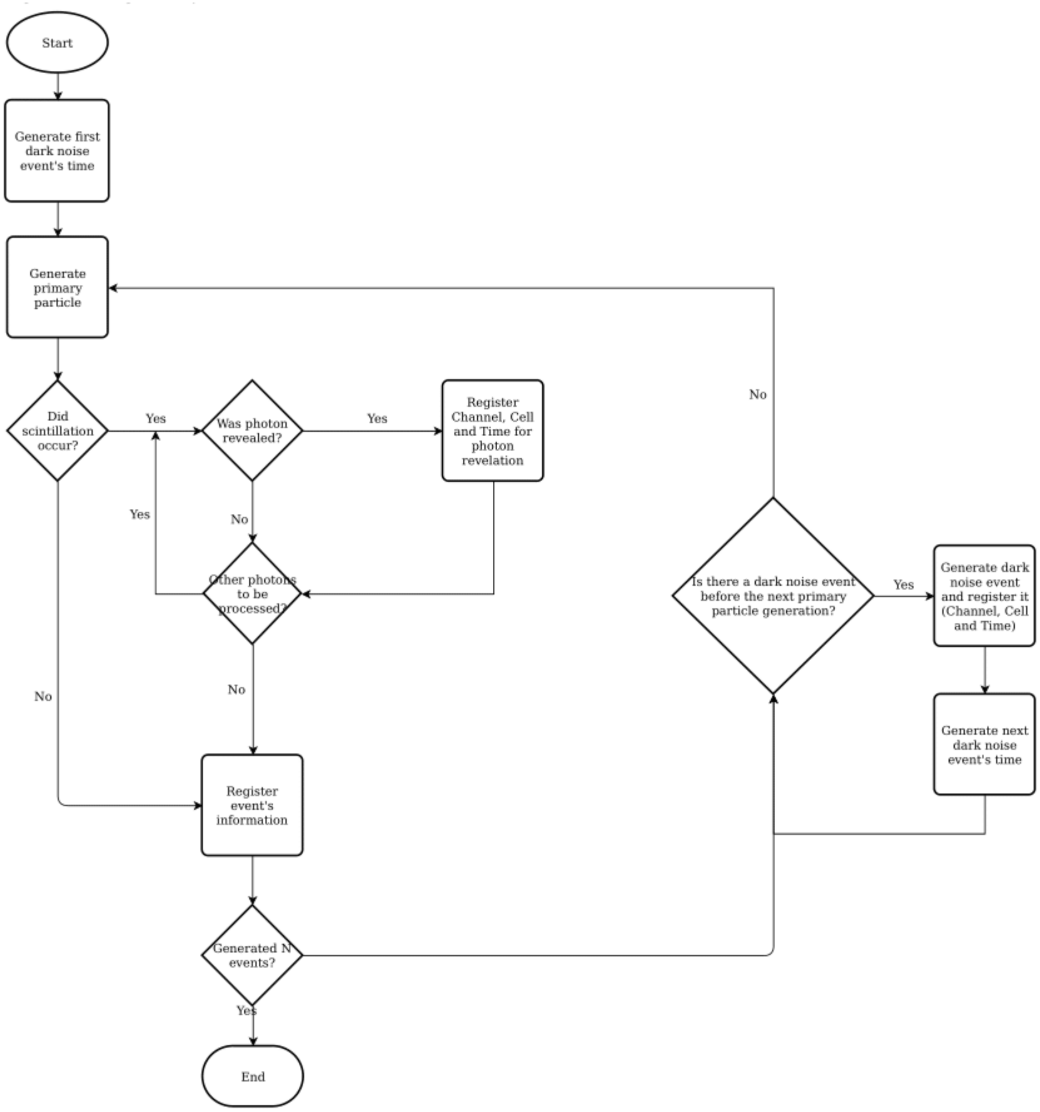

Figure 3.13: *Flowchart of the Geant4 level simulation of SciFi detector.*

The first think that the code does is to extract randomly the time of the next dark noise event for each of the SiPM in the detector (in the complete detector they are 84) by sampling an exponential distribution function, with a decay constant which is equal to 90 kHz (the mean dark noise rate for S13360-1350CS Hamamatsu SiPM[34]). Actually the dark noise events are generated at the beginning of the next events, so that the first event generated is always a signal one.

Then the first primary particle (μ^+, e^+ or π^-) is generated: in single fiber simulations the particles are always generated at the center of the fiber, along the z axis (Fig. 3.14); in complete detector simulation the beam is distributed in space sampling a bidimensional Gaussian whose width and position can be changed from command line.

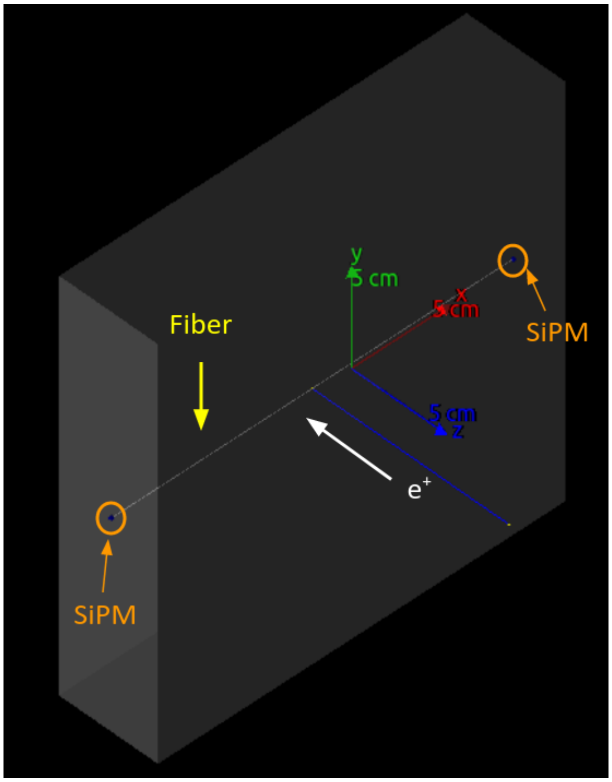

Figure 3.14: *Single fiber simulation event: e+, along z axis, passing through the fiber at its center.*

If scintillation occurs and a photon reaches the surface of a SiPM, it is checked whether it is detected or not. This of course depends on the photon energy and on the SiPM ε_{PDE}: Fig. 3.15 shows the PDE of an S13360-1350CS Hamamatsu SiPM, in red, as a function of the wavelength of the photon[34]. It is actually the product of the quantum efficiency and of a term which takes into account the effective detection area of the single pixel, named fill factor: it is the ratio between the effective area and total area of the single pixel. The PDE of the S13360-

1350CS SiPM completely contains the emission spectrum of the BCF fibers (see Fig. 3.4 and 3.15).

Using WebPlotDigitizer[39] the PDE has been extracted to use it into the simulation: when a photon arrives on the SiPM surface, it is found the most close point in wavelength on the extracted PDE. Then a number between 0 and 1 is extracted sampling a uniform distribution: if the number extracted this way is lower than the PDE value, the information about the photon are saved (such as the pixel fired, the channel and the time of absorption). Whether the photon is detected or not, it is killed in the following step.

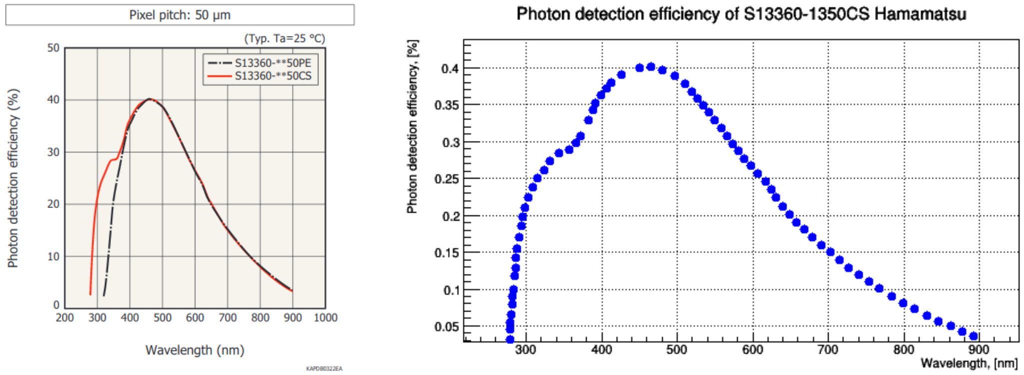

(a) PDE in the datasheet

(b) PDE extracted from the one on the left

Figure 3.15: *Photon detection efficiency as a function of incoming photons of an S13360-1350CS Hamamatsu SiPM. On the left the PDE as shown in [34]. On the right the PDE as extracted using WebPlotDigitizer[39].*

In the simulation the SiPM is composed of two volumes: the pixel volume, which is a unique box made of Silicon; the window, which in the CS models is made of a ceramic material (silicon resin) but in the simulation is an empty space with a refractive index equal to 1.41. Only the optical properties of the window has been introduced, because of their role for the transport of the photons.

In Tab. 3.4 the sizes of the SiPM are collected, while Fig. 3.16 and 3.17 show respectively the SiPM dimensional outlines as reported in [34] and the simulated sensor.

SiPM height [mm]	SiPM width[mm]	Pixel volume height [mm]	Window height [mm]
1.5	1.3	1.0	0.5

Table 3.4: SiPM sensor size[34].

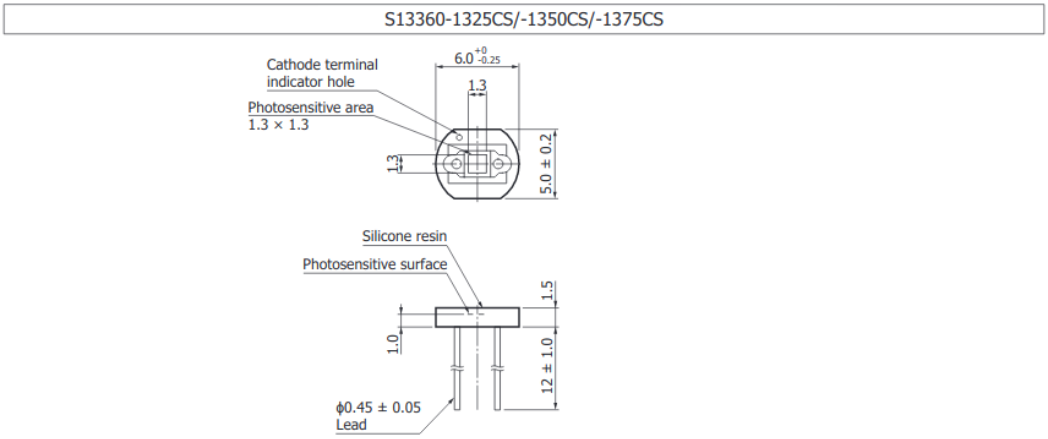

Figure 3.16: *Dimensional outlines of an S13360-1350CS Hamamatsu SiPM[34].*

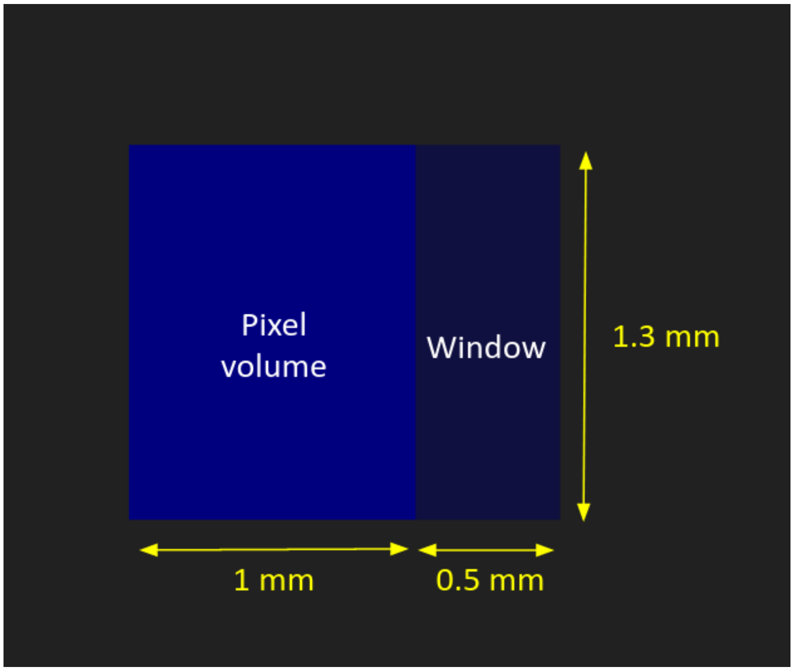

Figure 3.17: *Simulated S13360-1350CS Hamamatsu SiPM.*

After checking on each scintillation photon detection the event ends and all the information collected is saved in the output tree. If the number of events is less than the one requested the cycle restarts, but from the second event on there is an additional step: before the scintillation photons arrive on the SiPM surface it is checked whether there is a dark noise event or not. If yes, it is saved as it would be done for a detected photon and the next dark noise event time within the same SiPM is extracted. Then the cycle is restarted until the next dark noise event happens after the current primary event. If not the primary event starts.

There is a global variable in the simulation that takes into account the amount of time passed starting from the first event: it is named *GunTime*. In fact at each event the time of the next one is extracted sampling an exponential distribution with a slope equal to the beam rate, which can be set from command line.

Fig. 3.18 shows the distribution of the hit of the photons on a 50 μm pitch SiPM. The photons are produced after the passage of a 28 MeV/c momentum muon through a 250 μm sized fiber.

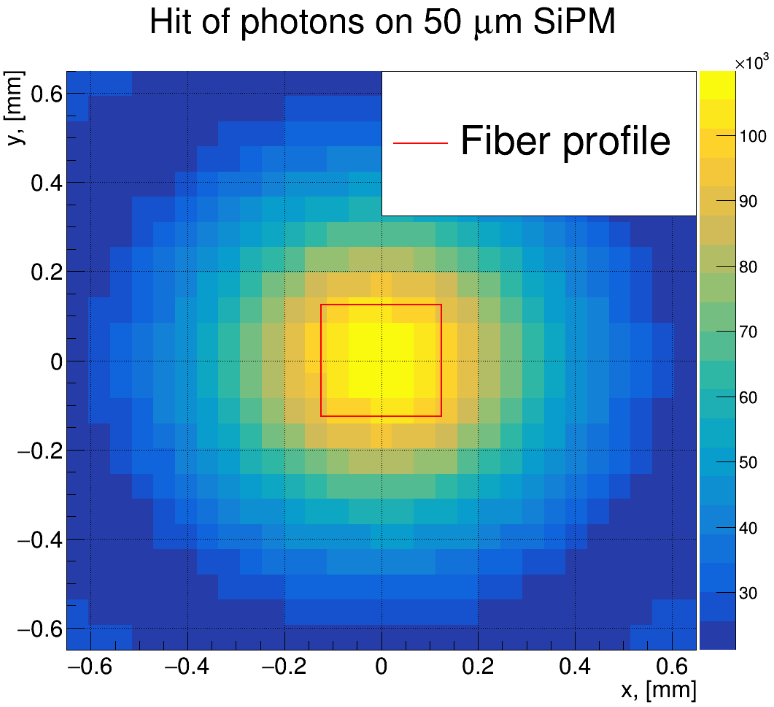

Figure 3.18: *Photons hit on 50 μm pitch SiPM. The red square represents the size of the fiber with respect to the SiPM active area.*

3.3.3 Signal simulation

Single photoelectron waveform

The waveform coming from a single pixel firing in the SiPM is shaped basing on data. Fig. 3.19 shows the waveform of a single photo-electron as measured by a WDB with Pole Zero Cancellation (PZC, varies from 0 to 7, see Ch. 1) 5: the possible values to be used in the final version are 4 or 5. The time division is 10 ns wide. The amplitude division is 30 mV high. The WebPlotDigitizer[39] has been used to extract the points from the image. Then the signal has been fitted with an exponential folded with a Gaussian. It is not trivial to compare the parameters obtained through the fit with the expected rising and falling time for a SiPM signal due to the presence of PZC. The fine tuning of the MC simulations was expected to be done during the MEGII beam tuning pre-eng 2020 originally planned for June and currently shifted to September due to COVID-19 pandemic. The ideal thing, in order to obtain a good agreement between the detector response and the simulation, would have been using a sum of single photo-electron signals (dark noise events) at different PZC values to be fitted with an effective function. This should have been followed by a study of linearity in response with higher photo-electron number events: using ^{39}Sr for example. In this thesis a focus on the detector simulation itself has been given, the Geant4 level, instead of on the electric response side, and at this level it is not needed a fine tuning on the signal shaping: the waveform used is shown in Fig.3.19.

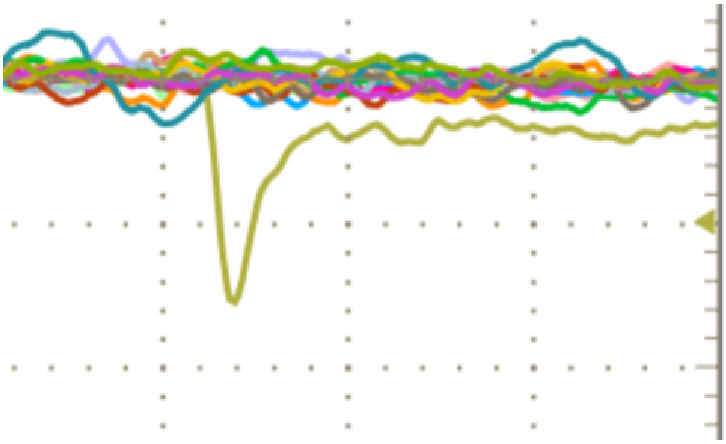

Figure 3.19: *Single photo-electron waveform measured through WDB with PZC 5.*

In order to avoid the pedestal on the left of Fig. 3.19, the fit has been performed only around the peak, where the noise effect is negligible. The fitting function is:

$$f(x) = A\left(C(x - x_{pos}, \tau_{rise}, \sigma_{gaus}) - C\left(x - x_{pos}, \frac{\tau_{rise}\tau_{fall}}{(\tau_{rise} + \tau_{fall})}, \sigma_{gaus}\right)\right) + offset \quad (3.8)$$

with τ_{rise} the rising time, τ_{fall} the falling time, σ_{gaus} the gaussian width, A a multiplicative constant and x_{pos} a positioning value. The C function is defined as:

$$C(x, a, b) = b\sqrt{2\pi}\exp\left(\frac{b^2}{2a^2} - \frac{x}{a}\right)\left(\mathrm{erf}\left(\frac{ax - b^2}{ab\sqrt{2}}\right) + 1\right) \quad (3.9)$$

Tab. 3.5 and Fig. 3.20 show the results of the fit. The fit is performed without errors on the signal points.

τ_{rise} [ns]	τ_{fall} [ns]	σ_{gaus} [ns]
1.58 ± 0.07	0.57 ± 0.03	0.50 ± 0.03
A [mV]	x_{pos} [ns]	$offset$ [mV]
-69.4 ± 0.6	2.76 ± 0.04	2.5 ± 1.4

Table 3.5: Fitting parameters.

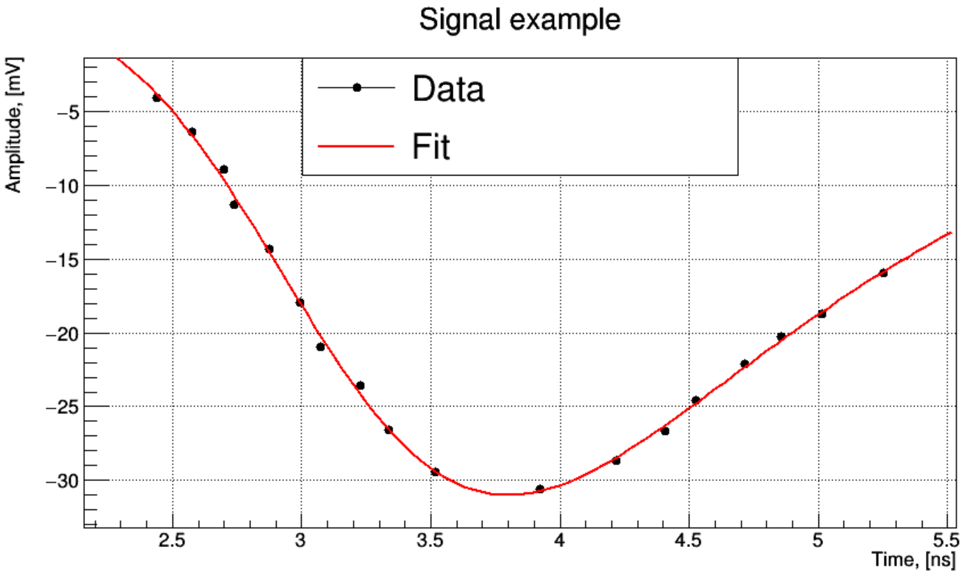

Figure 3.20: *Single photo-electron signal fit. The parameters are collected in Tab. 3.5.*

τ_{rise} [ns]	τ_{fall} [ns]	σ_{gaus} [ns]
1.58	0.57	0.50

A [mV]	x_{pos} [ns]	$offset$ [mV]
2.07	1.5	0

Table 3.6: Parameters used in the simulation.

The parameters used in the simulations are collected in Tab. 3.6.

A smearing effect on the single photo-electron waveforms has been introduced: the effect of electric noise has not been considered but the amplitude of the waveforms was sampled using data taken during PSI Summer Program 2019. First photo-electron signal amplitude spectrum was measured using Dark Noise events with PZC 0 value, assuming that the effect would be the same with higher PZC values. The SiPM used is a S13360-50PE Hamamatsu[34]. Fig. 3.21 shows the data, on the right panel, fitted with a skew Gaussian: the tail on the left is an exponential function ($\tau = (1.6 \pm 0.4) 10^{-4}$ a.u.) connected to a Gaussian ($\sigma = (5.98 \pm 0.12) 10^{-3}$ a.u.) analytically. The data are scaled so that the mode of the distribution is 1.

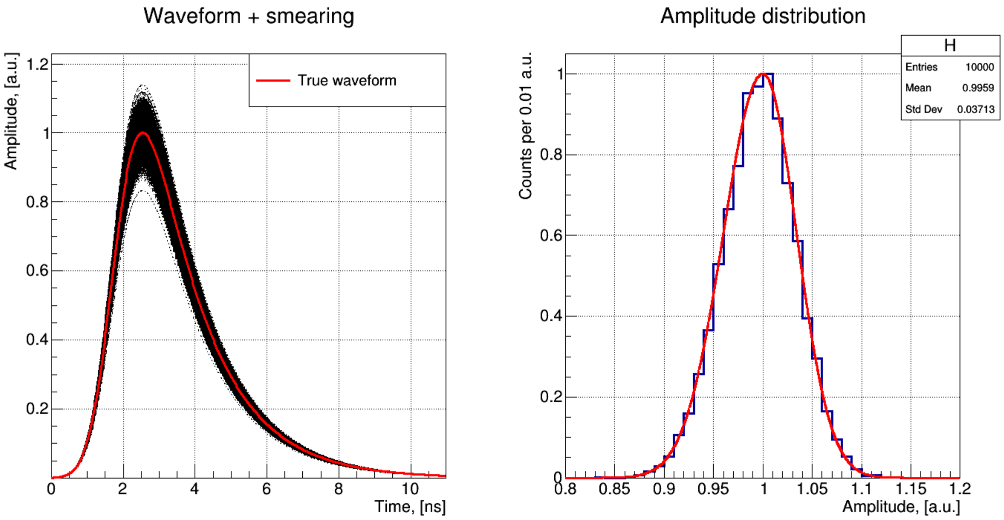

Figure 3.21: *Single photo-electron amplitude distribution: on the left the measured distribution fitted with a skew Gaussian; on the left a comparison among the true waveform and the sampled ones.*

On the left panel there are 10^4 waveforms with amplitude sampled through the fitted function: the sampling is performed through the *GetRandom()* method of *TF1* ROOT objects[8].

Channel waveform

After the Geant4 simulation ends, the output file contains information about the whole event and about the single detected photons, but the macro that elaborates the signals uses only the information about the single photons detected. The macro is written in C++ and it includes libraries from the toolkit ROOT[8]. The first step is to order temporary the arrival time of the photons on the SiPM surface. Due to the structure of the Geant4 simulation, the output is already partially ordered: the single photons information stored during an event is stored in vectors that are filled on a temporal basis hierarchy, so that the first photons revealed are the first to be stored. This means that it isn't necessary to order all the events at once, but instead it is possible to order the information about a smaller group of events. The routine that orders the output is structured as follows:

1. the information about photons coming from the first 100 events is stored and ordered;
2. the first half of the ordered events is stored in a new file, while the remaining data are saved in a buffer;
3. the data stored in the buffer are merged with the next 100 events information and ordered;
4. the second and third steps are repeated until the file ends.

Of course the number of events in these "packages" may vary according to the beam rate: the typical amount of time needed for the photons to arrive is of the order of 10 ns. In order to obtain long enough packages it is necessary to cover a period of time that's longer than the typical arrival time of photons. This way, considering packages containing 100 events, the ordering works up to rates of the order of:

$$R \sim \frac{100}{10ns} = 10^{10} Hz \tag{3.10}$$

As will be discussed much more in detail later, this rate is actually more than two orders of magnitude higher than the maximum rate registered on a single fiber: at the collimator in the

ΠE5 line, the beam has a $\sigma \sim 20$ mm which means that there are almost 2 orders of magnitude between the beam rate and the hit rate on the central fibers. The highest beam rate is the one of the positron beam with completely opened slits and it is of the order of 10^9 Hz. Specific tests on the output confirm that using this algorithm produces a temporary ordered output.

Then the information about the photons are divided by channels (SiPMs) and all the photons detected by a SiPM fired in a 20 ns window are rejected (see Fig. 3.12 (b)): this allows to create single channel waveforms as they would be measured with an oscilloscope.

In fact the last step is to form the signals and save their characteristics. At the beginning of the routine two vectors are created: *signal* and *signalT*. The first one represents the amplitude of the signal at a given moment. The second one represents the time. They have the same size and each *signal* element is related to the *signalT* element with the same position index: *signalT.at(i)* is the time at which the amplitude is *signal.at(i)*.

In the beginning, the two vectors are filled: *signalT* corresponds to a time window 200 ns long divided in 0.1 ns bites; *signal* is filled with zeros. It is possible to set a threshold in amplitude in order to select the waveforms to be saved: the default value is 0.5 a.u. (1 corresponds to the maximum of a single photoelectron signal). The threshold is checked only at the central values of *signal* and *signalT*: these are the values at the center of the considered time window. The threshold is checked at the central value of *signal* instead of the first one for debugging reasons: this way, if there is any error in the output, it is also possible to check the previous event.

The routine is structured as follows:

1. the next photon arrival is read from file;
2. the time window slides at 0.1 ns bites:
    (a) *signal.at(0)* and *signalT.at(0)* are erased;
    (b) the sum of the signals amplitude in the next point to be added is calculated based on the previous photons arrival times. This value is named *Amplitude*;
    (c) *Amplitude* is added to the bottom of *signal* and the next temporal step is added to the bottom of *signalT*;

    (d) if the central value of *signal* is higher than the threshold, basic information about the signal are saved in the output: amplitude, time at which the signal passes over the threshold. Other information about the corresponding event is saved for debugging reasons, such as the number of the event;

    (e) steps from (a) to (c) are repeated until the next element to be added in *signalT* is greater than the arrival time of the next photon.

3. the arrival time of the photon is saved in a buffer and will be used to evaluate the signals in the next cycles;

4. after 400 steps, the arrival time is erased from the buffer: this choice is made to reduce the amount of memory to be used by the macro. As shown in the previous paragraph, 40 ns it's enough to consider the pixel to be turned off.

The cycle is repeated until the end of the file and the waveforms are processed separately for each channel.

Fig. 3.22 shows an example of waveform.

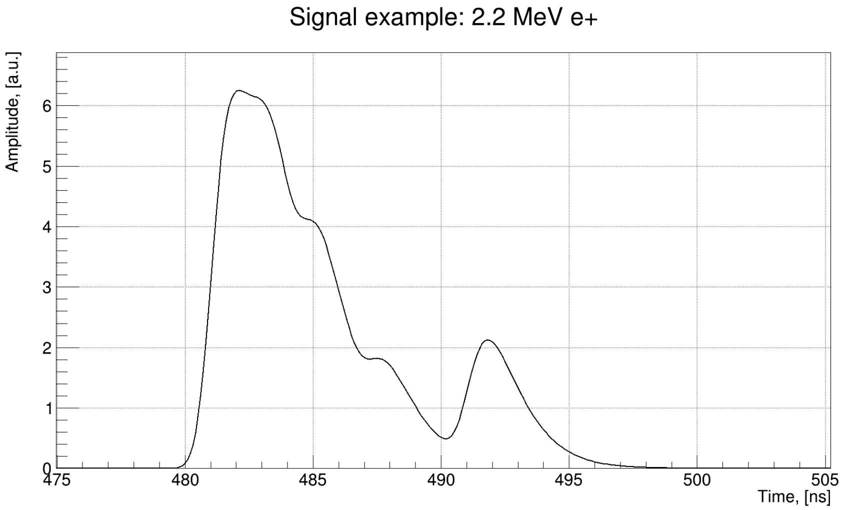

Figure 3.22: *Example of waveform obtained with the simulation. This waveform follows the passage of a 2.2 MeV positron through a BCF-10 fiber.*

3.4 Single fiber rate reconstruction

The saturation caused by a high rate of primary particles passing through a fiber has been evaluated: the saturation arises because of the dead time after the coincidence between the SiPMs at the end of the same fiber. Simulations have been run at different beam rates, using a perfectly centered monochromatic 2.2 MeV kinetic energy positron beam along the axis of the fiber. Each run is 10^5 events long with the Dark Noise events turned off.

Knowing the dead time window length and the fibers rate, it is possible to evaluate a correction factor to obtain a better estimation of the number of primary particles passing through the fibers per unit time.

The expected measured rate is:

$$R_{exp} = R_{real} \exp\left(-R_{real} \times \Delta T_{dead}\right) \tag{3.11}$$

Fig. 3.23 shows the effect of the dead time on the rate of a single fiber.
It is possible to correct this effect. The easiest thing that can be done is to evaluate the values of the following succession:

$$a_{n+1} = R_{meas} \exp\left(-a_n \times \Delta T_{dead}\right)$$

with R_{meas} the rate measured on a single fiber and $a_0 = R_{meas}$. The aim is to obtain a value that satisfies eq. 3.11: the algorithm is stopped when the difference between a_{n+1} and a_n is lower than 10^{-5}. Fig. 3.24 shows the effect of this correction on the measured rate. The error associated to each point was evaluated calculating the correction factor a hundred times through the same algorithm, sampling a Gaussian with mean equal to the measured rate and width equal to the error associated to the measurement (Poisson).
There is a discrepancy between the "real" value and the corrected one for rates higher than 10^6 particles/s. Considering a symmetric gaussian beam with a 20 mm σ, the fraction of particles passing through the central fibers is $\sim$ 0.5 % each. This means that using this correction algorithm will provide good estimation of the "real" rate up to beam rates on the order of a few 10^8 particles/s. This algorithm is quite simple, and there are routines more precise than this one, but for the aim of this work this is enough. Actually in the next sections beam rates

higher than 10^7 particles/s will not be simulated, which means that the rate estimation will be good without using the algorithm above.

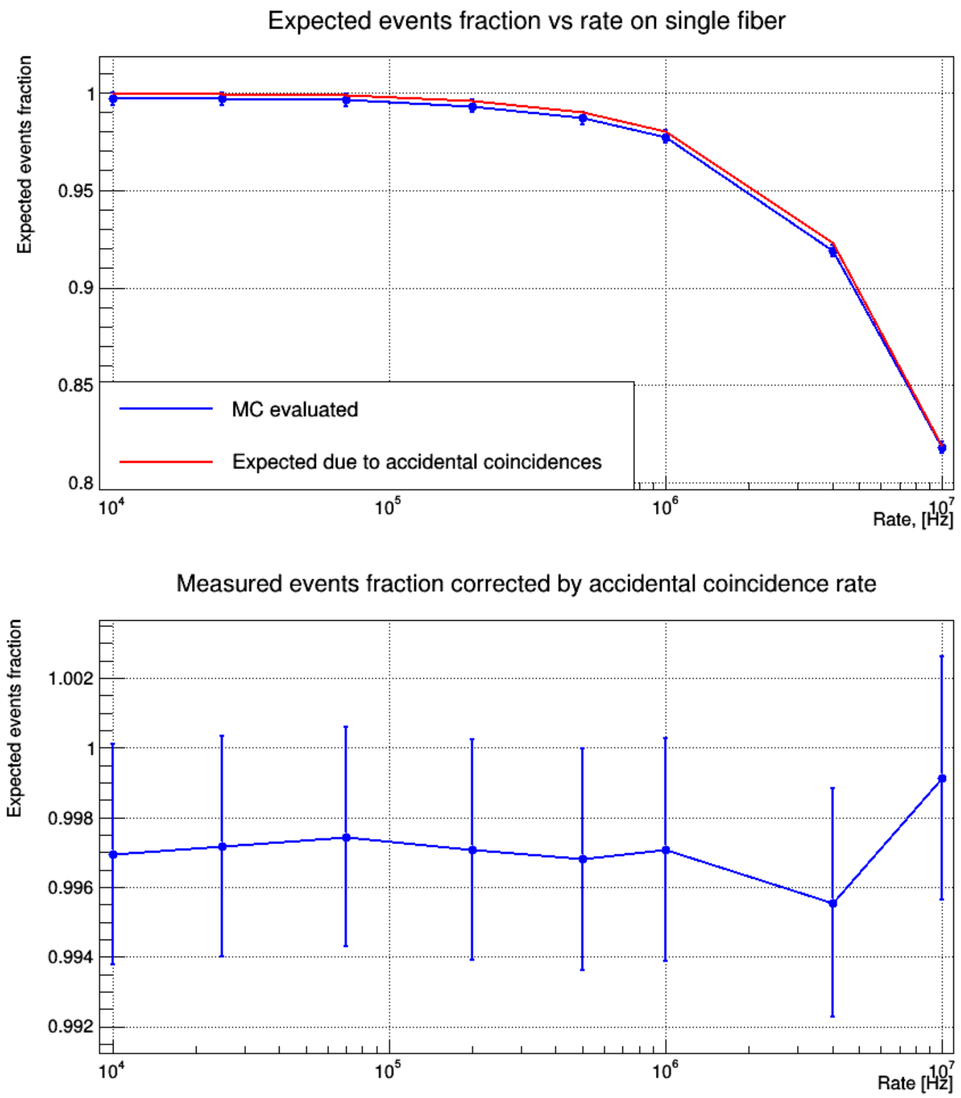

Figure 3.23: *Comparison between expected and simulated dependence of the single fiber rate on the real beam rate. In the top panel there is the dependence of the measured rate fraction on the real one as extracted from MC simulations in blue, to be compared with the red plot that is the expectation evaluated with eq. 3.11. In the bottom panel there is the ratio between the point of the plots above.*

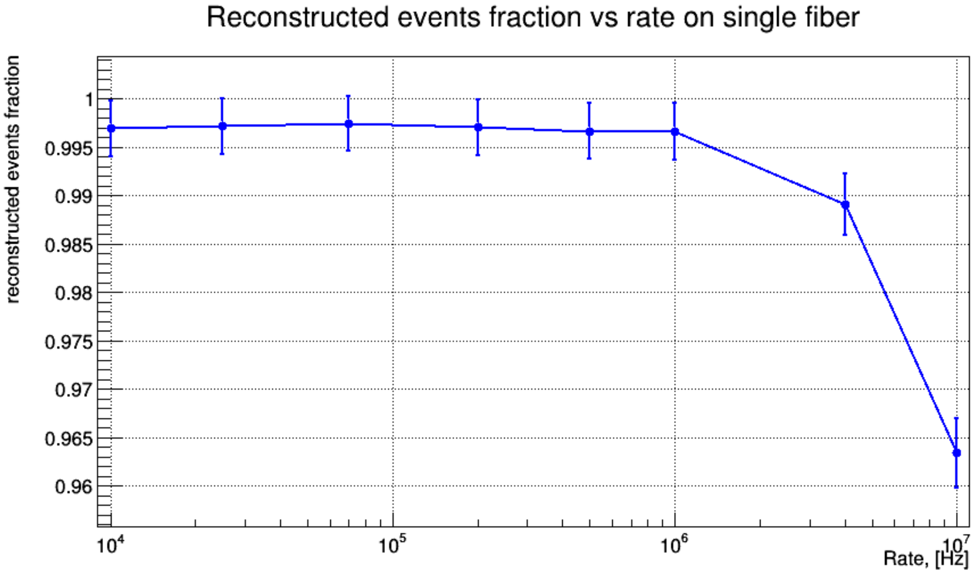

Figure 3.24: *Single fiber rate measured corrected.*

3.5 Complete detector

To simulate the complete detector 42 20 cm long fibers have been placed, using alternatively BCF-10 or BCF-12, 0.25 mm, or 0.50 mm , wide composing a grid: the fibers labelled from 0 to 20 compose the back layer, where the fibers are positioned along the x axis, the horizontal direction, giving information about the vertical component of the beam; the fibers labelled from 21 to 41 compose the front layer, where the fibers are positioned along the y axis, the vertical direction, giving information about the horizontal component of the beam. The fibers are 5 mm spaced and the two layers are 5 mm spaced too. Fig. 3.25 shows the simulated SciFi detector while muon hits a fiber.

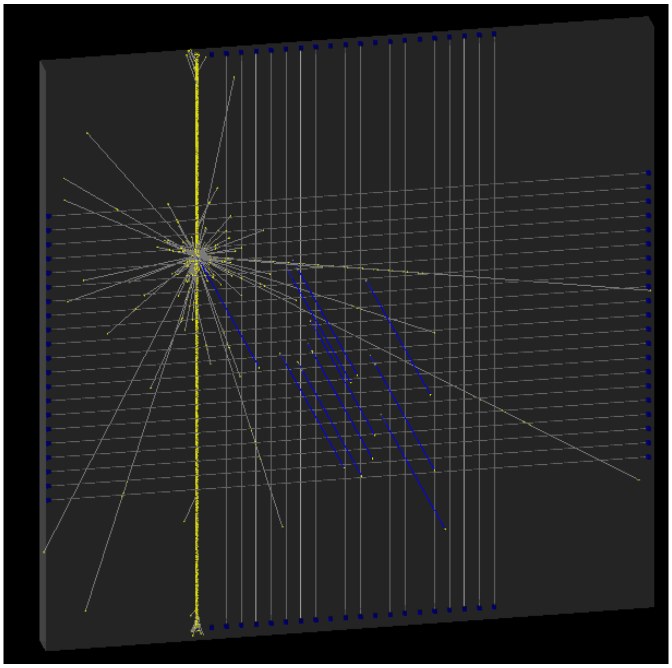

Figure 3.25: *Complete SciFi detector simulation view. The event shown is a muon depositing energy in a front layer.*

At the ends of each fiber a S13360-50CS SiPM is placed, directly in contact with the fiber. The original project involved the use of BCF-10 fibers 0.25 mm wide. Currently the fibers used at PSI are BCF-12 and there are two detector versions: an in-air version that uses 0.25 mm wide fibers and an in-vacuum version that uses 0.50 mm wide fibers. In the next paragraph a difference in terms of signal amplitude spectrum will be shown, but at this level it is not possible to prefer a configuration to another: the scintillation properties are similar between BCF-10 and BCF-12, the attenuation lengths is negligible at this lengths (20 cm) and the difference in emission decay time is negligible as well.

More in detail, in this section it will be discussed:

- the performances of the detector while using coincidences between the SiPMs on the same fibers;
- the reconstruction algorithm;
- the information that can be obtained on the correlation between the transverse axes, using the coincidences between the two layers of fibers.

3.5.1 Spectra

In order to compare different configurations of SciFi, simulations have been run varying the beam type and the fibers characteristics. Tab. 3.7 collects the conditions used for these simulations, while Fig. 3.26 and 3.27 show the amplitude spectra after imposing coincidence between SiPMs at the ends of the same fiber. Here and in the simulations of the next paragraphs, the dead time is set to be 20 ns and the coincidence window is 20 ns long, starting from the first SiPM with the output over threshold. The threshold for the coincidences is 1.5 a.u. (photoelectrons): this is to avoid coincidences due to afterpulses or dark noise.

Beam characteristics		
Particle	Initial kinetic energy (momentum) [MeV]	Beam width [mm]
e^+	52.8	20
μ^+	3.7 (28)	20
π^-	16.8 (70.5)	8

Fibers material		Fibers width	
BCF-10	BCF-12	0.25 mm	0.50 mm

Table 3.7: Configurations considered in SciFi simulations. The results are collected in Fig. 3.26 and 3.27.

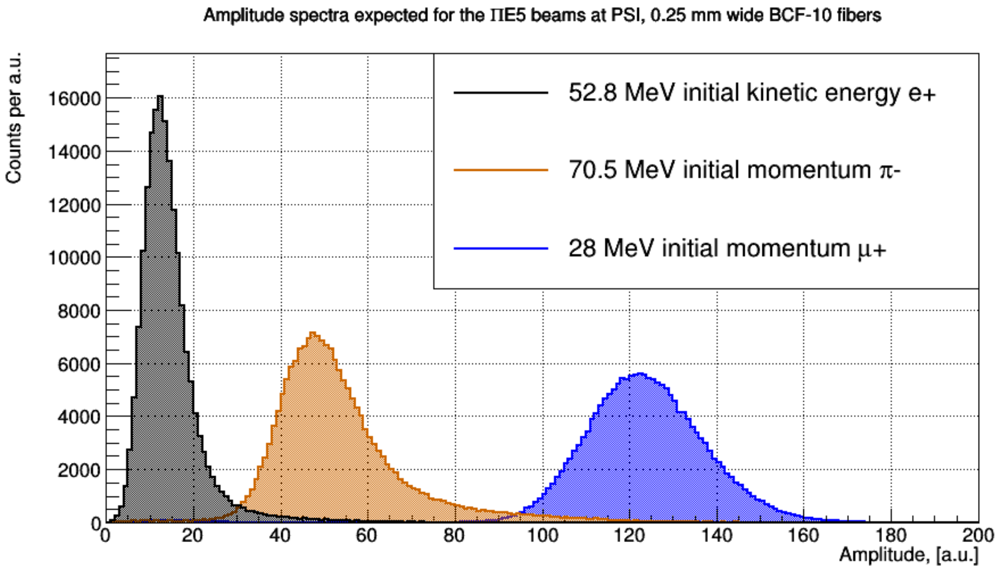

(a) 0.25 mm wide

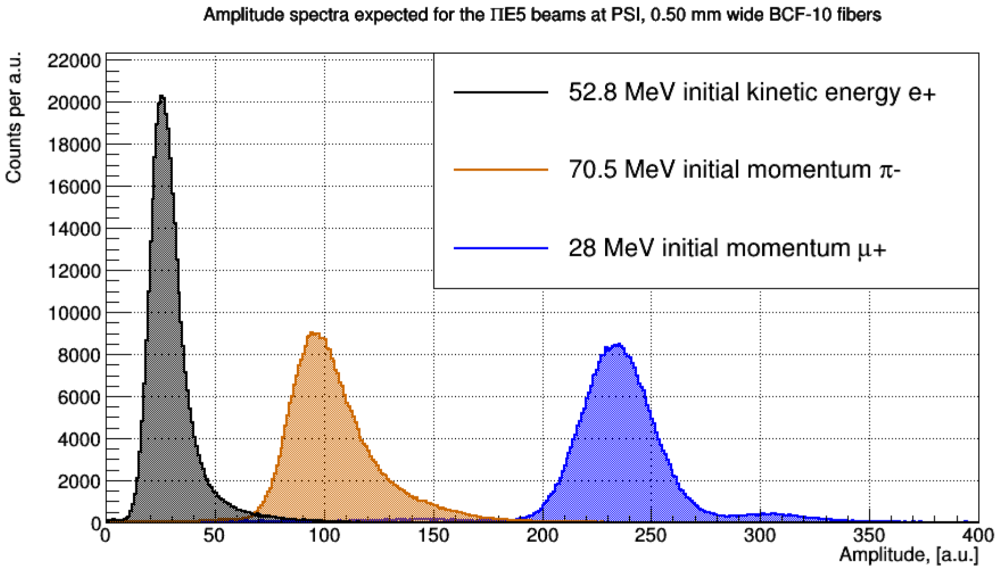

(b) 0.50 mm wide

Figure 3.26: *Amplitude spectra obtained with BCF-10 fibers.*

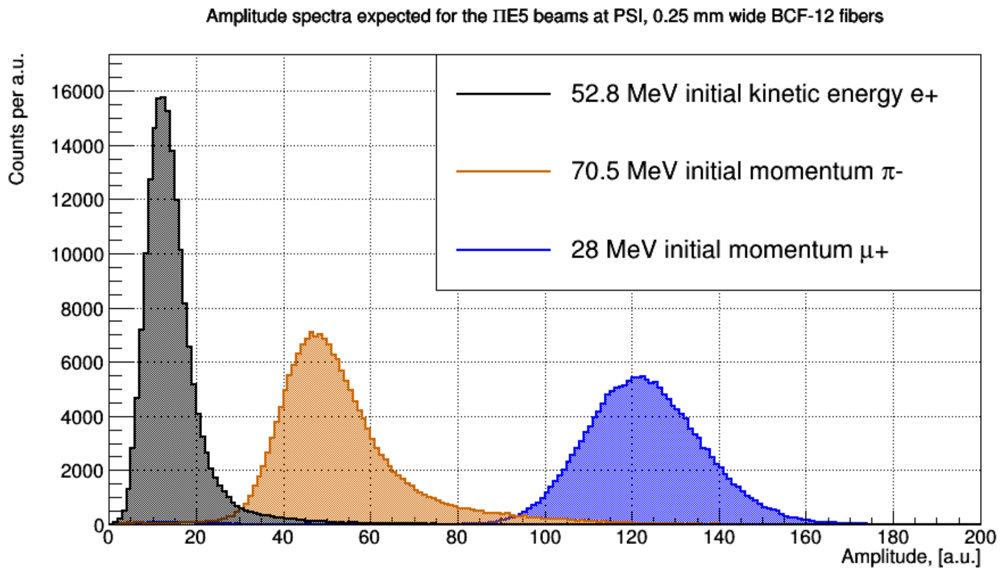

(a) 0.25 mm wide

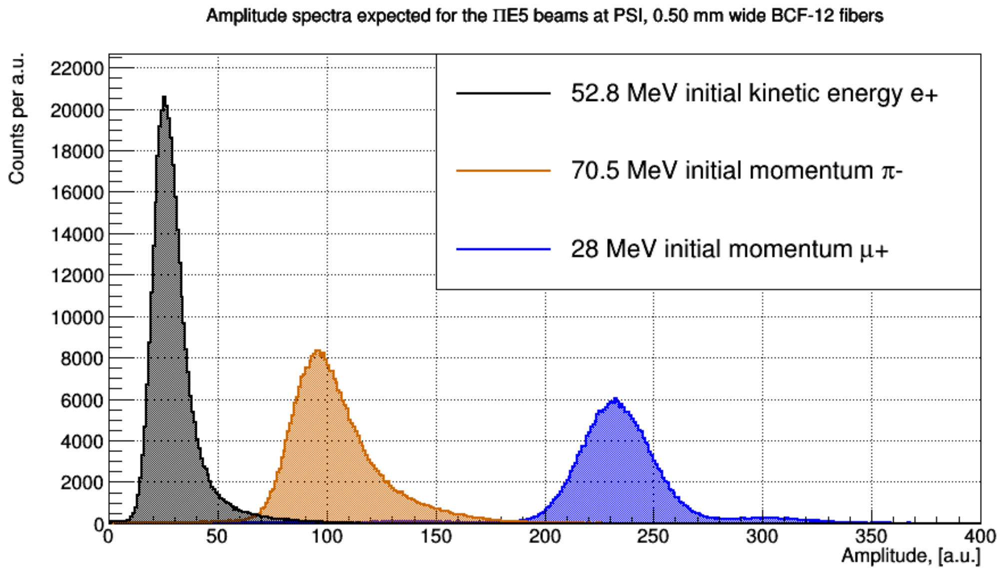

(b) 0.50 mm wide

Figure 3.27: *Amplitude spectra obtained with BCF-12 fibers.*

The most probable values of the three particle distributions are spaced as expected: a factor $\sim$3-4 between e$^+$ and π^-; a factor $\sim$ 10 between e$^+$ and μ^+ (see Fig. 3.6).
As mentioned above, the spectra obtained with BCF-10 and BCF-12 are quite similar and in the following paragraph It will be shown that at a reconstruction level they are equivalent.

Comparing the spectra obtained with an 0.25 mm or 0.50 mm wide fiber, there is a clear difference in the muon spectrum: there is a peak around 300 a.u. in the case of 0.50 mm fibers. This is due to the particles that hit two fibers during a single event: in the second fiber the energy deposit is higher because in the Bethe-Bloch plot, the 28 MeV/c momentum muons are positioned on the left of the minimum. With 0.25 mm fibers this effect is present too, but it is enhanced using 0.50 mm fibers, where the energy deposit difference is higher and number of particles passing through two fibers is higher as well.

Fig. 3.28 shows a comparison between the amplitude spectra of 28 MeV/c momentum muons passing through two fibers when their width is 0.25 or 0.5 mm. The fibers are BCF-10. This effect is completely negligible for pions and positrons.

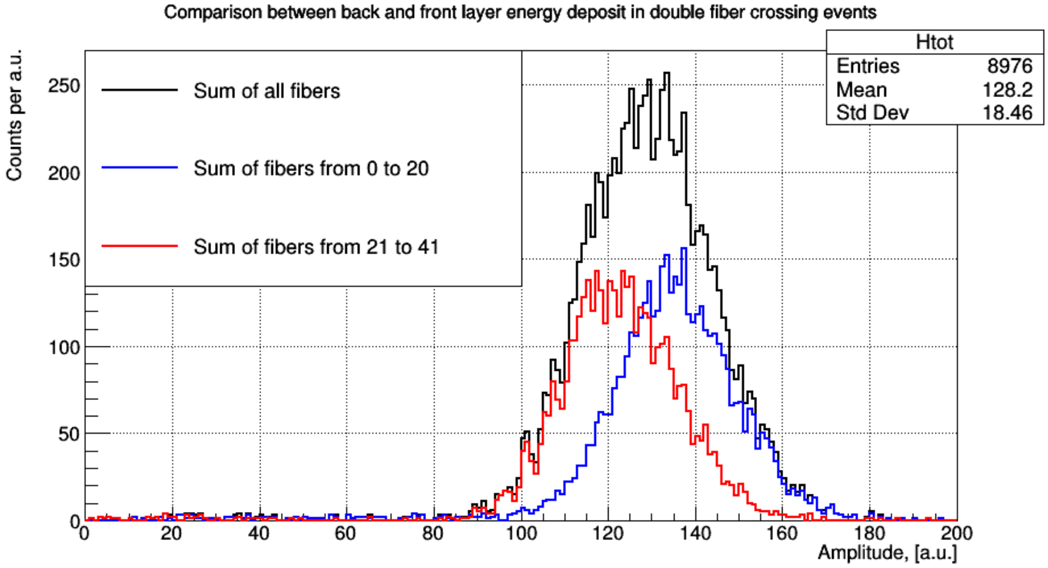

(a) 0.25 mm wide

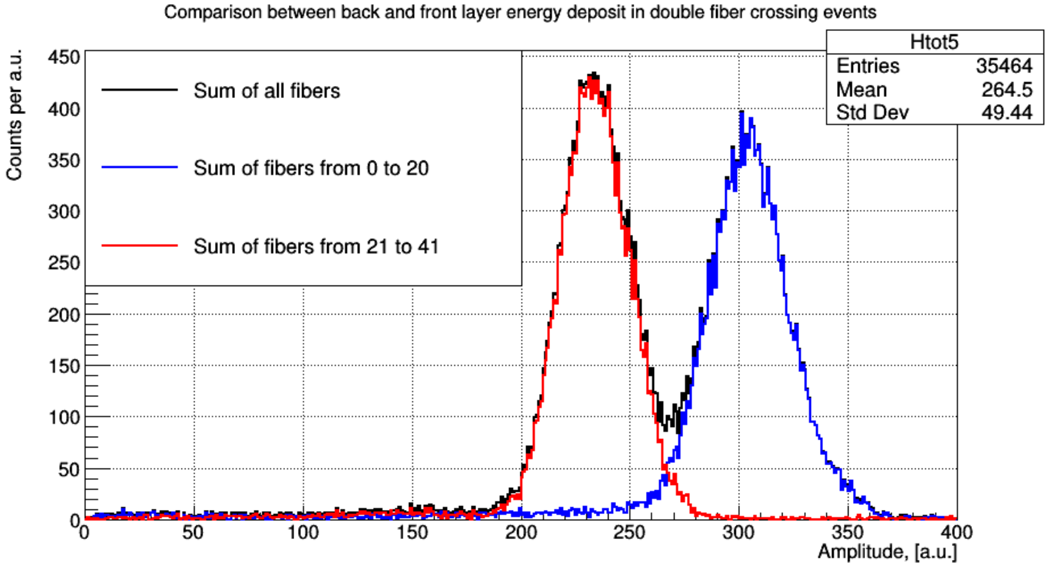

(b) 0.50 mm wide

Figure 3.28: *Amplitude spectra obtained with BCF-10 fibers. Here are shown only events where 28 MeV/c momentum muons pass through two fibers. It is possible to see that the signals from the back layer (fibers 0 to 20) are higher.*

3.5.2 Double channel coincidences

Reconstruction algorithm

The macro that elaborates the response of the detector produces three output files: a ROOT[8], and two text file. The ROOT file collects all the information about the waveforms, while the first text file collects the number of time the SiPMs at the ends of each fibers are in coincidence (42 entries) and the second text file collects the number of time two fibers are in coincidence (441 entries). The text files contain the duration of the run too.

In order to extrapolate information about the shape and the rate of the beam, a macro reads the text file and produces two profiles: a vertical profile, based on the first 21 fibers (back layer); an horizontal profile, based on the last 21 fibers (front layer). Then the two profiles are fitted to two Gaussians that share the same integral: the fit is performed contemporary on the two layers, imposing that the areas of the two Gaussians are the same. From this fit it is not possible to obtain information about correlation between the two transverse directions of the beam. The fitting functions are:

$$f_i(x) = \frac{A}{\sqrt{2\pi}\sigma_i} \exp\left(- \frac{(x_i - \mu_i)^2}{2\sigma_i^2} \right) \tag{3.12}$$

with A the integral of the two fitting functions, i = 0 or 1 represents the layer, σ_i the standard deviation and μ_i the mean of the i-th direction. The fit is performed minimizing numerically the sum of the χ^2-like variable:

$$\chi^2 = \Sigma_{i=0,1}\Sigma_{j=0}^{20} \frac{(O_{i,j} - f_i(x_{i,j}, \mu_i, \sigma_i))^2}{O_{i,j}} \tag{3.13}$$

where j is an index for fibers on the same layer, $O_{i,j}$ represents the number of hits on the j-th fiber in the layer i and $x_{i,j}$ is the position of the j-th fiber along the i-th direction.
The rate is obtained through the following expression:

$$R = \frac{A}{fiber\,core\,width \times \Delta T} \tag{3.14}$$

where ΔT is the duration of the simulation run.

Tab. 3.8 and Fig. 3.29 show the reconstruction performed on a 28 MeV/c momentum μ^+ beam, perfectly centered along the axis of the detector and symmetric, with a 20 mm sigma. The amplitude threshold is 1.5 a.u. (photo-electron) and the fibers are BCF-10.

Tab. 3.9 and Fig. 3.30 show the reconstruction performed in the same conditions as above, but using BCF-12 fibers.

μ_x [mm]	σ_x [mm]	μ_y [mm]	σ_y [mm]
0.09 ± 0.09	20.22 ±0.06	0.01 ± 0.03	20.09 ± 0.06

A [mm]	R [μ/s]	χ^2	ndof
(2.305 ± 0.008) 10^5	(9.80 ± 0.03) 10^6	34.8	37

Table 3.8: Fit parameters and rate for beam reconstruction example in Fig. 3.29.

μ_x [mm]	σ_x [mm]	μ_y [mm]	σ_y [mm]
-0.11 ± 0.02	20.06 ± 0.06	-0.05 ± 0.10	20.12 ± 0.06

A [mm]	R [μ/s]	χ^2	ndof
(2.223 ± 0.008) 10^5	(9.81 ± 0.03) 10^6	45.2	37

Table 3.9: Fit parameters and rate for beam reconstruction example in Fig. 3.30.

The results are compatible and the resolutions too. At this level is not possible to distinguish the performances of SciFi using BCF-10 fibers or BCF-12. In terms of shape reconstruction, the results obtained with positrons and pions are consistent as well.

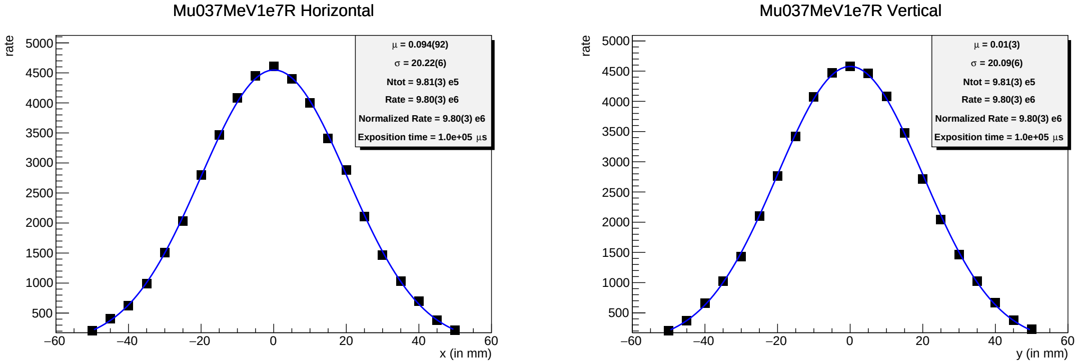

(a) Front layer

(b) Back layer

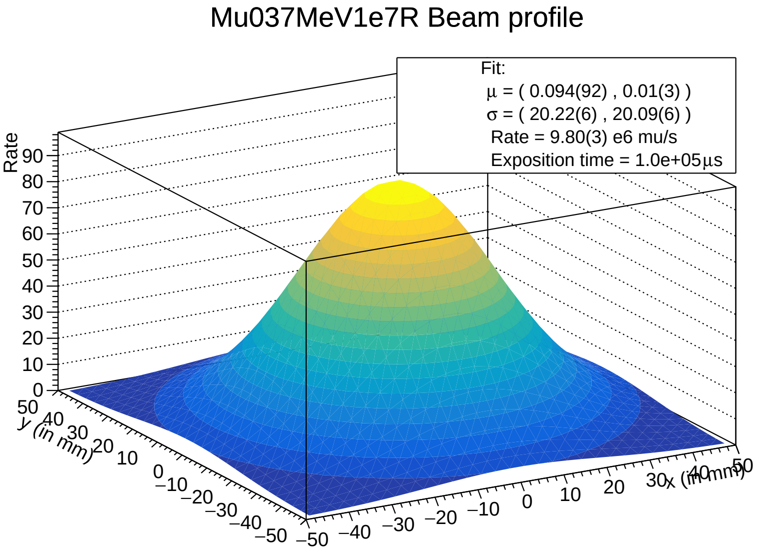

(c) Bidimensional view

Figure 3.29: *Muon beam reconstruction with SciFi. The beam is 20 mm wide in both directions, centered along the detector axis. The fibers are BCF-10, 0.25 mm wide. The beam rate is* 10^7 *μ/s. The number of events generated is* 10^6.

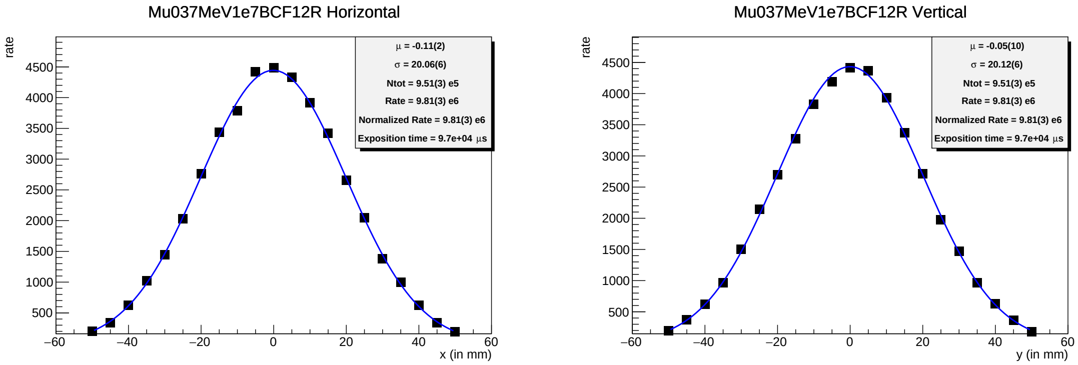

(a) Front layer

(b) Back layer

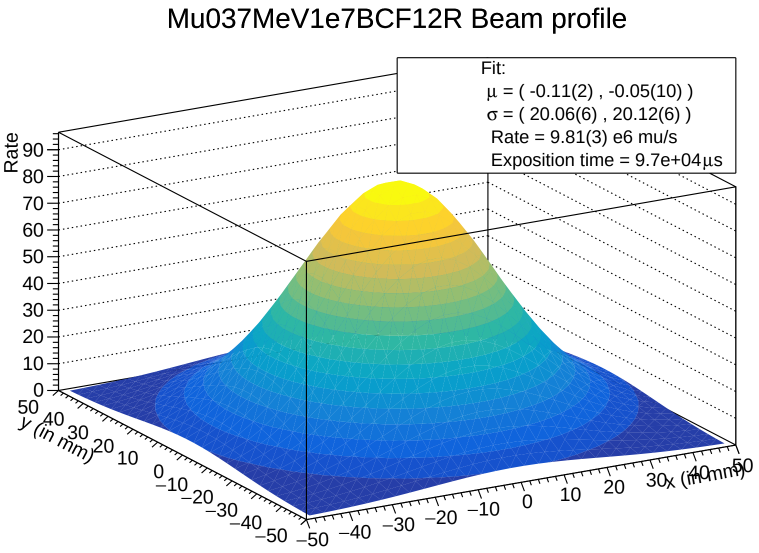

(c) Bidimensional view

Figure 3.30: *Muon beam reconstruction with SciFi. The beam is 20 mm wide in both directions, centered along the detector axis. The fibers are BCF-12, 0.25 mm wide. The beam rate is* 10^7 μ*/s. The number of events generated is* 10^6.

Beam rate reconstruction

In order to check if the rate resolution as extracted from the fit is a good estimation, or to point out if there is some resolution limitation at this level, 10 runs have been simulated using a 28 MeV/c momentum muon beam. The beam is 20 mm wide, symmetric, perfectly aligned along the detector axis. The beam rate is 10^7 μ/s and the number of events simulated per run is 10^6. After the simulation the beam is reconstructed and a comparison is made among the beam rates obtained from each sample. Then the arithmetic mean of the obtained values and the beam rate extrapolated from the reconstruction when performed on the merging of the samples, are compared. This procedure is done for 0.25 and 0.50 mm wide fibers, using BCF-10 and BCF-12 as materials.

Fig. 3.31 shows the results of these simulations, while Fig. 3.32 shows an example of merged sample: it is the reconstruction performed on the sample obtained by merging the 0.25 mm wide BCF-10 fibers samples.

Tab. 3.10 collects a summary of the reconstructed rates extrapolated by arithmetic mean calculation or fit on the merged samples.

Sample conditions	Arithmetic mean of rates [μ/s]	χ^2/ndof	Rate extrapolated from the merged samples [μ/s]
BCF-10, 0.25 mm wide	$(9.811 \pm 0.010)\ 10^6$	7.4/9	$(9.815 \pm 0.010)\ 10^6$
BCF-10, 0.50 mm wide	$(9.867 \pm 0.008)\ 10^6$	6.4/9	$(9.869 \pm 0.008)\ 10^6$
BCF-12, 0.25 mm wide	$(9.806 \pm 0.013)\ 10^6$	2.7/9	$(9.813 \pm 0.013)\ 10^6$
BCF-12, 0.50 mm wide	$(9.837 \pm 0.009)\ 10^6$	15.9/9	$(9.840 \pm 0.009)\ 10^6$

Table 3.10: Comparison between arithmetic mean of beam rate reconstructed from low statistics samples, 10^6 events, and beam rate reconstructed from high statistics samples, 10^7 events.

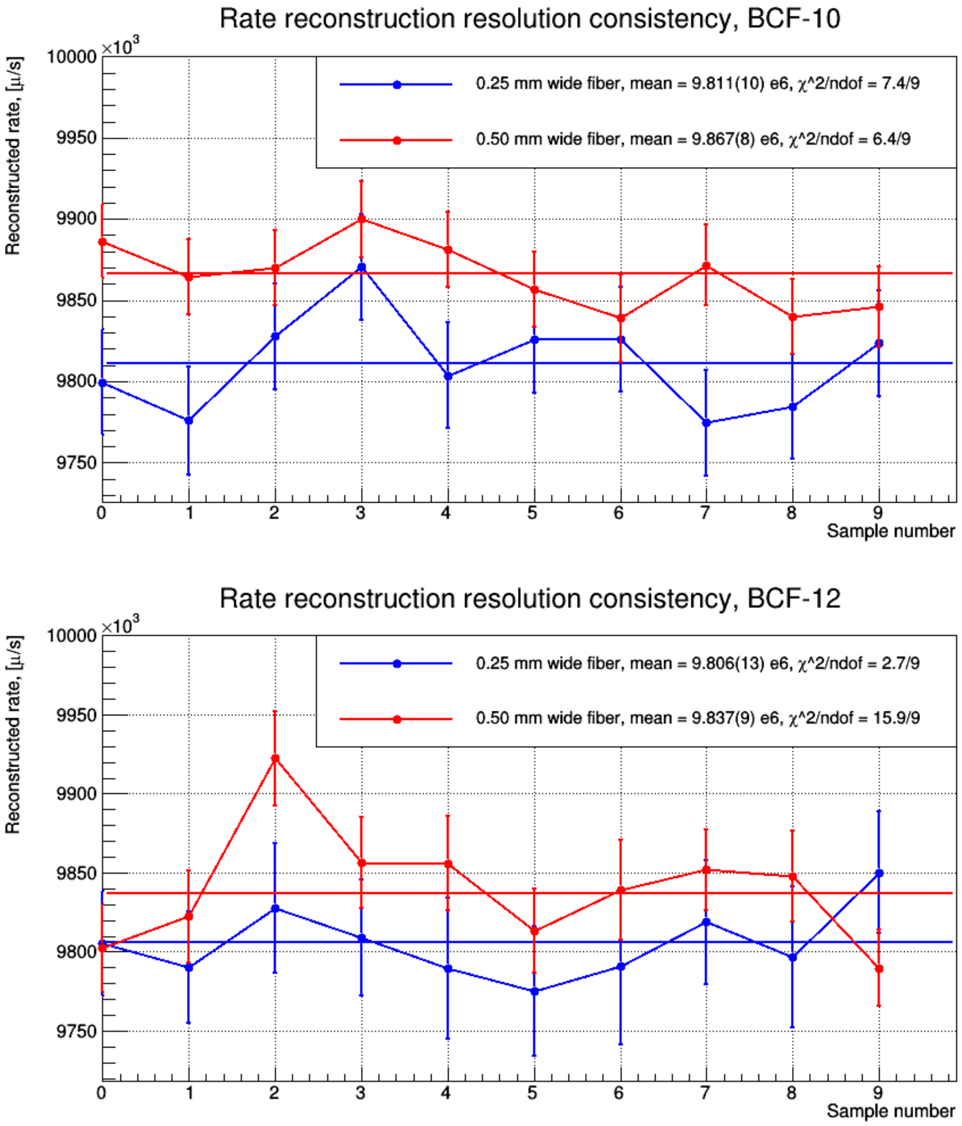

Figure 3.31: *Comparison between rate reconstruction in different configuration. Each graph represents the rate reconstruction for a different sample, maintaining fixed the detector configurations. In the top panel there are the graphs related to BCF-10 fibers. In the bottom panel there are the graphs related to BCF-12 fibers. Each sample is composed of* 10^6 *events and the beam rate is always* 10^7 μ*/s.*

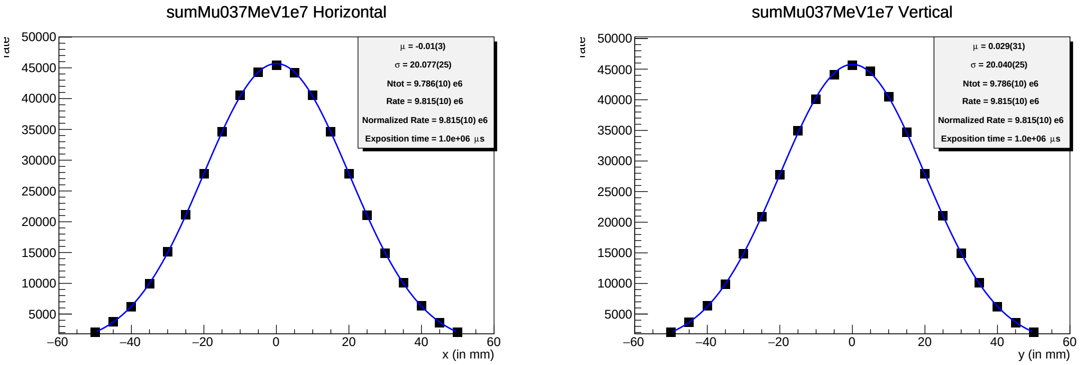

(a) Front layer

(b) Back layer

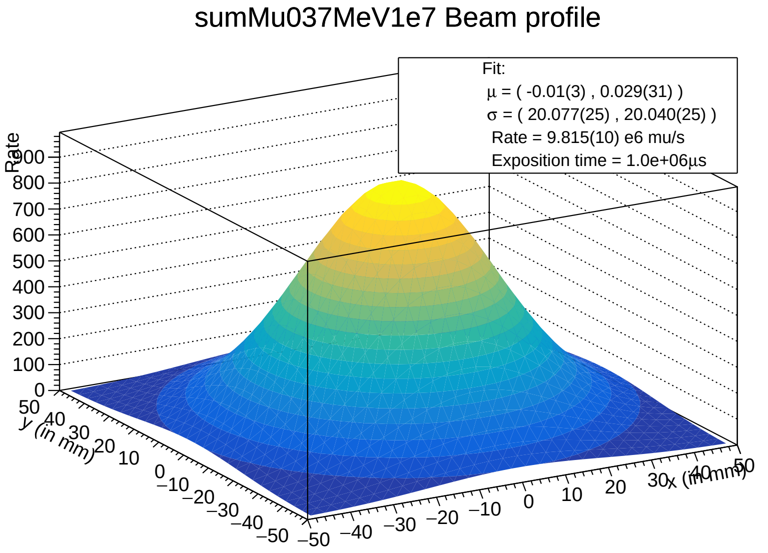

(c) Bidimensional view

Figure 3.32: *Muon beam reconstruction with SciFi. The beam is 20 mm wide in both directions, centered along the detector axis. The fibers are BCF-10, 0.25 mm wide. The beam rate is 10^7 μ/s. The number of events generated is 10^7.*

The results are consistent on equal conditions. It must be underlined that on a theoretic level 10^6 events are enough to provide a resolution better than per cent. Anyway the results are not compatible among the different conditions considered and they are never consistent with the real value. Tab. 3.11 collects the beam rate extracted with a 20 mm positron beam and with an 8 mm pion beam, using 0.25 mm wide BCF-10 fibers. The results are not consistent with the values obtained with the muon beams, nor between them. This suggests that there is a difference in performances when measuring beam rates, depending on the primary particle characteristics. In the future it will be needed a data-driven check on the results obtained through the Monte Carlo simulation, and on the beam rate measurement stability and dependence on the beam specifications.

	e^+ beam	π^- beam
Kinetic energy (momentum) [Mev(Mev/c)]	52.8	16.8 (70.5)
Beam width [mm]	20	8
Reconstructed beam rate [particle/s]	$(9.77 \pm 0.03)\ 10^6$	$(9.62 \pm 0.03)\ 10^6$

Table 3.11: Beam rate reconstruction performed on e^+ and π^- beams. Here the characteristics of the beam and the resulting rate reconstruction.

3.5.3 Double fiber coincidences

As already mentioned, the output files produced at the end of the simulation are three: a ROOT file containing information about the single waveforms; a text file with the counts of the coincidences between SiPMs on the same fiber; a text file that contains the counts of the coincidences between two fibers. The first two outputs have already been discussed. In this paragraph a brief discussion will be done about the reconstruction algorithm implemented to extrapolate information about the correlation between the two transverse directions: in fact the information about rate, sigmas and position of the beam will always be more precise if obtained through the single layer reconstruction presented in the previous paragraph, but it is not possible to obtain information about the correlation of the beam from such an analysis.

Reconstruction algorithm

When the output waveforms coming from SiPMs on the same fiber pass over threshold in a time window 20 ns long, the amplitude of the two signals, the time at which the coincidence is activated (*activation time*) and the corresponding fiber are saved in a TTree[8] named *swaves* (”signal waveforms”), which then is written inside the ROOT output file of the simulation. In order to generate coincidences between the two layers of fibers, a routine reads the *swaves* TTree. This TTree is ordered by the *activation time* variable.
When two consecutive entries in *swaves* are activated in a time window 12.5 ns long (which is the actual minimum time window that can be obtained by the WDB system), if the corresponding fibers belong to different layers, the amplitudes, the activation time and an integer from 0 to 440, indicating the involved fibers, are saved in a TTree named *swaves2.* After an event there is a 25 ns long dead time window. Then the text file regarding the coincidences between fibers is generated.

Unlike the single fiber case, here there is a major background to be considered: the accidental coincidences. In fact, in order to obtain a bidimensional profile of the beam, it is necessary to let all the fibers in a layer to be in coincidence with all the fibers in the other layer. This means that the expected profile is the sum of two bidimensional Gaussians: one is the ”real” one, directly related to the beam shape and containing information about the correlation; one is an uncorrelated beam, with the same widths of the real beam and a rate that is strictly related to the number of accidental coincidences between fibers in the two layers.
The rate of accidental coincidences between the two layers is:

$$R_{acc} = 2R_{layer} \exp\big(- R_{layer} \times \Delta T_{coincidence}\big) \tag{3.15}$$

where R_{layer} is the number of events registered per layer in the unit time and $\Delta T_{coincidence}$ is the length of the coincidence time window (12.5 ns). In first approximation, R_{layer} can be obtained by dividing the total number of counts measured with SciFi by the length of the measurement window and by a factor 2. This is not the beam rate as it would be extracted by a bidimensional gaussian fit: this is the rate at which there is an accidental coincidence between two fibers of different layers.

In order to obtain the ”uncorrelated beam rate” R_{un}, it is necessary to divide R_{acc} by the integral of the uncorrelated Gaussian, when normalized to one, in the ”intersections” between the fibers. In first approximation, the area of these intersections is the square of the core of the fibers. This integral is performed by the reconstruction algorithm after that the single layer reconstruction is finished, so that the beam position and the sigmas are already available.

A bidimensional Gaussian can be expressed in the following form:

$$f(x,y) = \frac{A}{\pi\sigma_x\sigma_y\sqrt{1-\rho^2}} e^{-\frac{1}{2(1-\rho^2)}\left(\frac{(x-\mu_x)^2}{\sigma_x^2} - \frac{2\rho(x-\mu_x)(y-\mu_y)}{\sigma_x\sigma_y} + \frac{(y-\mu_y)^2}{\sigma_y^2}\right)} \tag{3.16}$$

where μ_i is the mean value along the i direction, σ_i is the standard deviation along the i direction, ρ is the correlation between the two directions and A is the normalization factor.

The fitting function F that has been used is the sum of two Gaussians as reported in eq. 3.16: f_{corr} and f_{un}. In order to make the fit converge without ambiguity, it is performed fixing some parameters that are known from the single layer analysis. Tab. 3.12 collects the values of the fixed parameters and the initial values of the free parameters.

f_{corr} parameters					
A_{corr} (free)	$\mu_{x,corr}$ (fixed)	$\sigma_{x,corr}$ (free)	$\mu_{y,corr}$ (fixed)	$\sigma_{y,corr}$ (free)	ρ_{corr} (free)
$A_{single} \times$ $f.c.w.$	$\mu_{x,single}$	$\sigma_{x,single}$	$\mu_{y,single}$	$\sigma_{y,single}$	0

f_{un} parameters					
A_{un} (fixed)	$\mu_{x,un}$ (fixed)	$\sigma_{x,un}$ (fixed)	$\mu_{y,corr}$ (fixed)	$\sigma_{y,corr}$ (fixed)	ρ_{un} (fixed)
$R_{un} \times$ $f.c.w.^2 \times$ ΔT	$\mu_{x,single}$	$\sigma_{x,single}$	$\mu_{y,single}$	$\sigma_{y,single}$	0

Table 3.12: Initial parameters for bidimensional beam reconstruction with SciFi. The parameter named *f.c.w.* is the fiber core width. ΔT is the time window of the measurement.

The parameters labelled with *single* are obtained from the single layer reconstruction. The parameter named *f.c.w.* is the fiber core width. If $|\rho_{corr}| > 2\Delta\rho_{corr}$ the A_{un} parameter is set free and the fit is repeated. In order to avoid misevaluations while reconstructing low correlations, A_{un} is limited upperly by the value in Tab. 3.12.

Fig. 3.33 shows an example of beam reconstruction using the algorithm above. The beam is obtained rotating 60 degrees a beam with the parameters in Tab. 3.13. The expected correlation is ρ = 0.672 and the expected σ are σ_x = 15.207 and σ_y = 22.221. The fibers are BCF-10 0.25 mm wide and the number of events generated is 10^7. The results are collected in Tab. 3.14.

The reconstructed beam rate from single layer fit is:

$$R = (9.816 \pm 0.010)10^6 \mu/s$$

The reconstructed beam rate from bidimensional fit is:

$$R_{corr} = (9.729 \pm 0.007)10^6 \mu/s$$

In order to evaluate properly the uncertainty on ρ, a macro iterates the estimation sampling the fixed parameters used in the fit: in fact those parameters are obtained from a previous fit and so they have an uncertainty and are correlated one each other. At each iteration five uncorrelated Gaussians are sampled, one for each parameter of the single layer fit, with the variance obtained through the fit. Then they are mixed using the Cholesky decomposition of the correlation matrix of the single layer fit.

The values obtained in this way are then used to obtain a distribution of ρ. The uncertainty evaluated this way is negligible with respect to the one extrapolated with the fit.

Fig. 3.34 shows the correlation distribution described above. The standard deviation is 3.1 10^{-5}, while the reconstructed value of the correlation is:

$$\rho_{corr} = 0.673 \pm 0.007 \tag{3.17}$$

The uncertainty is two order of magnitude higher than the standard deviation on ρ_{corr}: the fit is stable on the estimation of the correlation. The next paragraph will focus on the reconstruction of ρ_{corr} in different conditions.

Beam rate [μ/s]	μ_x [mm]	σ_x [mm]	μ_y [mm]	σ_y [mm]	ρ
10^7	0	25	0	10	0

Table 3.13: Beam parameters of the reconstruction example in Fig. 3.33 before rotation.

f_{corr} parameters					
A_{corr} (free) [mm^2]	$\mu_{x,corr}$ (fixed) [mm]	$\sigma_{x,corr}$ (free) [mm]	$\mu_{y,corr}$ (fixed) [mm]	$\sigma_{y,corr}$ (free) [mm]	ρ_{corr} (free)
(5.13 ± 0.04) 10^5	-0.04 ± 0.02	14.94 ± 0.08	0.04 ± 0.04	21.83 ± 0.14	0.673 ± 0.007
f_{un} parameters					
A_{un} (released) [mm^2]	$\mu_{x,un}$ (fixed) [mm]	$\sigma_{x,un}$ (fixed) [mm]	$\mu_{y,corr}$ (fixed) [mm]	$\sigma_{y,corr}$ (fixed) [mm]	ρ_{un} (fixed)
(1.066 ± 0.006) 10 ^{5}	-0.04 ± 0.02	15.214 ± 0.016	0.04 ± 0.04	22.22 ± 0.03	0
χ^2/ndof					
single layer fit			bidimensional fit		
42.4/37			365/377		

Table 3.14: Fit parameters for beam reconstruction in Fig. 3.33. It is performed using coincidences between fibers on different layers.

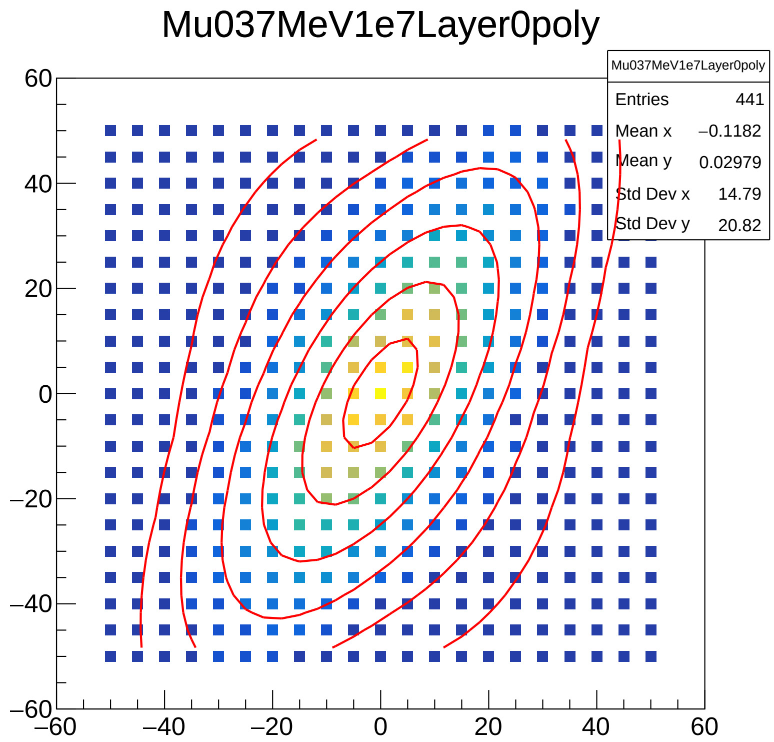

(a) Comparison between fit and histogram.

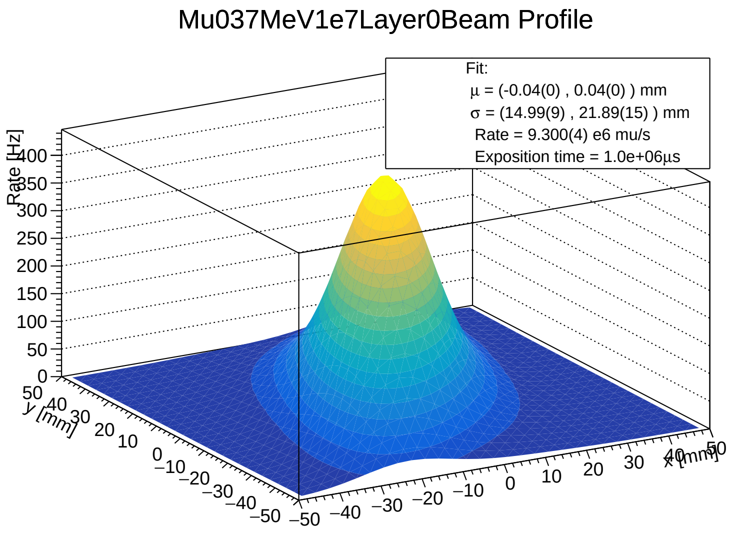

(b) Fitting function profile.

Figure 3.33: *Correlated muon beam reconstruction using coincidences between fibers on different layers. The beam parameters are collected in Tab. 3.13. The results are collected in Tab. 3.14. The number of events generated is* 10^7.

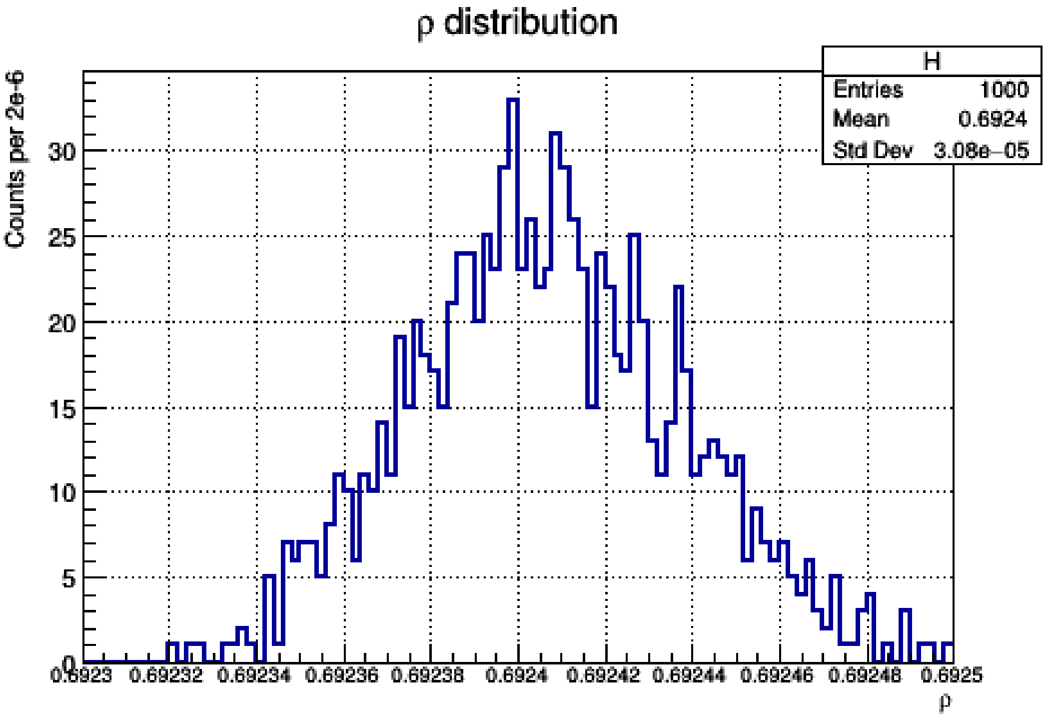

Figure 3.34: *Reconstructed ρ distribution.*

Correlation estimation

Fig. 3.35 and Tab. 3.16 show the results of the reconstruction performed on a beam with lower correlation. Tab. 3.15 shows the expected values. The number of event generated is 10^6.

Beam rate [μ/s]	μ_x [mm]	σ_x [mm]	μ_y [mm]	σ_y [mm]	ρ
10^7	0	16.39	0	18.87	0.245

Table 3.15: Beam parameters of the low correlation reconstruction example in Fig. 3.35 before rotation.

The so-obtained parameters are compatible with the expected values.

f_{corr} parameters					
A_{corr} (free) [mm^2]	$\mu_{x,corr}$ (fixed) [mm]	$\sigma_{x,corr}$ (free) [mm]	$\mu_{y,corr}$ (fixed) [mm]	$\sigma_{y,corr}$ (free) [mm]	ρ_{corr} (free)
(5.13 ± 0.04) 10^5	0.03 ± 0.07	15.9 ± 0.4	-0.04 ± 0.03	17.9 ± 0.4	0.28 ± 0.03

f_{un} parameters					
A_{un} (fixed) [mm^2]	$\mu_{x,un}$ (fixed) [mm]	$\sigma_{x,un}$ (fixed) [mm]	$\mu_{y,corr}$ (fixed) [mm]	$\sigma_{y,corr}$ (fixed) [mm]	ρ_{un} (fixed)
(1.334 ± 0.009) 10^{4}	0.03 ± 0.07	16.482 ± 0.004	-0.04 ± 0.03	19.04 ± 0.07	0
χ^2/ndof					
single layer fit			bidimensional fit		
42.4/37			365/377		

Table 3.16: Fit parameters for beam reconstruction in Fig. 3.35. It is performed using coincidences between fibers on different layers. The $_{un}$ parameter is kept fixed because it reached the upper limits during the minimization.

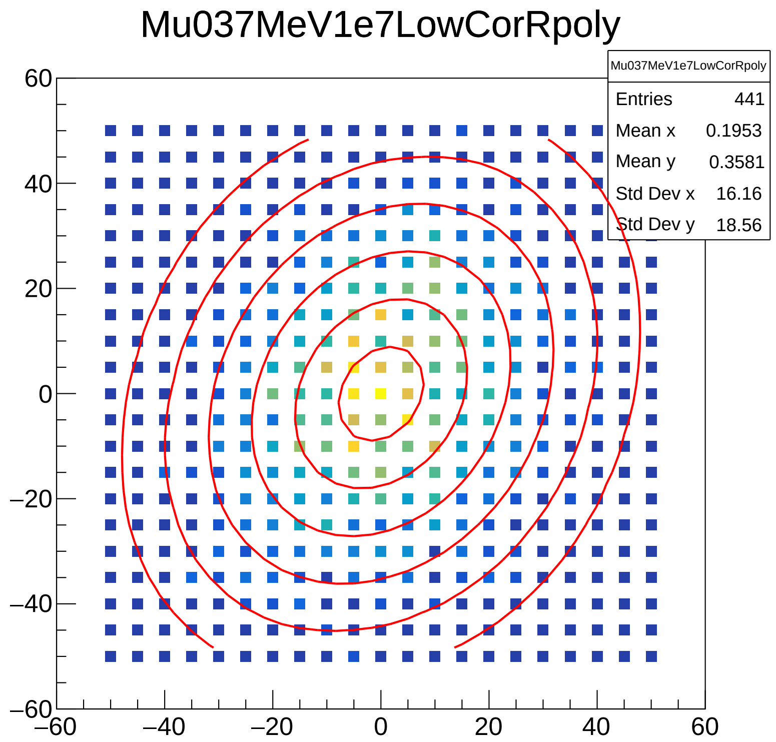

(a) Comparison between fit and histogram.

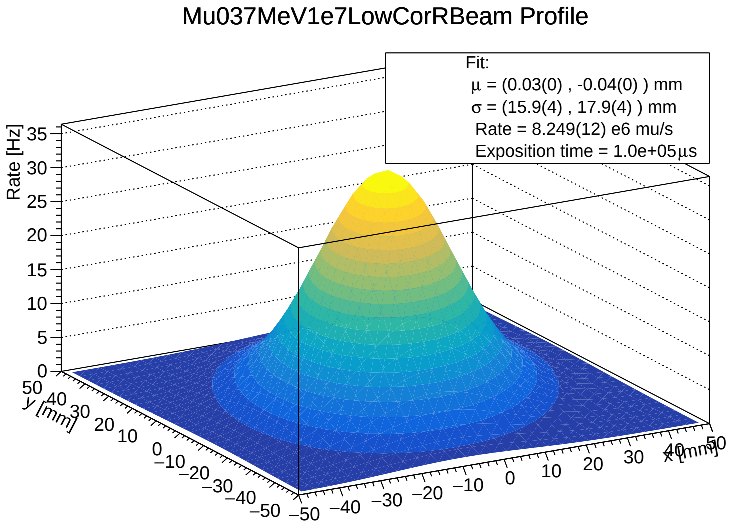

(b) Fitting function profile.

Figure 3.35: *Low correlation muon beam reconstruction using coincidences between fibers on different layers. The beam parameters are collected in Tab. 3.15. The results are collected in Tab. 3.16. The number of events generated is* 10^6.

Then the same simulations are repeated as in previous paragraph (beams specifications in Tab. 3.13), using different values for the rotation angle, generating 10^6 events for each sample. The results are collected in Fig. 3.36. All the values are compatible with the expected one.

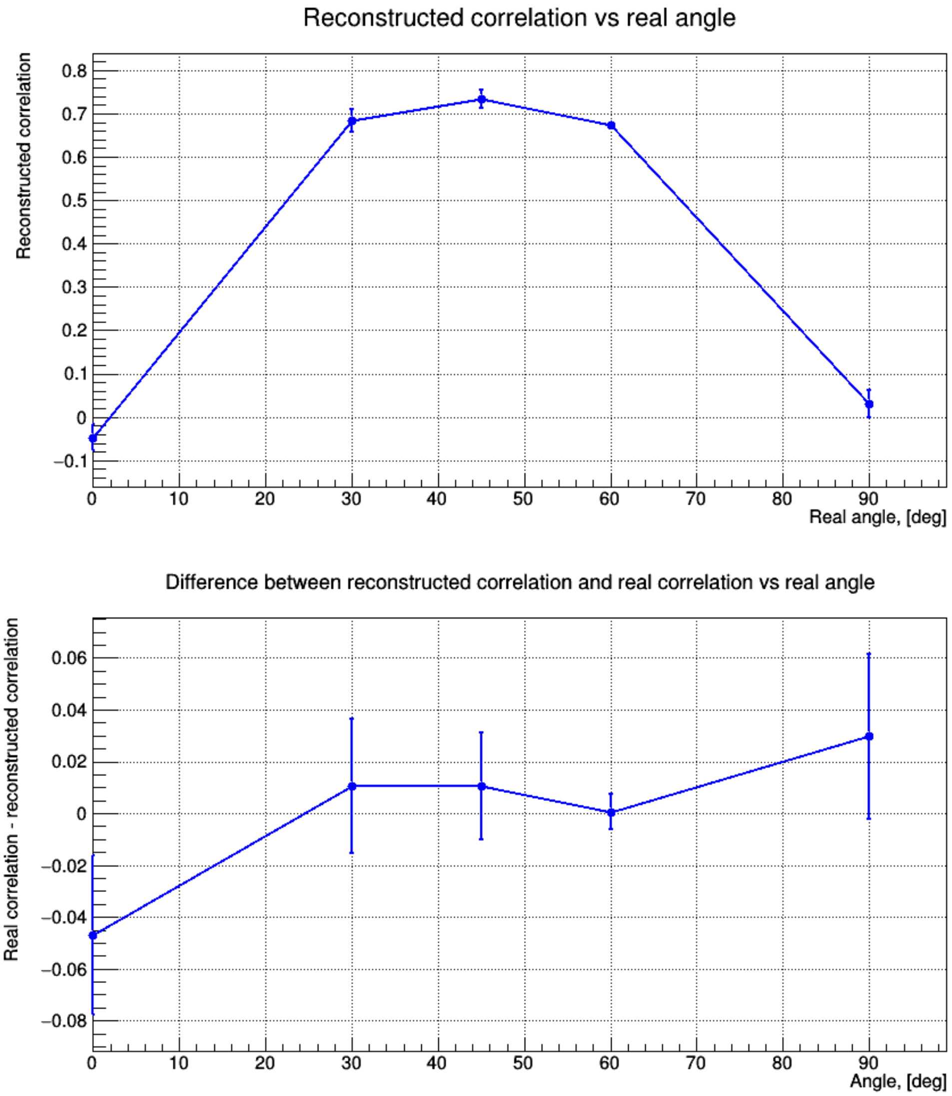

Figure 3.36: *Reconstructed ρ_{corr} dependence on the rotation angle.*

So it would be possible to measure the beam correlation by using coincidences between fibers on different layers. Currently this feature is not implemented in the SciFi trigger.

3.6 First proof of principle

During Summer 2019 I spent two months at PSI laboratories as a summer student. During the summer program I could participate to the first tests of the SciFi detector. Fig. 3.37 shows one of the first measurements performed with the 0.25 mm wide fibers SciFi on the ΠE5 muon beam, while positioned at collimator. The measurement was taken on September the 16^{th}. The threshold was set on the second photo-electron and the measurement lasted 10 s.

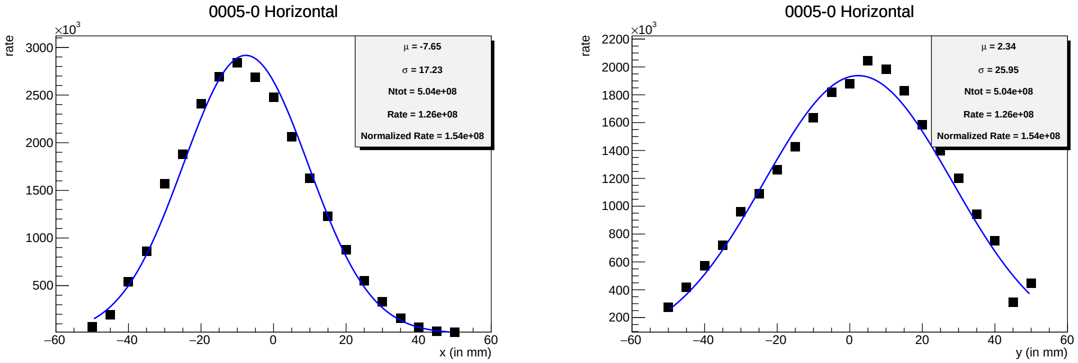

(a) Front layer

(b) Back layer

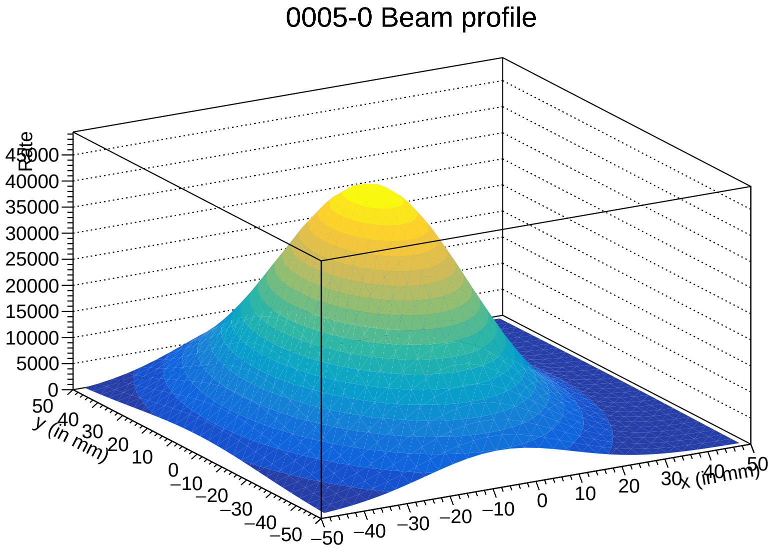

(c) Bidimensional view

Figure 3.37: *Beam measurement performed with 0.25 mm wide fibers SciFi on the ΠE5 muon beam at PSI laboratories. data taken on September 16^{th}, 2019.*

Chapter 4

Diagnostic tools: MatriX

In Ch. 3 I introduced a quasi non-invasive beam monitor. In the next chapter I am going to introduce a destructive beam monitor: MatriX.

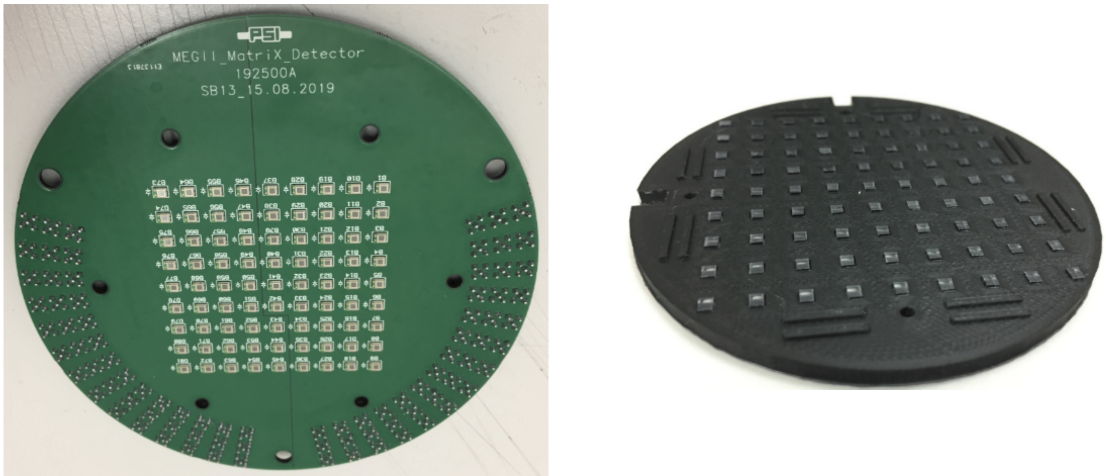

(a) SiPM matrix

(b) The BC-400 scintillating crystals are positioned inside a plastic mask during the assembly of the detector.

Figure 4.1: *MatriX detector view.*

It has the capability to measure beam rates and shapes with high precision as SciFi detector, but the design of this detector suits better the characteristics of the beam at COBRA center (Fig. 4.2), which is narrower than at collimator (μ^+ beam $\sigma_{x,y} \sim 10$ mm), and the available space at the center of the MEGII apparatus[5].

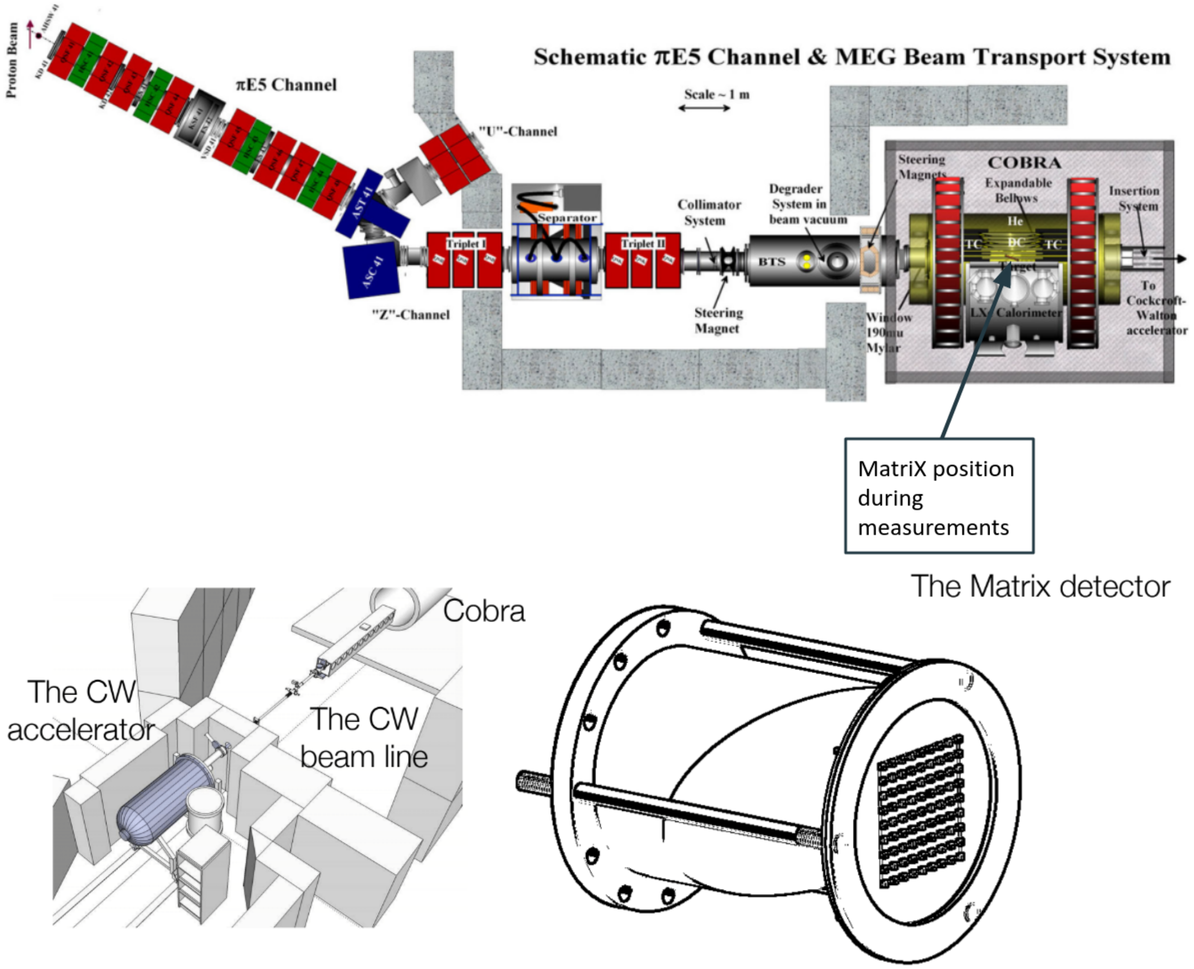

Figure 4.2: *MatriX position along the beam line.*

In the next sections I will describe in detail the MatriX detector and its Monte Carlo simulation implementation with the Geant4 toolkit[21, 22, 23].

4.1 Basic principles: brief introduction

MatriX is a beam monitor detector based on cubic scintillating crystals coupled to SiPMs. As in SciFi the SiPM read the scintillation light emitted after the passage of charged particles, but in this case - at least for the muons - the full energy deposit is exploited. In fact the main difference between SciFi and MatriX is the amount of energy deposited in each element and the more efficient way to collect the scintillation light, which for MatriX is higher, implying high amplitude signals that allow to cut the DN of the SiPM just with a threshold.

Due to the position along the beam line in which MatriX has to be put for the measurements, there is no need to make it a non-invasive detector: SciFi is intended to be used online, to check the beam position and shape, or even the rate, if it is necessary; MatriX is intended to be mounted on a support to be directly positioned at the end of the Cockroft-Walton arm in the ΠE5 area used for calibration[5, 29], where the MEGII target is positioned. The ΠE5 muon beam energy deposit in MatriX corresponds to the whole initial kinetic energy of the particles (3.7 MeV, Ch. 2) and the energy deposit for minimum ionising positrons is $\sim$ 0.5 MeV.

The current design of the MatriX detector consists of 81 BC-400 (organic) scintillating crystals[38] positioned in a 9×9 grid. The elements are spaced 6 mm apart. Each crystal is coupled to an S13360-1350PE Hamamatsu[34] SiPM through optical grease (Saint-Gobain BC-631[35]).

Due to its segmented design, MatriX is able to measure eventual correlations between the two transverse directions of the beam without any particular request on the trigger. In fact the scalers intrinsically consist of a bidimensional scan of the beam.

In the next section the performances of the current design and possible optimizations that can be done by substituting the scintillating material or the SiPM model will be discussed: a possible candidate for the scintillating material could be LYSO[19], an inorganic scintillator with a high light yield and a high radiation hardness; a possible alternative for the SiPMs could be the 25 μm pitch model (S13360-1325PE Hamamatsu[34]).

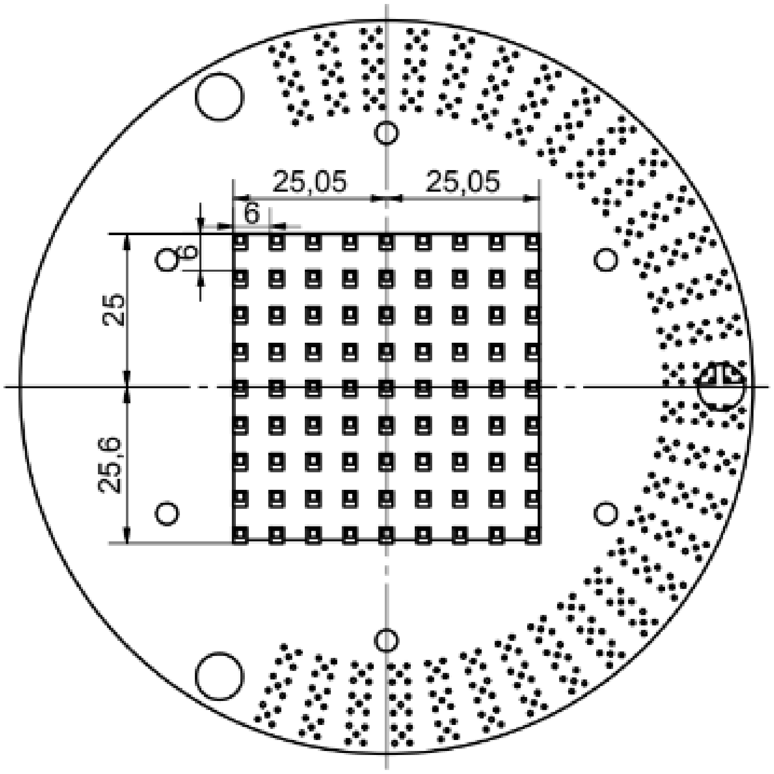

Figure 4.3: *MatriX detector project.*

4.2 Single element: single crystal simulations

4.2.1 Single Element description

The MatriX detector consists in 81 elements composed of a plastic scintillating crystal ($2\times2\times2$ mm^3 Saint Gobain BC-400[38]) coupled to a SiPM (Hamamatsu S13360-13PE[34]) through optical grease (Saint Gobain BC-631[35]). The elements are spaced 6 mm apart.

The minimum requests for the properties of the crystals are: high scintillation yield, fast decay time, emission spectrum fitting the absorption spectrum of the SiPMs. In the next paragraphs LYSO crystals, Lutetium based scintillation crystal doped with Cerium, will be considered[19].

The information about BC-400 and LYSO are collected in Tab. 4.1.

Scintillating crystals properties		
	BC-400	LYSO
No. photons per MeV	$\sim$ 11000	$\sim$ 33000
Rise time [ns]	0.9	-
Decay time [ns]	2.4	36
Wavelength of max. emission [ns]	423	420
Light attenuation length [cm]	160	20[46][47]
No. H atoms per cm^3	5.23	-
No. C atoms per cm^3	4.74	-
Ratio H:C atoms	1.103	-
No. of electrons per cm^3	3.37	-
Density [g/cm^3]	1.023	7.1
Refractive index	1.58	1.81

Table 4.1: *Saint Gobain scintillating crystals properties[38][19].*

The emission spectra of the considered scintillating materials are shown in Fig. 4.4. The emission spectra extracted using WebPlotDigitizer[39] are given in Fig. 4.5.

In the next paragraphs the first sanity checks on the simulation will be discussed .

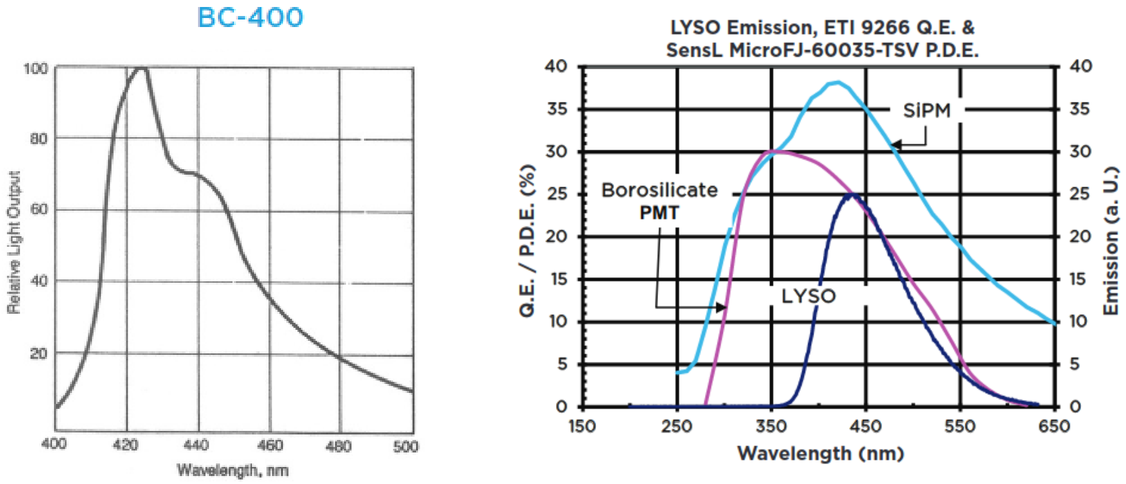

(a) BC-400

(b) LYSO

Figure 4.4: *Emission spectra of the considered crystals[38][19].*

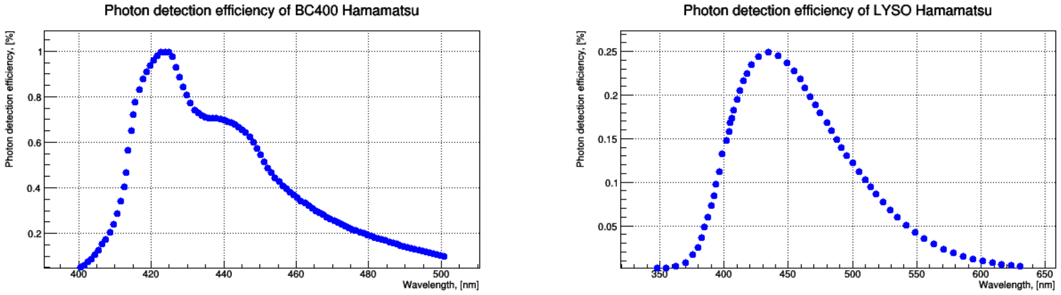

(a) BC-400

(b) LYSO

Figure 4.5: *Emission spectra of the considered crystals[38][19] extracted from the imaged in Fig. 4.4[39].*

4.2.2 Sanity checks

Simulations without the SiPM

Before implementing the SiPMs in the single element simulation, simulations have been run of the only scintillating crystals exposed to a positron beam. In this simulations the dependence of the energy deposit in BC-400 crystals for different initial kinetic energies and different crystal sizes has been checked.

Fig. 4.6 shows a typical energy deposit spectrum in a 2×2×2 mm^3 BC-400 crystal of a 2.2 MeV positron. It is fitted to a Landau distribution through χ^2 minimization.

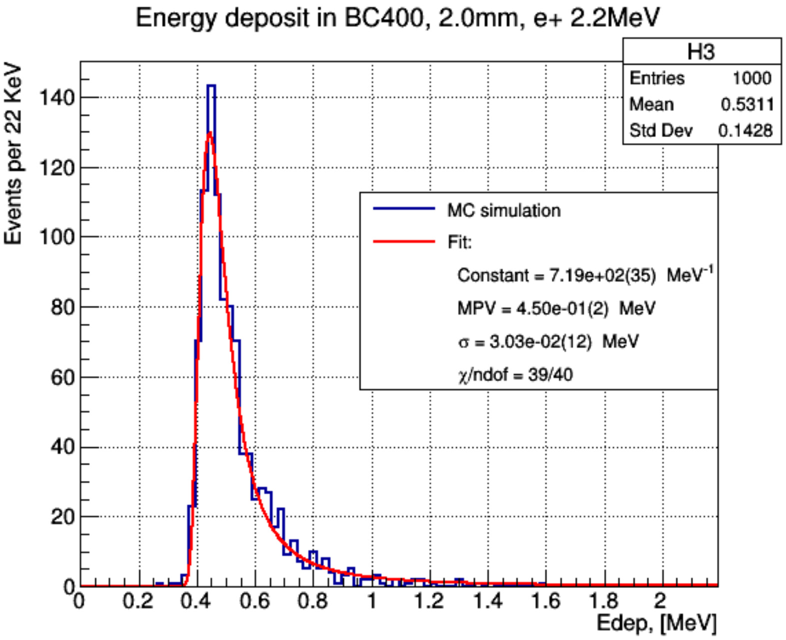

Figure 4.6: *2.2 MeV positron deposit in 2 mm sized cube of BC-400. The fitting function is a Landau distribution with the following parameter: constant = (4.6 ± 0.2) 10^2 MeV^{-1}, MPV = (4.47 ± 0.02) 10^{-1} MeV, σ = (2.80 ± 0.11) 10^{-2} MeV. χ/ndof = 81/54.*

Simulation in different conditions, varying the sizes of the crystal and the initial kinetic energy of the positrons have been run. The conditions are summarized in Tab. 4.2.

Deposit energy sanity check runs conditions		
Crystal size [mm]		
2	10	20
Initial kinetic energy [MeV]		
0.1	0.5	1.0
2.2	28	50

Table 4.2: *Sanity checks runs for deposit energy of positrons in BC-400[38].*

Fig. 4.7 and 4.8 show a summary of the sanity checks performed this way. The runs are collected in Ap. B , Fig. B.1, B.2 and B.3.

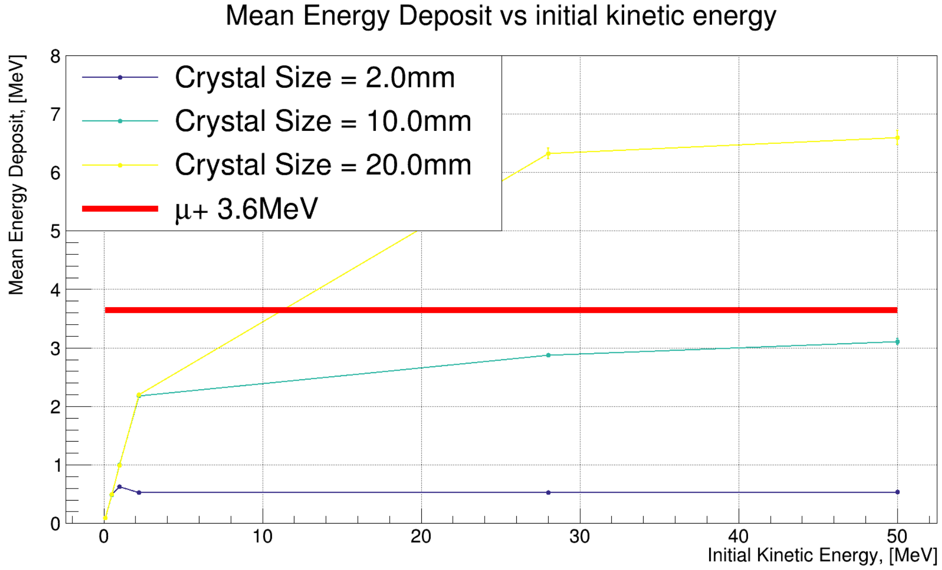

Figure 4.7: *Mean energy deposit of positrons in BC-400[38] vs initial kinetic energy for different crystal sizes. In red the deposit energy for 28 MeV/c momentum muons.*

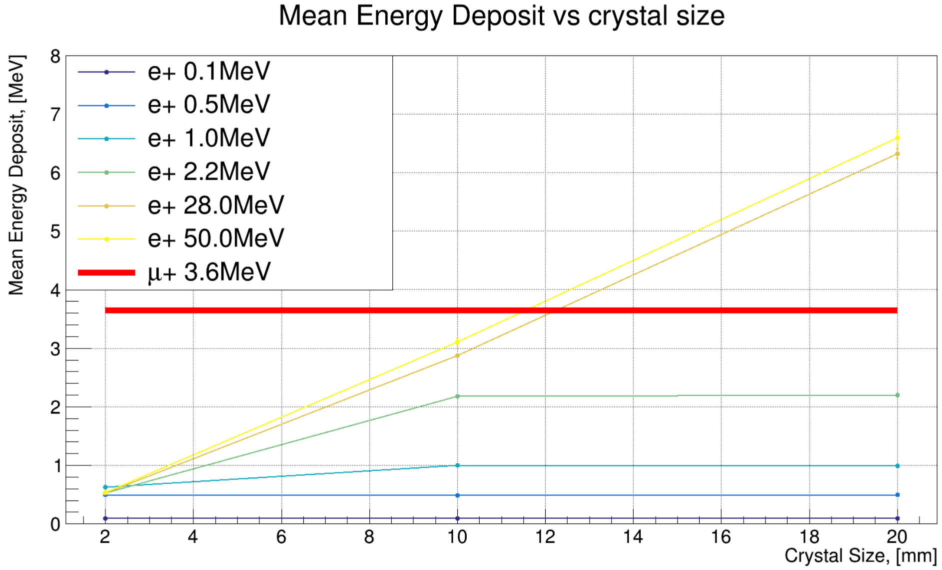

Figure 4.8: *Mean energy deposit of positrons in BC-400[38] vs the crystal size for different initial kinetic energies. In red the deposit energy for 28 MeV/c momentum muons.*

The energy deposit of positrons is almost constant in the 2 mm sized cube of BC-400[38]: in fact due to their light mass, positrons become soon minimum ionizing particles.

Simulation with non active SiPM

The next step was to check for the effect of the SiPM window when in contact with the back surface of the crystal. To do so an empty volume with a refractive index equal to 1.55[34], has been added behind the crystal. The surfaces of the crystal are perfectly polished and the window is centered along the axis of the crystal.

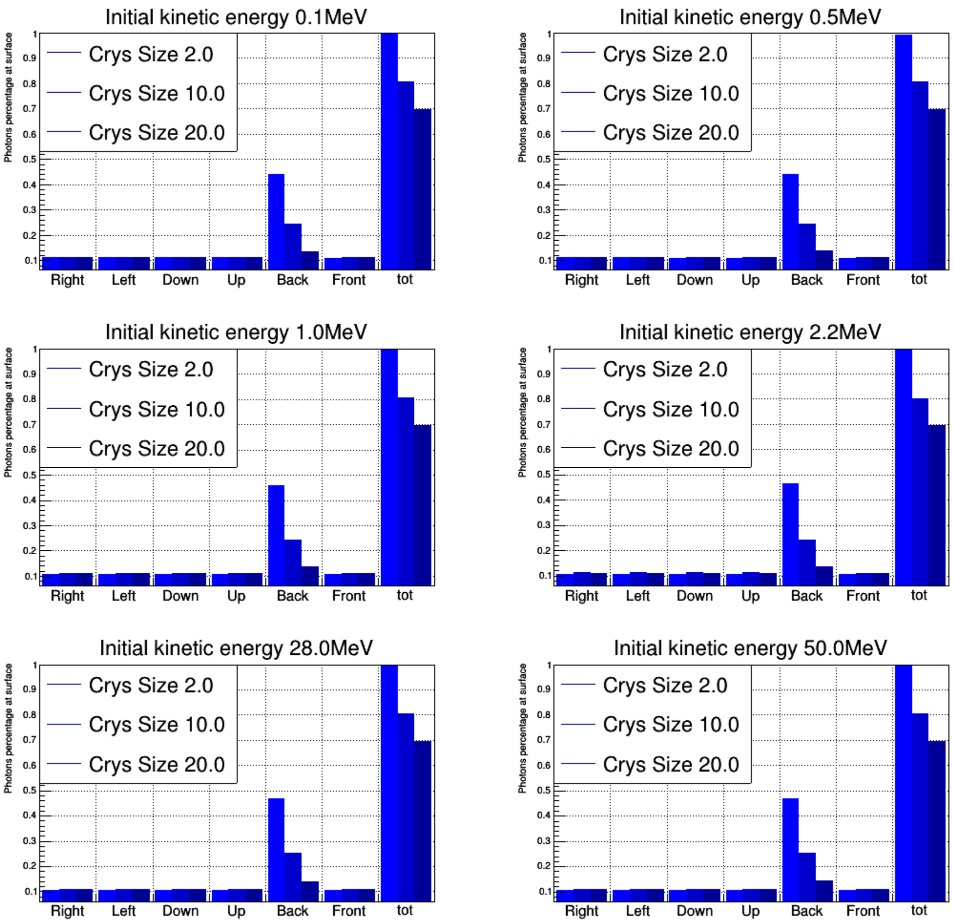

Figure 4.9: *Fraction of photons escaping the crystal through each surface after the passage of a positron through BC-400[38], at different initial kinetic energies and crystal sizes. The surfaces are labelled with respect to the upstream side of the element: the frontal surface is the first one to be hit by the particles; the back surface is the one in contact with the SiPM.*

Fig. 4.9 shows the fraction of photons escaping the crystal through each surface after the passage of a positron through BC-400[38], at different initial kinetic energies and crystal sizes. The fraction of photons escaping the crystal from the back surface depends on the crystal size, while the other do not. This is due to the presence of a volume with higher refraction index directly in contact with the crystal: the element is simulated in vacuum, so that the photons escaping from the back surface are a sum of those that are directly emitted in a direction that allows them to go out, and those that are reflected inside the crystal until they reach the window of the SiPM. Most of the photons escaping through the other surfaces are directly emitted in a direction that allows them to exit without reflections.

This explains why the total amount of photons escaping the crystal decreases when the size increases: the photons that exit through the back surface, while reflected, must travel longer distances, increasing the fraction of photons absorbed inside the crystal.

4.3 SiPM

The SiPMs used to build MatriX are S13360-1350PE from Hamamatsu[34]. The simulation is implemented as reported in Sec. 3.3. There is only one difference with respect to the simulation of the SciFi SiPM: the single element simulation of MatriX already takes into account the rejection of the photons that would be revealed in a pixel fired in a window of 20 ns, while the complete detector simulation saves all the information about photons that would be revealed, as in the SciFi one. There isn't any difference between the two cases when the rate is low enough, so that the events don't actually interfere with each other. But when the rate is high enough it is preferable to first merge together the events ordering the arrivals of the photons temporary and then apply the rejection. So this means that the complete detector simulation is more accurate, but the single element one is faster to be processed this way.

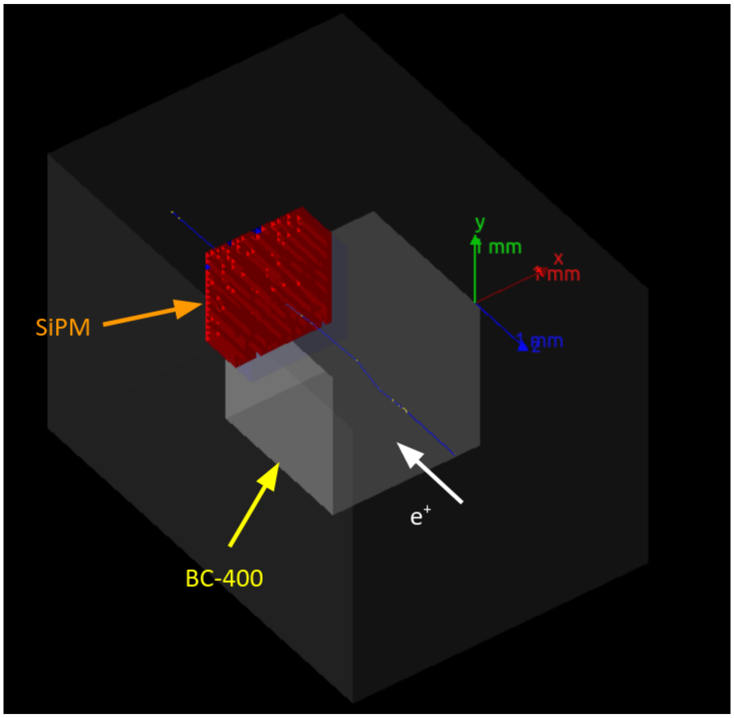

Figure 4.10: *Single MatriX element simulation event: e+, along z axis, passing through the crystal at its center. In red the pixels fired. The photons are not shown in this example to make the figure cleaner.*

This section will refer only to single element simulations, so that the rejection of photons coming from pixel recovery time, is already implemented in the Geant4 level of the simulation.

Here, all the primary particles travel along the z axis (Fig.4.10) and the crystal is perfectly centered and polished.

4.3.1 Implementation specs

As mentioned before the SiPM used in MatriX are of the same series of the SciFi ones. They differ only in three aspects:

- the window that covers the sensitive area is made of epoxy resin, instead of the silicon one of the CS models. In the simulation the window is an empty volume with a refractive index equal to 1.55[34] (see Tab. 4.3);
- the PDE is different (see Fig. 4.11 and 4.12);
- the sizes are different (see Fig.4.13 and 4.14 and Tab. 4.3).

Except for the aspects mentioned above, the implementation of the SiPMs in MatriX is the same as for the SciFi ones, and the flowchart is the same as in Fig. 3.13.

In the next paragraph a comparison between the performances of the 50 μm pitch model and the performances of the 25 μm pitch one will be given. Their characteristics are collected in Tab. 4.3.

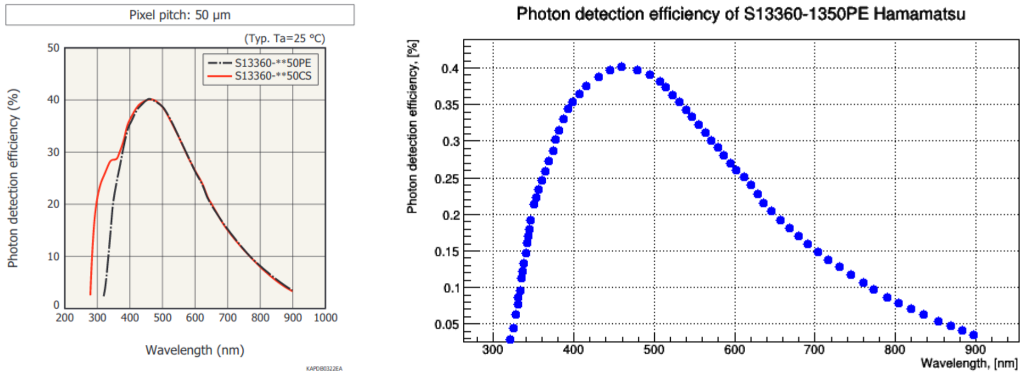

(a) PDE in the datasheet

(b) PDE extracted from the one on the left

Figure 4.11: *Photon detection efficiency as a function of incoming photons wavelength of an S13360-1350PE Hamamatsu SiPM. On the left the PDE as shown in [34]. On the right the PDE as extracted using WebPlotDigitizer[39].*

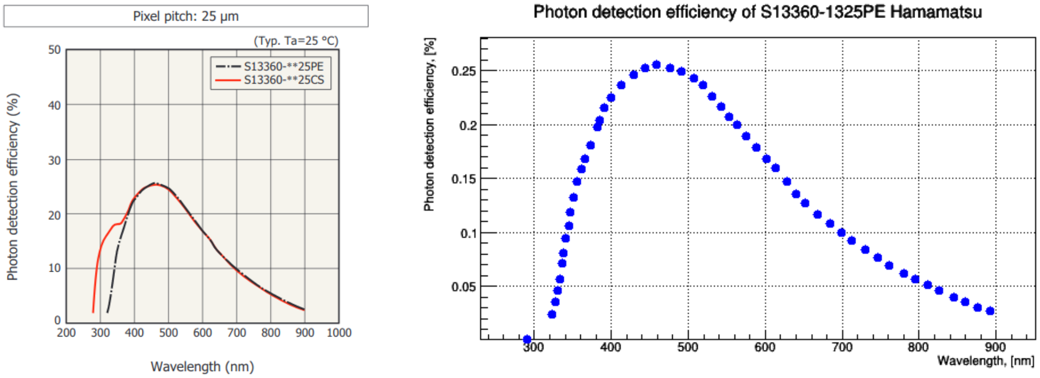

(a) PDE in the datasheet

(b) PDE extracted from the one on the left

Figure 4.12: *Photon detection efficiency as a function of incoming photons wavelength of an S13360-1325PE Hamamatsu SiPM. On the left the PDE as shown in [34]. On the right the PDE as extracted using WebPlotDigitizer[39].*

SiPM height [mm]	SiPM width[mm]	Pixel volume height [mm]	Window height [mm]
0.85	1.3	0.55	0.3

No. of pixel in 50 μm pitch model	No. of pixel in 25 μm pitch model
667 (29$\times$23)	2668 (58$\times$46)

Table 4.3: SiPM sensor size and number of pixels[34].

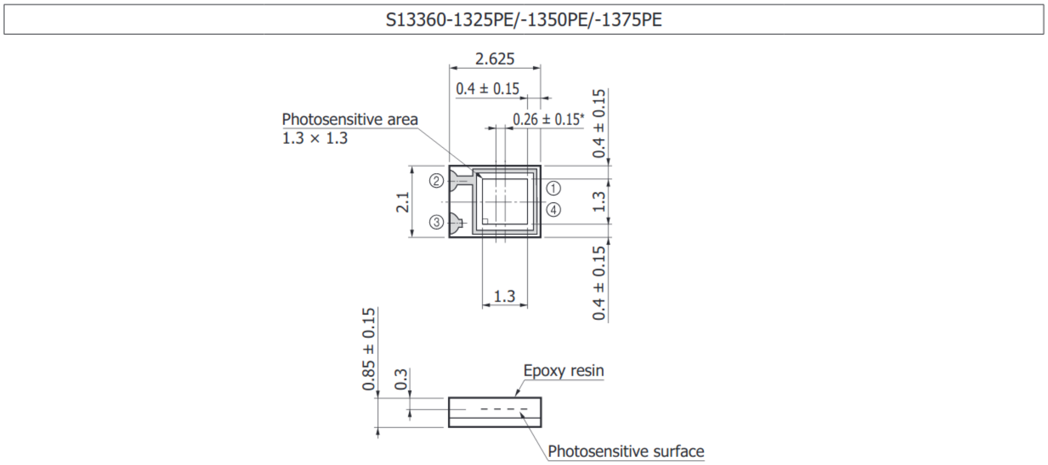

Figure 4.13: *Dimensional outlines of an S13360-1350PE Hamamatsu SiPM[34].*

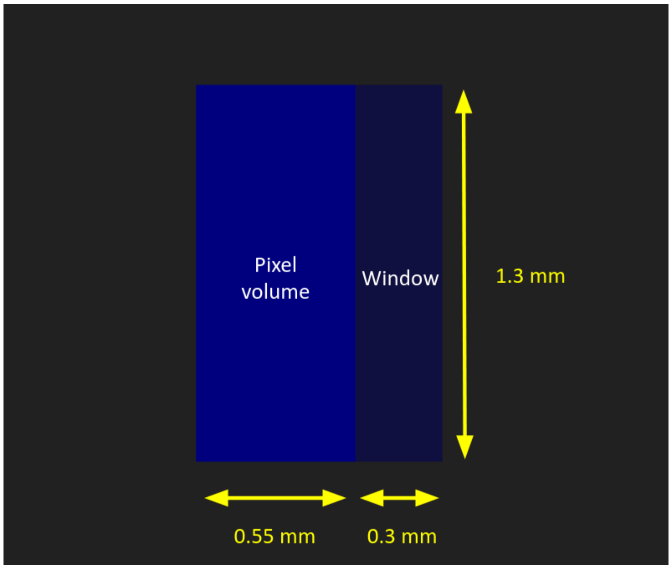

Figure 4.14: *Simulated S13360-1350PE Hamamatsu SiPM.*

4.3.2 Spectra separation and LYSO studies

In this paragraph the amplitude spectra of different particles impinging on the current detector are discussed, followed by the possible optimization coming from the use of LYSO and from the 25 μm pitch SiPMs.

The response of the single MatriX element is simulated for the following particles:

- e^+: the initial kinetic energies considered are 2.2 MeV (endpoint of ^{39}Sr emission spectrum) and 52.8 MeV (endpoint of Michel spectrum);
- μ^+: the initial momentum considered is 28 MeV/c;
- π^-: the initial momentum considered is 70.5 MeV/c;
- α: the initial kinetic energy considered is 4.5 MeV.

All the particles listed above were simulated as a monochromatic beam perfectly aligned along the beam axis at the center of the element. Later more realistic configurations are given. In the case of BC-400 only the current size of the crystals is considered: $2\times2\times2$ mm^3. In the case of LYSO the thickness of the crystal is varied while keeping the height and the width constant at 2 mm, as shown in Tab. 4.4.

LYSO crystals thicknesses in single MatriX element simulations [mm]				
0.1	0.2	0.3	0.4	0.5

Table 4.4: LYSO crystals thicknesses in single MatriX element simulations.

The thickness of the LYSO crystal has been varied in order to optimise the separation between stopped μ^+/m.i.p.. A comparison with the equivalent thickness to reproduce the BC-400 element when coupled to SiPMs has been done.
The SiPM considered are S13360-1350PE and S13360-1325PE by Hamamatsu[34], whose specifications are collected in paragraph 4.3.1

Fig.4.15 shows a comparison between the scintillation yield of BC-400 and LYSO obtained collecting all the simulations above together.

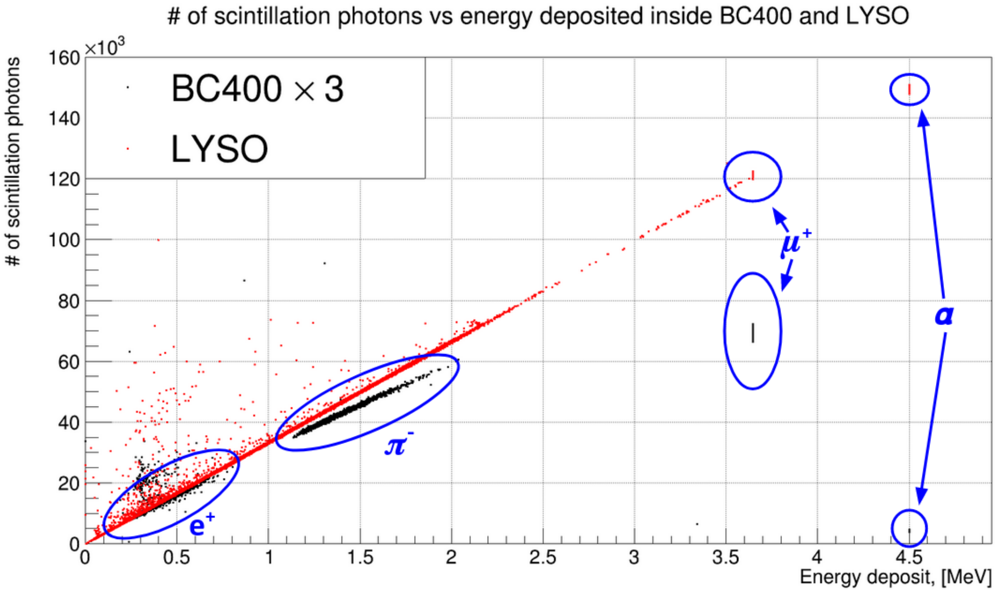

Figure 4.15: *comparison between the scintillation yield of BC-400 and LYSO. It is possible to see the effect of the Birks saturation in BC-400 particularly for the α particles, that deposit a high amount of energy along a short path.*

It is possible to see a high loss in linearity for low β particles, like muons and alphas, through BC-400: at this level is already possible to state that LYSO crystals would improve the separation between positrons and muons. This is crucial, because the background while measuring muon beams, consists of Michel positron from muons decaying inside the elements. This aspect will be discussed more in detail in the next section.

There is another source of loss in linearity response due to the dynamic range of the SiPMs: Fig. 4.16 shows a comparison between the number of pixels fired by particles through BC-400 and LYSO, using 50 or 25 μm pitch SiPMs.

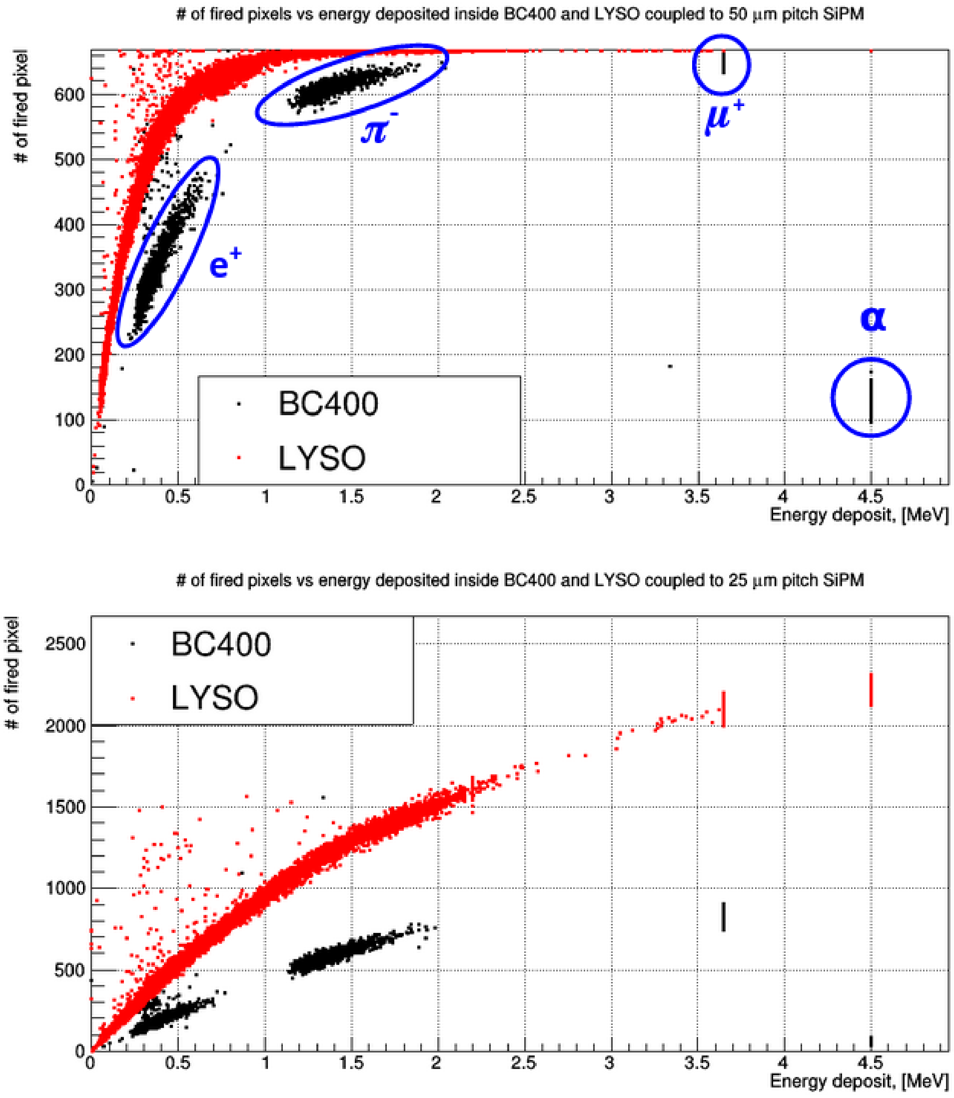

Figure 4.16: *comparison between the number of pixels fired by particles through BC-400 and LYSO. In the plot above, there are BC-400 and LYSO coupled to 50 μm pitch SiPM. In the plot below there are BC-400 and LYSO coupled to 25 μm pitch SiPM.*

It is possible to see that using 25 μm pitch SiPM would improve the separation between muons and positrons even using BC-400 as scintillating material.

In Fig. 4.17 and 4.18 are collected the spectra reported above in number of pixels fired, divided by crystal material and thickness.

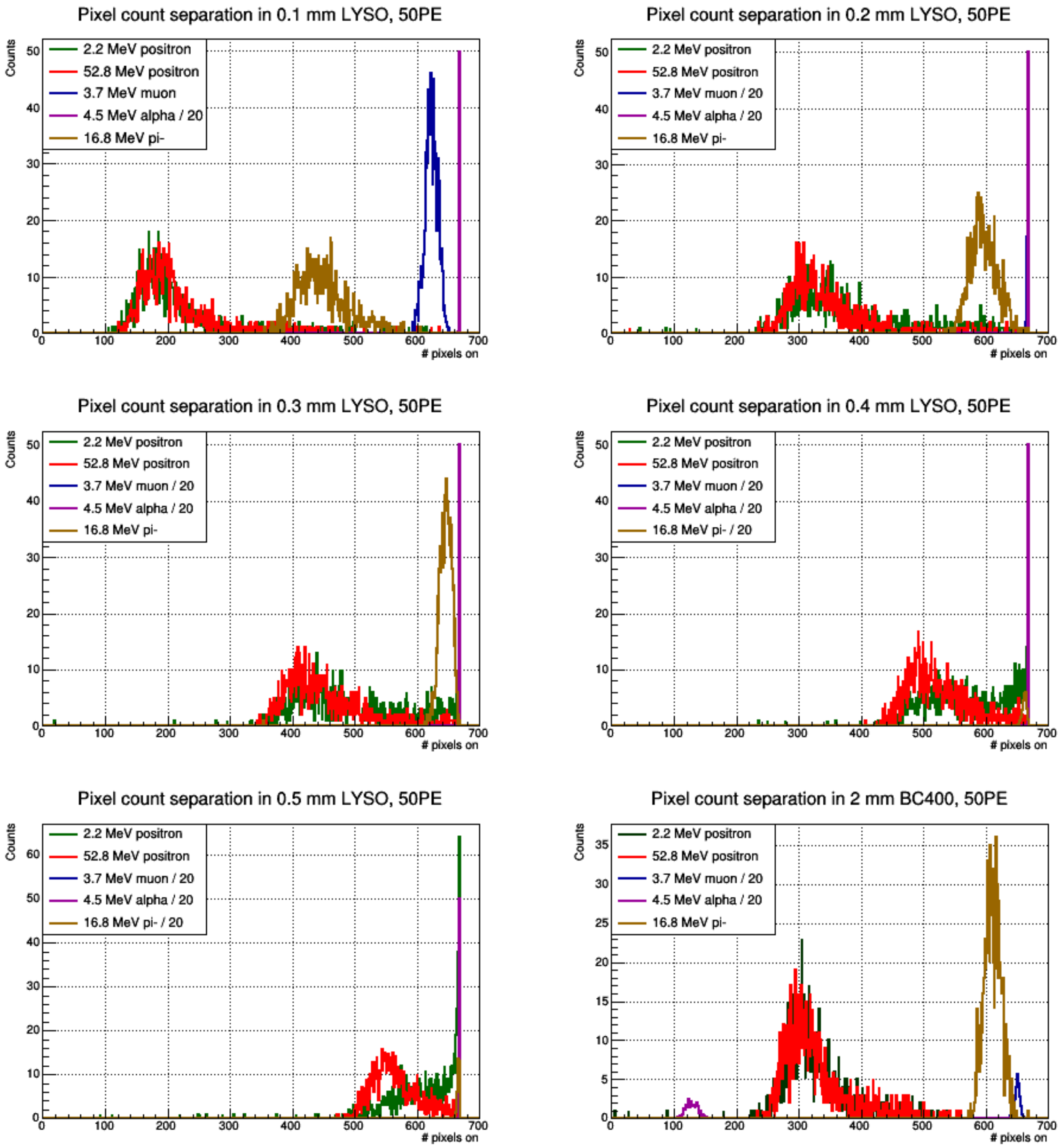

Figure 4.17: *Particles spectra in number of fired pixels for different crystal materials and thicknesses using 50 μm pitch SiPMs. The particles considered are: 2.2 and 52.8 MeV initial kinetic energy positrons; 70.5 MeV/c momentum negative; 28 MeV/c momentum; 4.5 MeV initial kinetic energy alphas.*

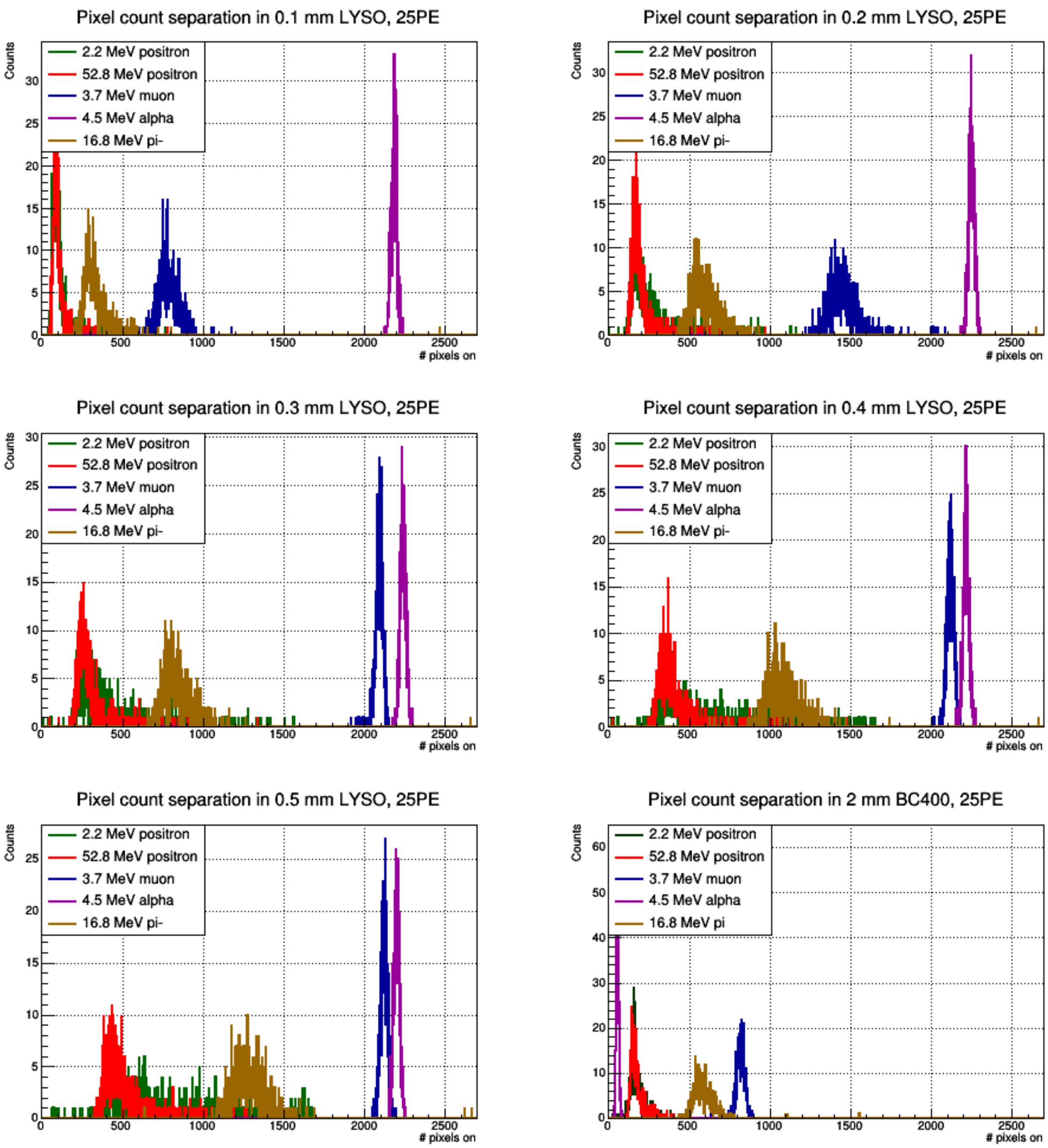

Figure 4.18: *Particles spectra in number of fired pixels for different crystal materials and thicknesses using 25 μm pitch SiPMs. The particles considered are: 2.2 and 52.8 MeV initial kinetic energy positrons; 70.5 MeV/c momentum negative; 28 MeV/c momentum; 4.5 MeV initial kinetic energy alphas.*

In order to find the thickness of LYSO equivalent to 2 mm BC-400, the most probable values dependence on the crystal thickness has been fitted. The most probable value is extrapolated fitting the spectra with a Landau distribution.

The conversion factor has been evaluated using 2.2 and 52.8 MeV positrons. In the case of 2.2 MeV positrons, the 0.5 mm value was not included and the fitting function is linear, because the energy deposit is too high with respect to the initial kinetic energy (see Fig: 4.17 and 4.18). In the case of 52.8 MeV positron the fitting function is quadratic to consider the saturation effects.

The fit parameters are collected in Tab. 4.5.

Fit parameters of the number of pixels fired dependence on the LYSO thickness				
	2.2 MeV positrons		52.8 MeV positrons	
SiPM pitch [μm]	50	25	50	25
offset	30 $\pm$ 3	-10 $\pm$ 2	19 $\pm$ 3	4 $\pm$ 2
linear coefficient [mm^{-1}]	1446 $\pm$ 25	906 $\pm$ 19	1726 $\pm$ 26	773 $\pm$ 26
quadratic coefficient [mm^{-2}]	/	/	-1337 $\pm$ 42	214 $\pm$ 54
conversion factor (LYSO thickness / BC-400 thickness)	9.34 $\pm$ 5 10^{-2}	9.05 $\pm$ 5 10^{-2}	9.38 $\pm$ 5 10^{-2}	8.95 $\pm$ 5 10^{-2}

Table 4.5: Parameters used to evaluate the conversion factor between LYSO and BC-400 thicknesses.in the last row the conversion factors.

The conversion factor between LYSO and BC-400 thickness, collected in Tab. 4.5 has been evaluated inverting the fit functions and calculated the LYSO thickness corresponding to the most probable value of the positron spectra in number of pixels fired (see Fig. 4.17 and 4.18).

The error on the conversion factor is evaluated using the covariance matrices in Ap. C.

The results are summarized in Fig. 4.19 and 4.20.

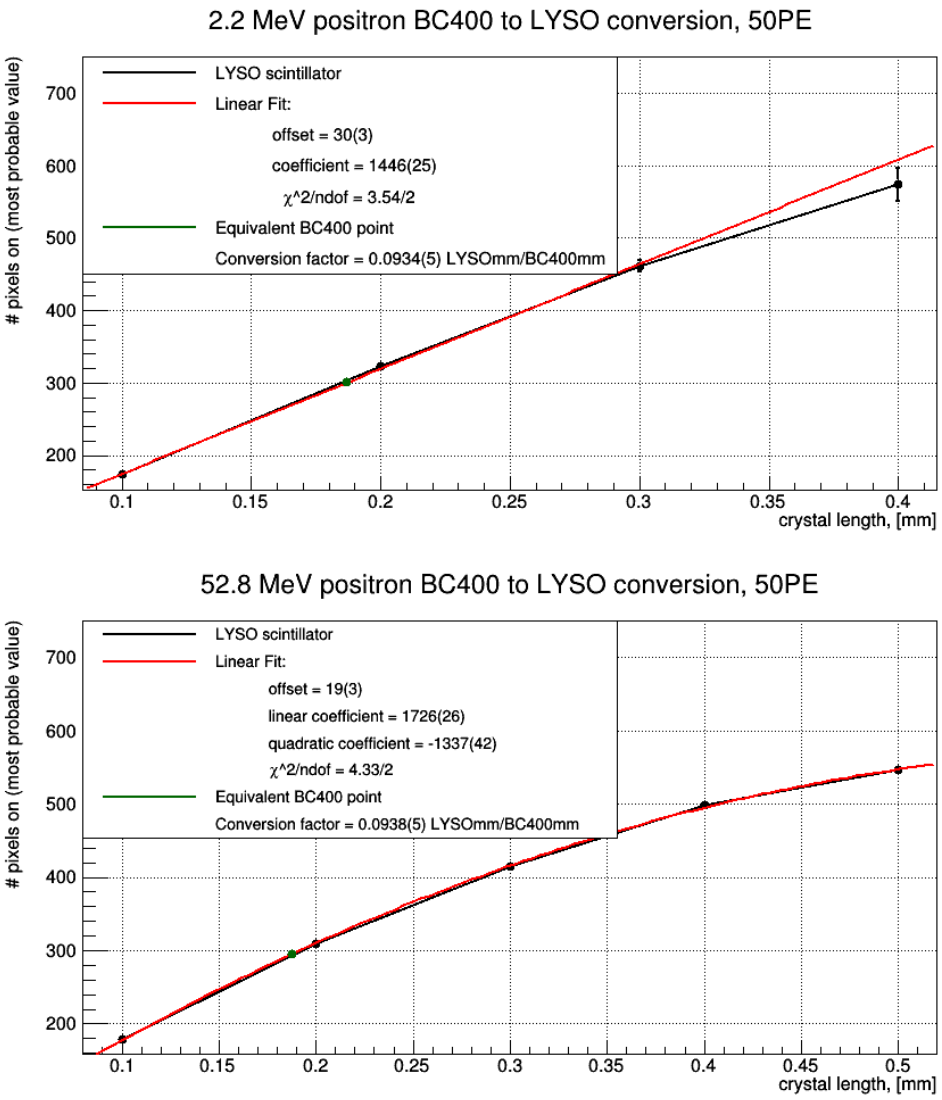

Figure 4.19: *Number of pixels fired vs LYSO crystals thickness using 50 μm pitch SiPMs. In the plot above the fitting function is linear, while in the plot below it is quadratic. Using the BC-400 most probable value of the number of pixels fired the conversion factor to obtain the equivalent LYSO thickness has been evaluated. In this case the value obtained is 0.0934 $\pm$ 0.0005 for the 2.2 MeV positrons (above), and 0.0938 $\pm$ 0.0005 for the 52.8 MeV positrons (below). The two values are consistent*

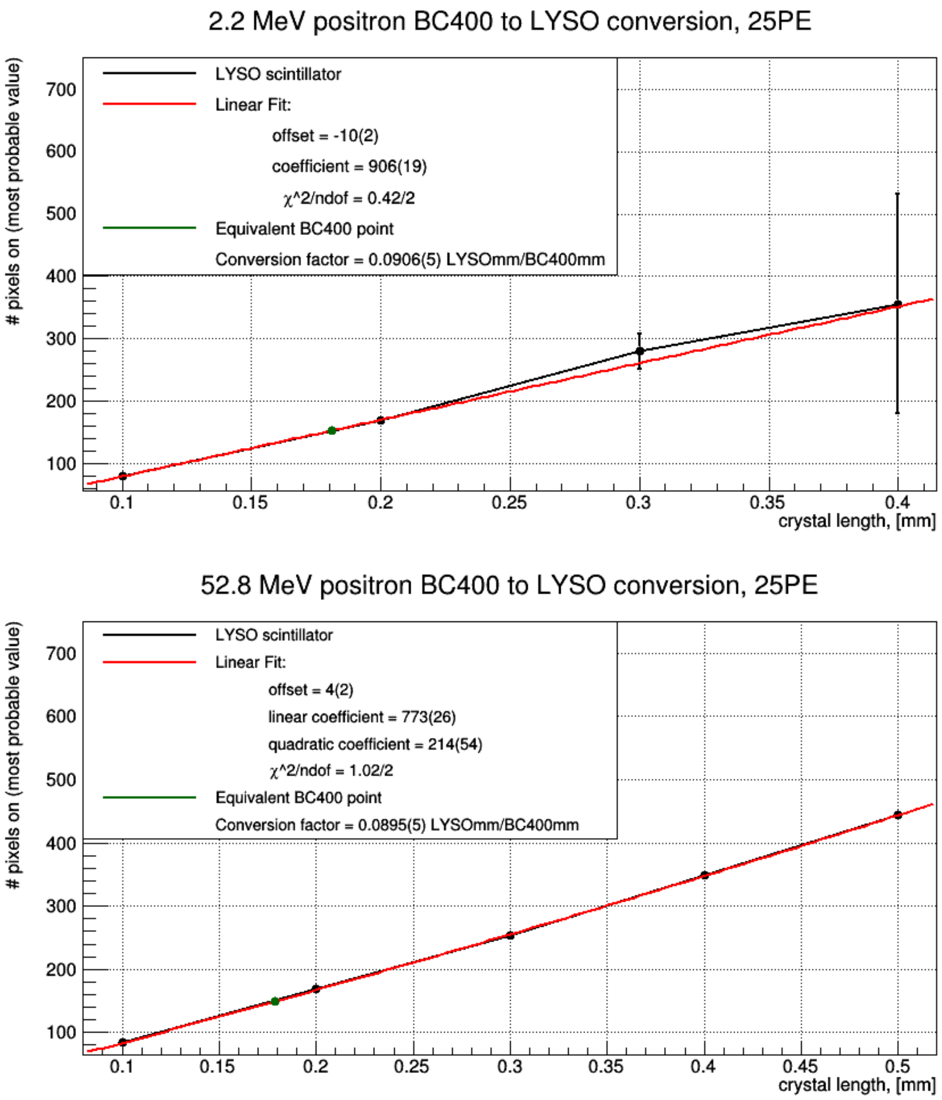

Figure 4.20: *Number of pixels fired vs LYSO crystals thickness using 25 μm pitch SiPMs. In the plot above the fitting function is linear, while in the plot below it is quadratic. Using the BC-400 most probable value of the number of pixels fired the conversion factor to obtain the equivalent LYSO thickness has been evaluated. In this case the value obtained is 0.0905 ± 0.0005 for the 2.2 MeV positrons (above), and 0.0895 ± 0.0005 for the 52.8 MeV positrons (below). The two values are consistent*

Using the conversions factors above the mean value of the LYSO equivalent thickness ($\mathrm{LYSO}_{\mathrm{eq,th}}$) would be:

$$\mathrm{LYSO}_{\mathrm{eq,th}} = <\mathrm{conversion\,factor}> \times\ 2\,mm = 9.1810^{-2} \times 2\,mm \sim 180\,\mu m \tag{4.1}$$

This value is not related to the energy deposit itself but rather to the number of pixels fired: in fact, the range of 28 MeV/c momentum muons in LYSO is $\sim 270\ \mu$m (see Fig. 4.21).

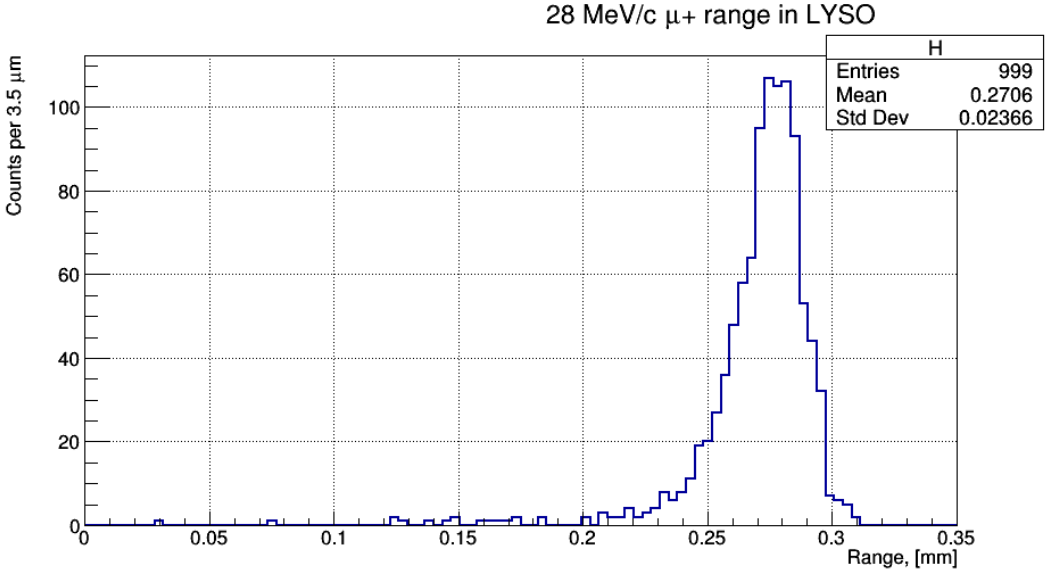

Figure 4.21: *Range of 28 MeV/c momentum* μ^+ *in LYSO.*

Taking into account this information, the best thickness for LYSO crystals in order to separate at best muons and Michel positrons in energy deposit would be $\sim 300\ \mu$m. But using such a thickness with 50 μm pitch SiPMs would reduce the performances of the detector, hitting on the saturation effect. The possibilities to take into account for the final version of the detector are:

- 200 μm LYSO crystals coupled to 50 μm pitch SiPMs: this would lead to high energy deposit directly inside the SiPMs and evaluations on radiation damage would be necessary;
- 300 μm LYSO crystals coupled to 25 μm pitch SiPMs: this would be the optimal condition and the light output would not compromise the SiPMs performances.

In any case the plots shown above do not take into account the time arrival distribution of the photons on the SiPMs: due to its scintillation process, LYSO has a high emission decay time and this effect has to be taken into account when evaluating the actual performances of the detector. Fig. 4.22 shows an example of muon signal in LYSO: the LYSO is 250 μm thick, the size of the samples currently present at PSI, and the SiPM model is 25PE.

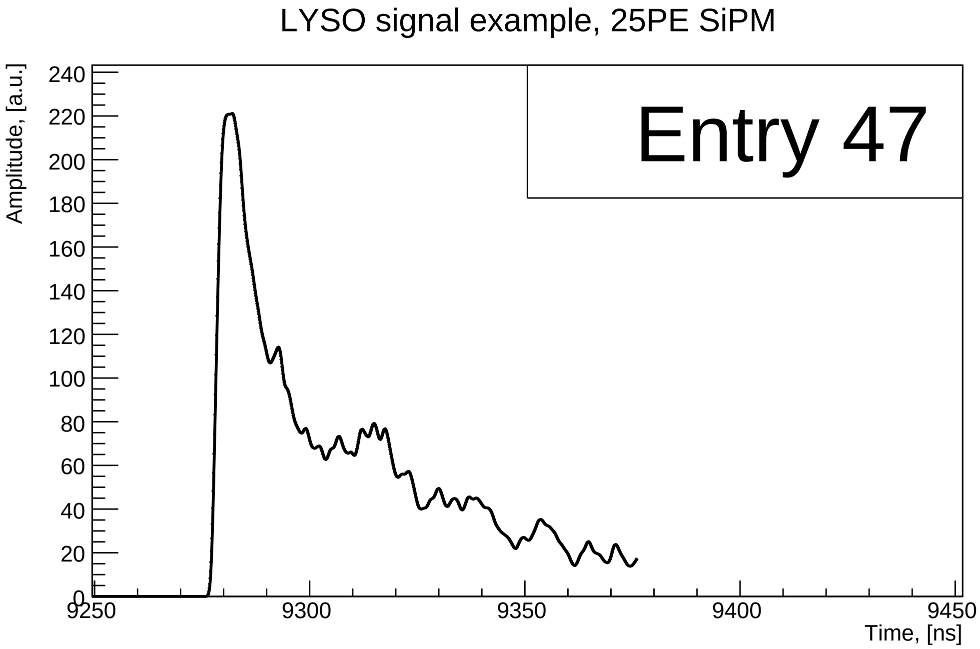

Figure 4.22: *Signal of a muon passing through LYSO.*

During my thesis work I did not deepen on this topic, but surely it will need further studies.

4.4 Complete detector

To simulate the complete detector 81 BC-400 2 mm sized crystals coupled to SiPMs have been placed, as in Fig. 4.3. The back surfaces of the SiPMs are in contact with the PCB: a 4 mm high silicon cylinder, with a 6 cm radius. Fig. 4.23 shows the simulated MatriX detector.

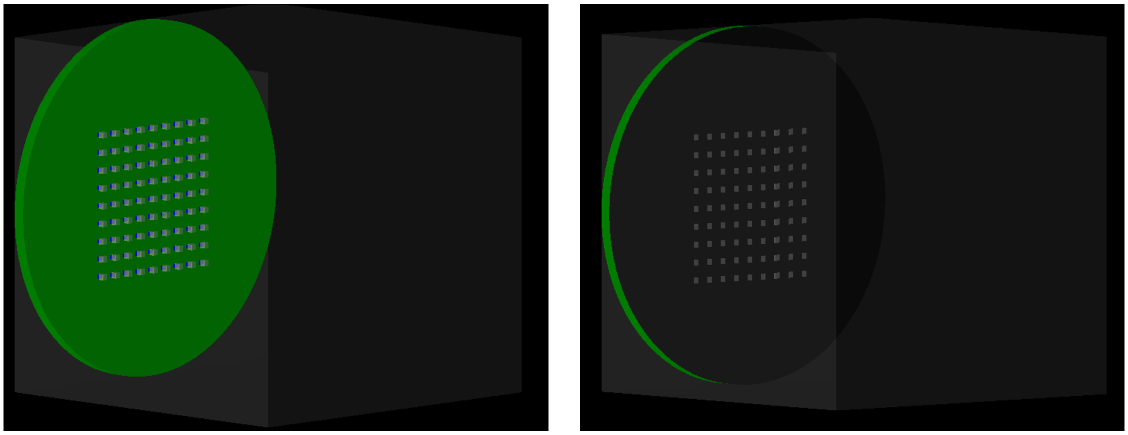
(a) Naked view. (b) Mask view.

Figure 4.23: *Complete MatriX detector simulation view.*

In this section only the S13360-1350PE Hamamatsu SiPMs[34] are simulated, because this is the model currently used for the prototype at PSI. Furthermore, as shown in Fig. 4.1, in the current prototype the crystals are held in place by a plastic mask: in the simulation there is the possibility to add a polyethylene mask. It has the same radius as the PCB but is as high as the single element: 2 mm (crystal) + 0.85 mm (SiPM). The holes on the mask are 2.01 mm sized squares: making the holes slightly bigger then the crystals allows to avoid transmission problems with photons at the interface between the crystals and the mask. In fact the mask absorbs the optical photons escaping the crystal, but they are actually refracted or reflected as they would be in air: the mask does not fit perfectly the element, there is always air between a crystal and the mask.

Fig. 4.23 shows the complete detector simulation with the mask.

As already mentioned in the previous sections, the simulation of the complete detector does not include the rejection of photons arriving on an already fired pixel: it is implemented in the macro that elaborates the SiPMs output signals.

In this section the major aspects emerging from the simulations are discussed:

- the effects of the mask on the measurements;
- the reconstruction algorithm;
- the expected time needed to perform rate measurements under per cent resolution.

In any case these considerations have to be taken as preliminary: for further details and to evaluate the resolution limits of the apparatus, a tuning with beam data is needed.

4.4.1 Spectra

Before discussing the reconstruction algorithm, is important to point out the response of the detector to the different particle beams considered.

In order to do so two variables have been introduced to separate the different contributions to the amplitude spectra, particularly in the muon one:

- *time event*: it is the time elapsed between the start of the event and the moment the first photon in the waveform is revealed;
- *track length*: it is the track length of the primary particle inside the BC-400 crystal.

Through *time event* it is possible to separate the amplitudes related to the primary particles from their decay products. In the case of the ΠE5 line at PSI, it is necessary only for muons: they are the only particles that have a sufficiently low energy to make them stop inside the crystals, and then decay.

Through *track length* it is possible to separate Michel positrons coming from muon decay inside the crystals or inside other components of the detector: mask, if present, or the PCB.

Monochromatic gaussian beams with no divergence, centered along the detector axis are simulated. Fig. 4.24 shows the spectra of the different particle beams considered. Tab. 4.6 shows the width (standard deviations) and energies of the beam used for these simulations. All the beams are perfectly symmetric (same standard deviations in the two directions) and all the simulations are performed with the mask applied to the detector.

Fig.4.24 will be discussed in detail.

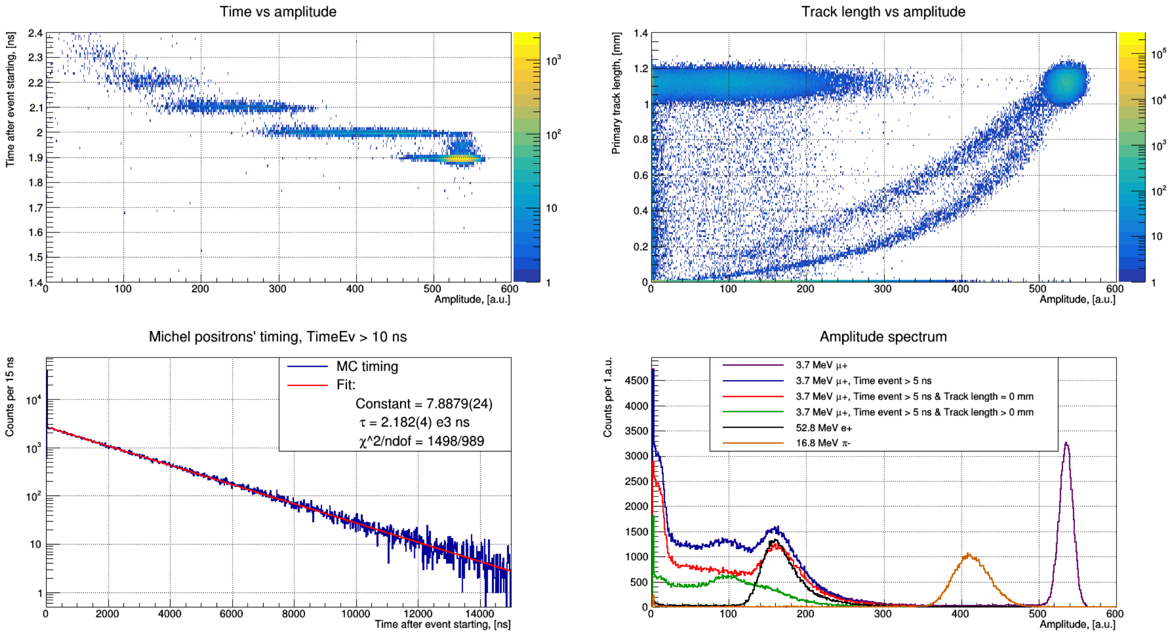

Figure 4.24: *From left to right, from top to bottom: muon beam time event vs amplitude, with the cut time event $<$ 2.4 ns; muon beam track length vs amplitude; muon beam time event histogram; different particle beams amplitude spectra comparison. The beam characteristics are collected in Tab. 4.6.*

Particle	Initial kinetic energy (momentum) [MeV]	Beam width [mm]
e^+	52.8	20
μ^+	3.7 (28)	20
π^-	16.8 (70.5)	8

Table 4.6: Beam characteristics used in the simulations to evaluate MatriX response.

The *time event* structures in the upper-left plot is related to the steps been used in the macro: the signals are generated in steps 0.1 ns long.

Comparing the upper-left plot with the downer-left plot shows the characteristic time of the primary particles signals and of the secondary particles signals arrival: the fit in the downer-left plot is performed with an exponential function. The decay time obtained is not compatible with the muon decay time (2.197034(21) μs[12]), but it is actually strongly dependent on the fit window and it is not trivial to take into account all the effects involved. For the purpose of my work this is not something crucial, and this aspect will not be discussed. It is important to point out that the decay constant extrapolated with the fit is of the same order of magnitude of muon decay time.

The *track length* plot lets clearly individuate the different components of the muon spectra.

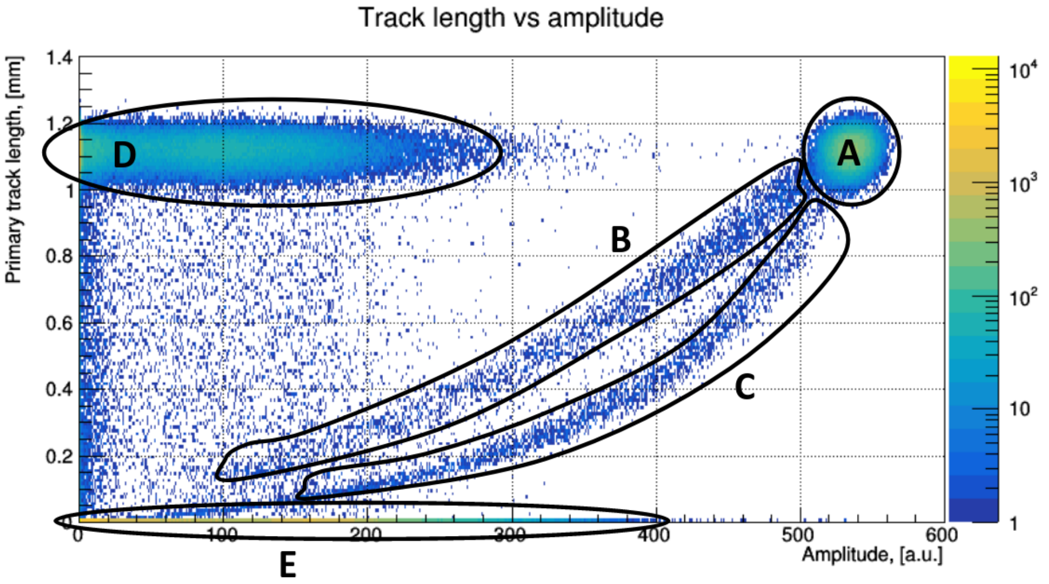

Figure 4.25: *Muon beam track length vs amplitude plot.*

Fig. 4.25 shows a detail of this plot:

- area A: this is the peak of the primary particles fully passing through the crystals. In the case of muons they are the particles that stop inside the crystals;
- area B: these are the particles that enter the crystal and that are scattered out of the crystals;
- area C: these are the particles that are scattered by the mask inside the crystals. These events lead to an overestimate on the rate measurement.
- area D: these are the Michel positrons coming from the muons stopped inside the crystals. In fact they have the same *track length* as the stopped primaries, because *track length* takes into account only the tracks of the primary particles;

- area E: these are the Michel positrons coming from the muons stopped inside the mask. In fact for these events the *track length* is zero: there is no energy deposit of the primary particles inside the crystals.

The downer-right plot in Fig. 4.24 shows a comparison between the pure muon spectra and the Michel positrons contributions.

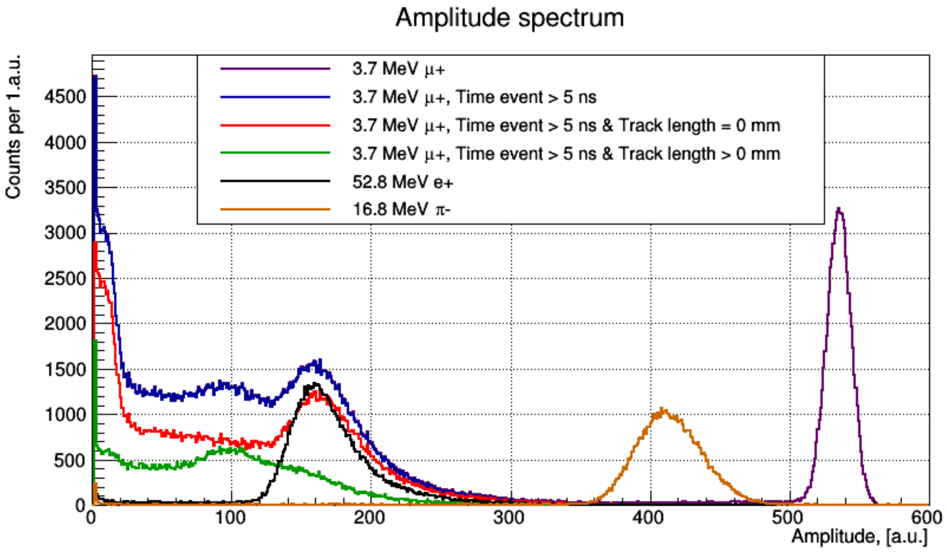

Figure 4.26: *3.7 MeV (28 MeV/c) muon spectrum compared to 52.8 MeV positron spectrum and 16.8 MeV (70.5 MeV/c) pion spectrum.*

Fig.4.26 shows a detail of this plot:

- black histogram: 52.8 MeV positrons;
- brown histogram: 16.8 MeV pion spectrum;
- purple histogram: complete muon spectrum. The low energy region, whose population is composed by Michel positrons, is covered by the blue histogram, which is actually the same histogram at low energy values;
- blue histogram: Michel positron spectrum coming from muon decay on MatriX detector. It is actually a part of the complete muon spectrum in the previous point and it is the sum of the green histogram and the red histogram;

- green histogram: Michel positron coming from muon decay inside scintillating crystals. It has a broad peak at $\sim$ 100 a.u.: the muon range inside BC-400 is $\sim$ 1.1 mm (see Fig. 4.25), so that the average path of the positrons inside the crystal is $\sim$ 1 mm, and the peak is positioned at values lower than the 52.8 MeV positron peak;

- red histogram: Michel positrons coming from muon decay inside the mask. In this case the positrons are produced outside the crystals, causing them to pass through the crystals. It is important to notice that the peak corresponds to the 52.8 MeV positron peak.

There is a good degree of separation between Michel positrons and muons, but the presence of the mask worsens the performances of the detector: in fact, depending on the threshold used to separate the signals, there can be contamination with the Michel positrons.

4.4.2 Beam reconstruction: symmetrical beam

Reconstruction algorithm

The macro that elaborates the response of the detector produces two output files: a ROOT file[8], and a text file. The ROOT file collects the information about the waveforms, while the text file collects the number of time the output of each channel of MatriX is above the chosen threshold. It is possible to do so processing directly the ROOT file instead of the Geant4 level output.
The text file contains the duration of the run too.

In order to extrapolate the information about the shape and the rate of the beam, a macro reads the text file producing a bidimensional histogram and fitting it with a bidimensional Gaussian. The fitting function is:

$$f(x,y) = \frac{A}{2\pi\sigma_x\sigma_y\sqrt{1-\rho^2}} e^{-\frac{1}{2(1-\rho^2)}\left(\frac{(x-\mu_x)^2}{\sigma_x^2} - \frac{2\rho(x-\mu_x)(y-\mu_y)}{\sigma_x\sigma_y} + \frac{(y-\mu_y)^2}{\sigma_y^2}\right)} \tag{4.2}$$

where:

- μ_i is the mean value along the i-th direction;

- σ_i is the standard deviation along the i-th direction;

- ρ is the correlation between the two directions;
- A is the normalization factor.

While for the reconstruction of beam using SciFi the bidimensional fit is performed fixing parameters extrapolated from previous analysis (see Ch. 3), in the case of MatriX all the parameters in eq. 4.2 are free to vary.

Using A and the exposure time it is possible to calculate the beam rate:

$$R = \frac{A}{(crys.\,size)^2\,\Delta T} \tag{4.3}$$

Fig. 4.27 shows an example of beam reconstruction using the output of the MatriX simulation.
The beam to be reconstructed in this case is 20 mm wide in both directions, and centered along the detector axis. The beam rate is 10^7 μ/s. The number of events simulated is 10^7. A 300 a.u. threshold in amplitude has been used.

Tab. 4.7 collects the results of the fit.

μ_x [mm]	σ_x [mm]	μ_y [mm]	σ_y [mm]
-0.03 ± 0.03	20.12 ± 0.05	-0.06 ± 0.03	19.98 ± 0.04

A [mm^2]	ρ	χ^2	ndof
(3.672 ± 0.007) 10^7	-0.003 ± 0.002	60.6	75

Table 4.7: Fit parameters for beam reconstruction example in Fig. 4.27.

The reconstructed beam rate is:

$$R = (1.000 \pm 0.008)10^7\mu/s$$

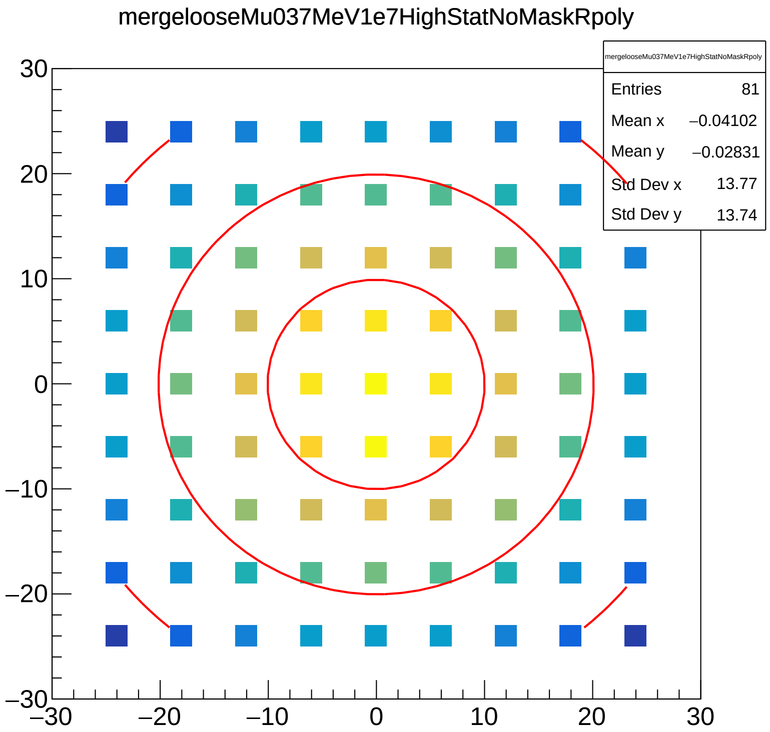

(a) comparison between fit and histogram.

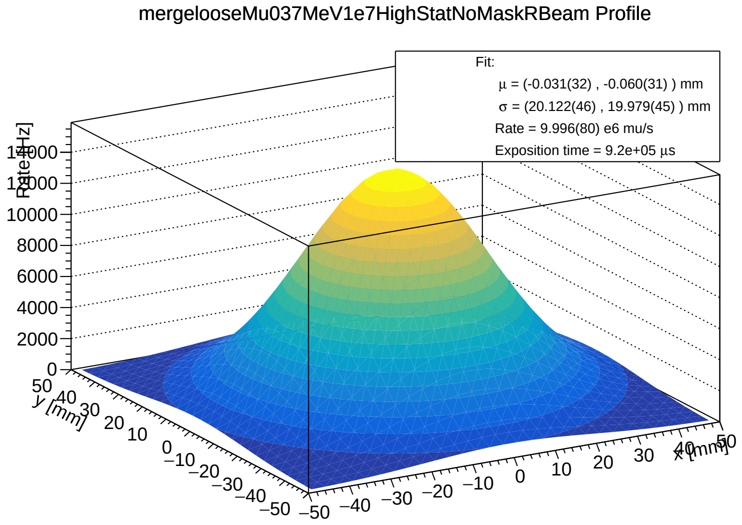

(b) Fitting function profile.

Figure 4.27: *Muon beam reconstruction without the mask. The beam is 20 mm wide in both directions, centered along the detector axis. In this case the beam rate is* 10^7 *μ/s. The threshold chosen in this case is 300 a.u..*

Rate reconstruction dependence on number of generated events

The first aim of MatriX is to provide fast rate measurements with uncertainties below the percent level. This capability has been evaluated dividing a sample of 10^7 52.8 MeV positrons events in smaller samples, in order to find the resolution as a function of the generated events, or better as a function of the number of particles arrived on the detector. It must be underlined that this quantity is different from the number of particles passing through the crystals, so that even a particle that does not interact with the MatriX elements is considered as an event.

Fig. 4.28 shows the uncertainty dependence on the number of generated events.

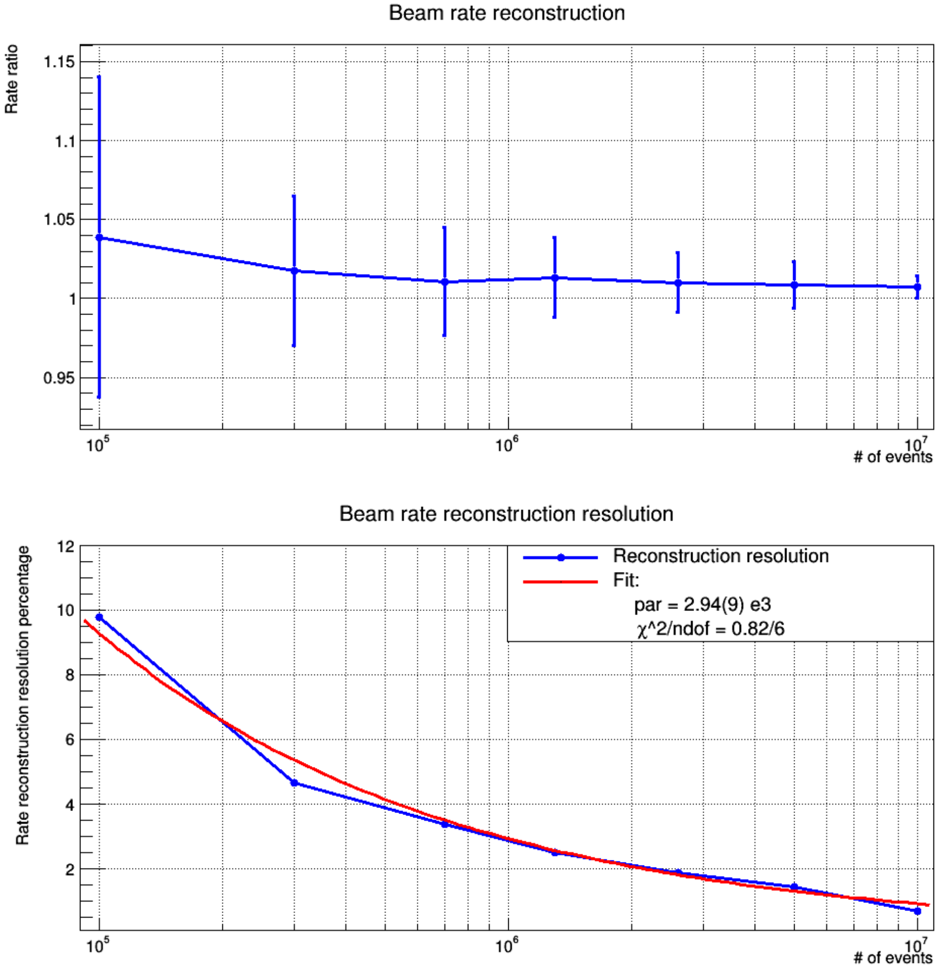

Figure 4.28: *Rate reconstruction resolution as a function of number of events generated. The fitting function in the plot below is proportional to 1/$\sqrt{N}$. The threshold is constant for all the samples: 20 a.u..*

10^7 events are sufficient to obtain a resolution on rate reconstruction better than percent. The muon beams at PSI have a rate of the order of 10^8, so a few seconds are more than enough to reach such a resolution.
In the next paragraphs all the simulated beam rates will be 10^7 particles/s.

Effect of mask on rate measurements

On summer 2019 we built the first complete MatriX prototype. It is shown in Fig.4.1. The final version of MatriX will have the crystals fixed on the SiPMs using the optical cement (BC-600 from Saint Gobain[48]). Currently the crystals are maintained in position only by the plastic mask, and they are coupled to the SiPMs through optical grease[35]. In order to evaluate the effect of the mask on the beam measurements, simulations of MatriX measuring different beams in different conditions have been run: they are collected in Tab. 4.8.

Particle	Initial kinetic energy (momentum) [MeV]	Beam width [mm]	
e^+	52.8	20	8
μ^+	3.7 (28)	20	10
π^-	16.8 (70.5)	8	

Table 4.8: Beam characteristics used in the simulations to evaluate MatriX response.

The positron beam and the muon beam have been ran with two different widths: the 20 mm width is the typical width of the beam at the collimator, while 8-10 mm is the typical width of the beam at COBRA center. During summer 2019 I could only participate to measurements at collimator, so I started with simulations ”at collimator”, but as already mentioned MatriX is designed to measure beams at COBRA center, while measurements at collimator and after the BTS will be performed with SciFi.

All of the simulations have been run with a plastic mask, without a mask and with an aluminum mask. In order to compare the beam reconstruction in the different conditions a focus has been posed only on the rate reconstruction: the size measurements where always consistent with the expected values.

Using the variables *time event* and *track length* the primary particles signals are separated from dark noise events, secondary particles events and afterpulses. From now on these spectra are referred as ”pure”. Fig. 4.29 shows the pure muon spectrum as an example.

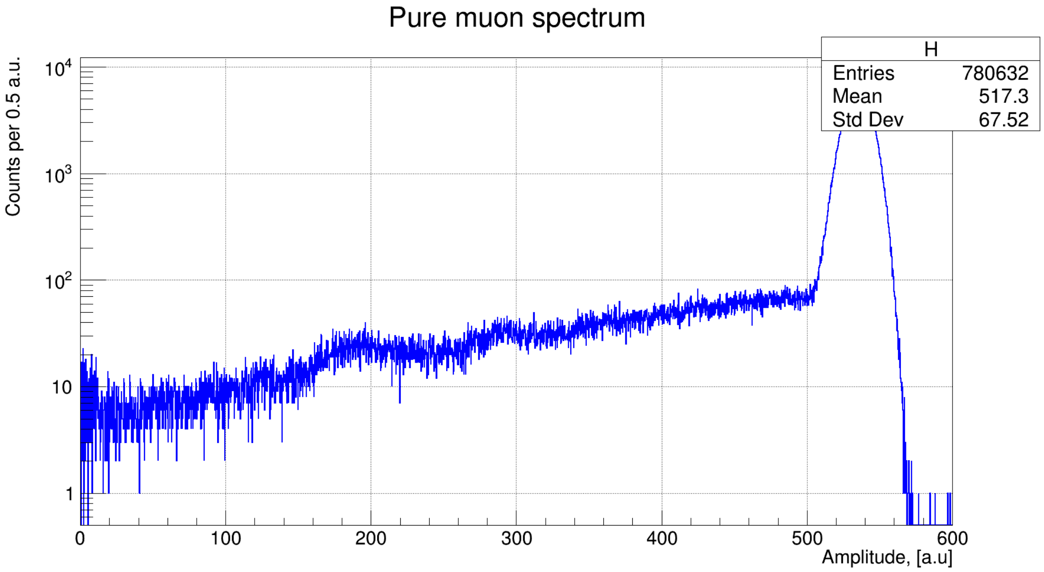

Figure 4.29: *Pure muon spectrum measured without mask. The number of events generated is 10^7.*

Pure spectra are used in order to evaluate the fraction of events lost at different thresholds: a cumulative function of the pure spectra has been built and the beam rate has been evaluated with different thresholds at 5 % bites in fraction of events lost.

To analyse the differences among the considered mask configurations, three quantities have been evaluated as a function of the lost events fraction, that from now on I will refer to as ”cut fraction”:

1. rate loss vs cut fraction: the rate loss is defined as $1 - \frac{R_{rec}}{R_{real}}$, where R_{rec} is the reconstructed rate, while R_{real} is the rate used in the simulations. Here the dependence is expected to be linear, so that if the threshold is such as to cut 5% of the primary particles event, the same value is expected to be lost in rate reconstruction;

2. rate reconstruction corrected vs cut fraction: rate reconstruction corrected is defined as $\frac{R_{rec}}{R_{real}(1-cut\,fraction)}$. Here the graph is expected to be constant;

3. relative resolution on rate reconstruction vs cut fraction.

Fig. 4.30 shows an example: it represents the rate reconstruction done on a 20 mm muon beam with a polyethylene mask on MatriX. The simulation is composed of 10^7 events.

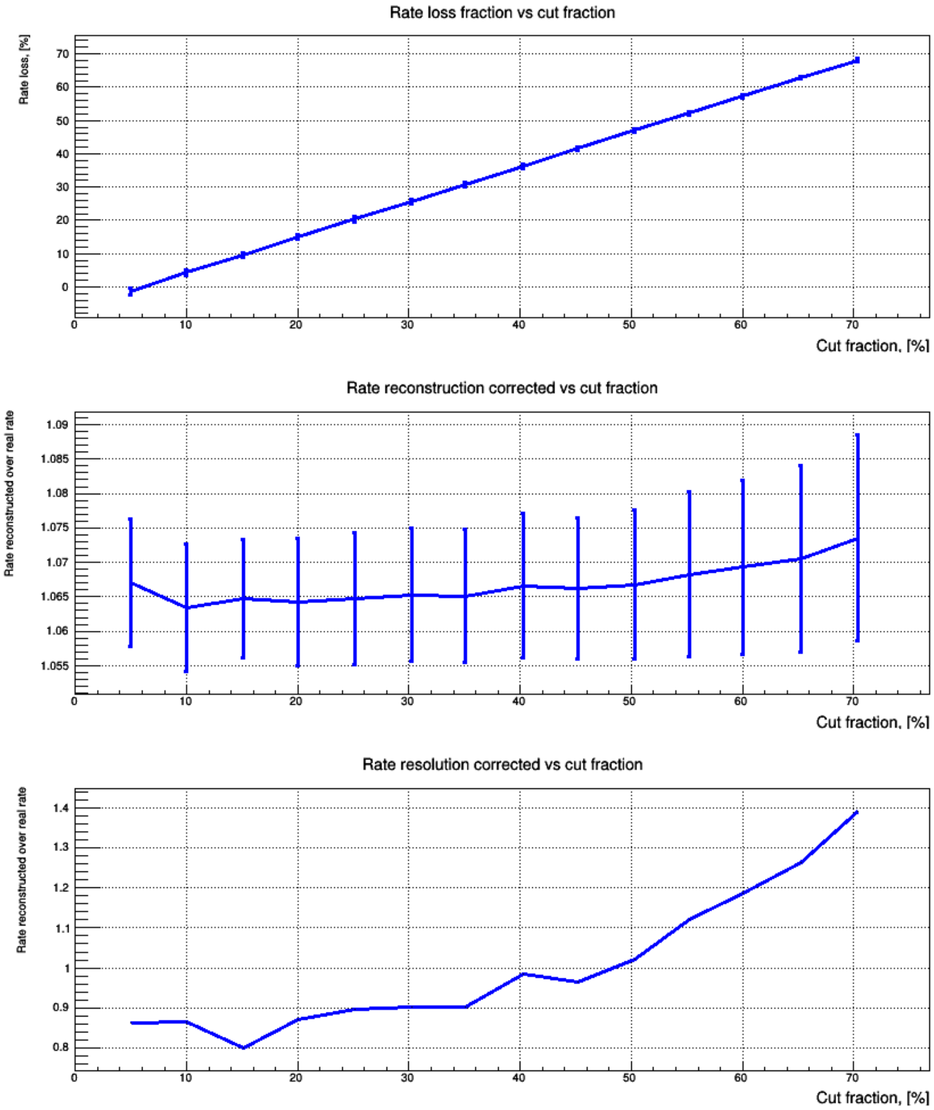

Figure 4.30: *Rate reconstruction of a muon beam. A polyethylene mask is mounted on MatriX. The sample is composed of 10^7 events.*

There is an overestimation of the rate by a $\sim 7\%$ factor: this overestimation is caused by the muons scattered by the mask on the scintillating crystals. This effect results in an increase of the efficient area of the single element that depends on the momentum of the beam particles. Fig. 4.31 and 4.32 show the rate reconstruction performed on a 20 mm positrons beam and on a 8 mm pion beam. The first sample is composed of 10^7 events, while the second one is composed of 10^6 events.

There is an overestimation by a 5% factor reconstructing the positron beam, while the reconstruction is compatible with 1 reconstructing the pion beam, but this could be due to the low statistics.

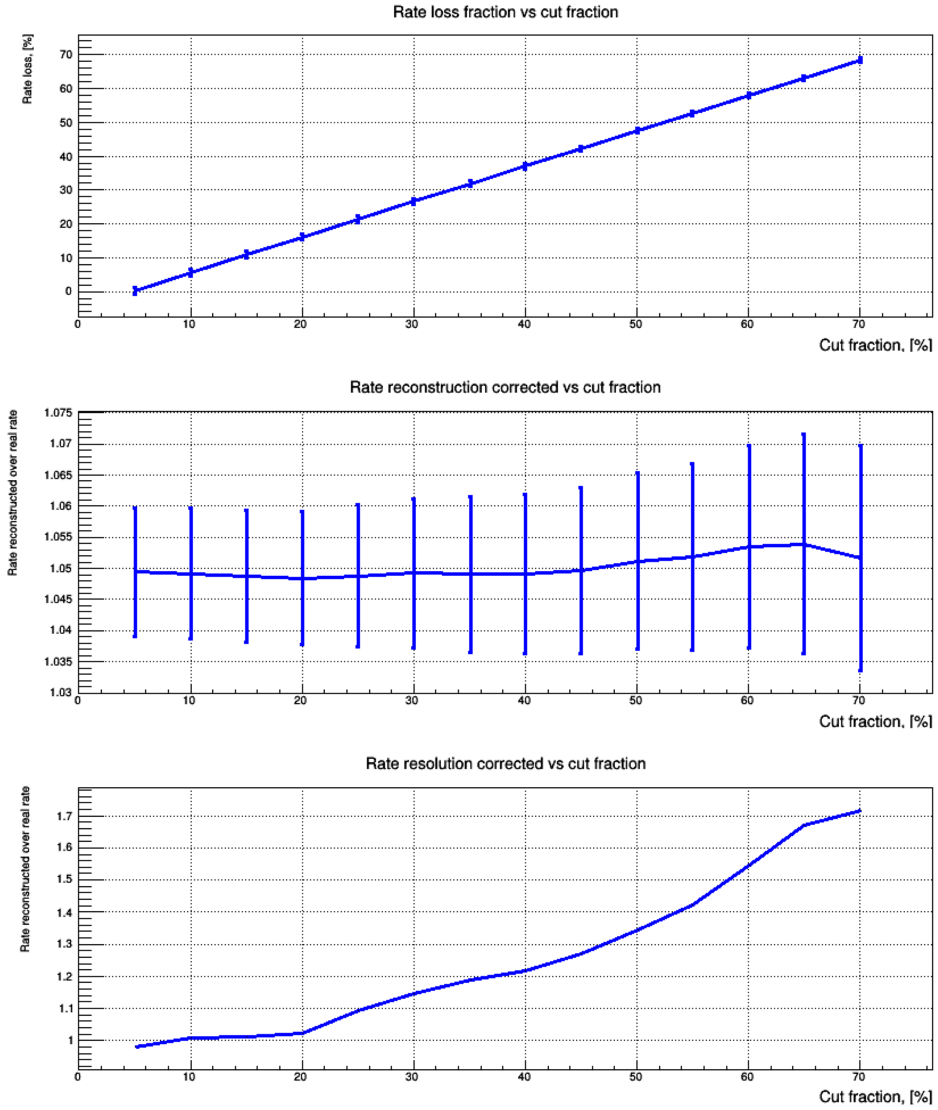

Figure 4.31: *Rate reconstruction of a positron beam. A polyethylene mask is mounted on MatriX. The sample is composed of* 10^7 *events.*

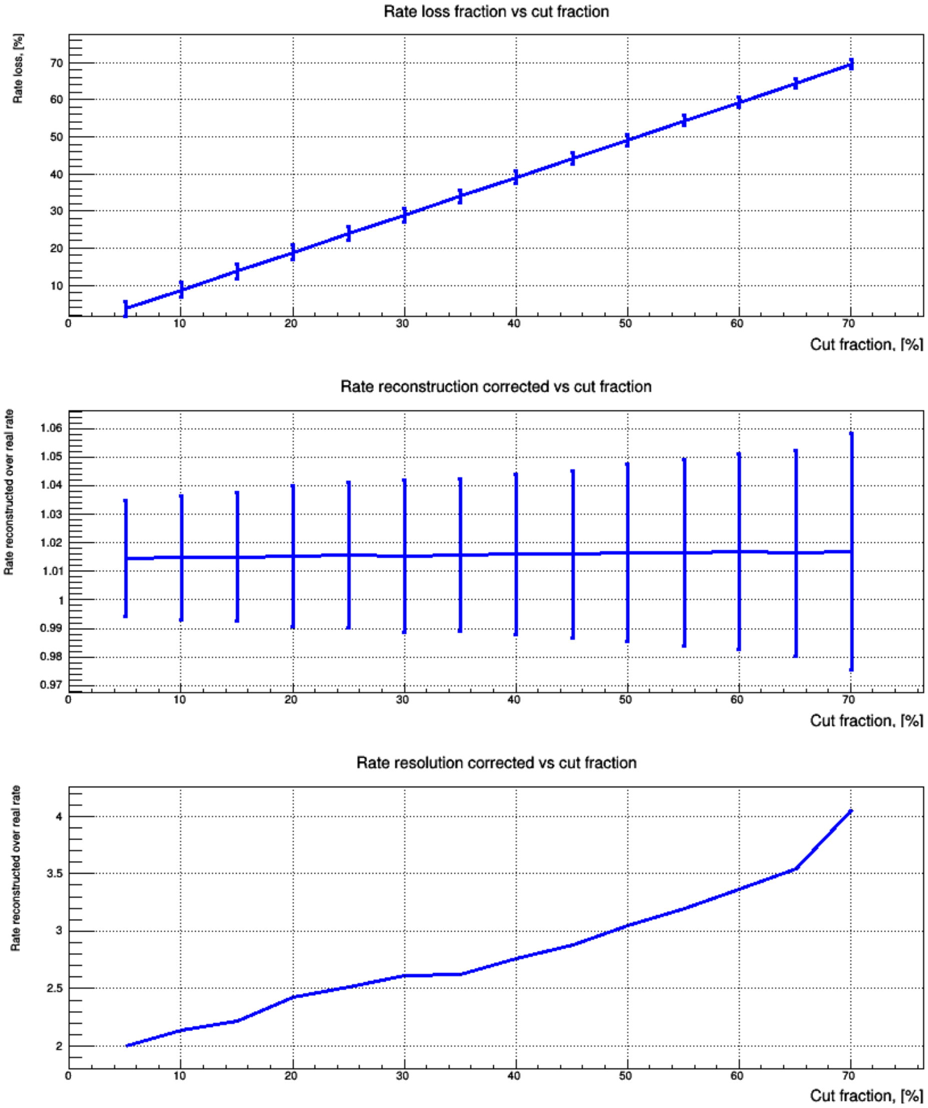

Figure 4.32: *Rate reconstruction of a pion beam. A polyethylene mask is mounted on MatriX. The sample is composed of* 10^6 *events.*

This effect can be avoided by removing the mask. Fig. 4.33, 4.34 and 4.35 show the rate reconstruction performed on the same simulations removing the mask. In these cases the reconstruction is compatible with the real value: there is no cross-talk effect among the elements up to this level. In any case the effect, if present, is lower than the requested resolution ($\lesssim 1\%$).

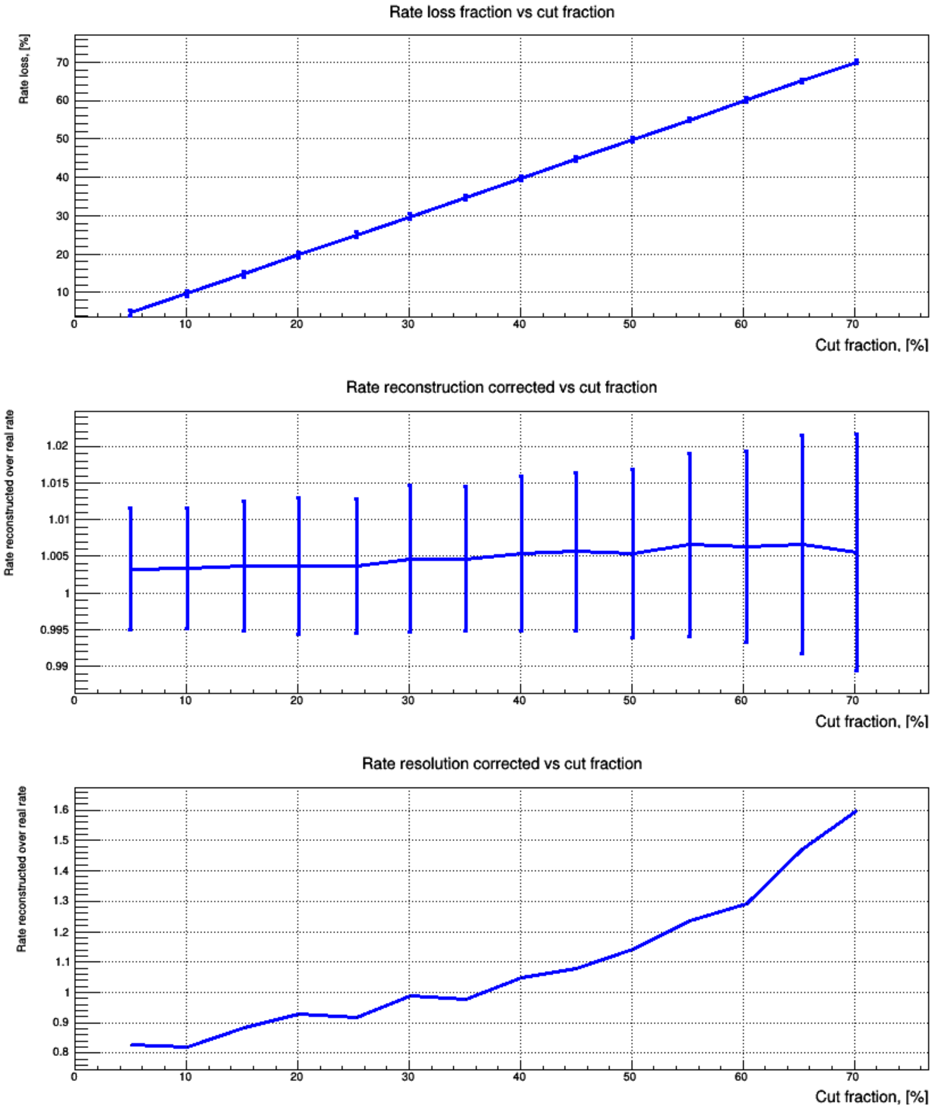
Rate loss fraction vs cut fraction

Rate reconstruction corrected vs cut fraction

Rate resolution corrected vs cut fraction

Figure 4.33: *Rate reconstruction of a muon beam. The detector is without mask. The sample is composed of* 10^7 *events.*

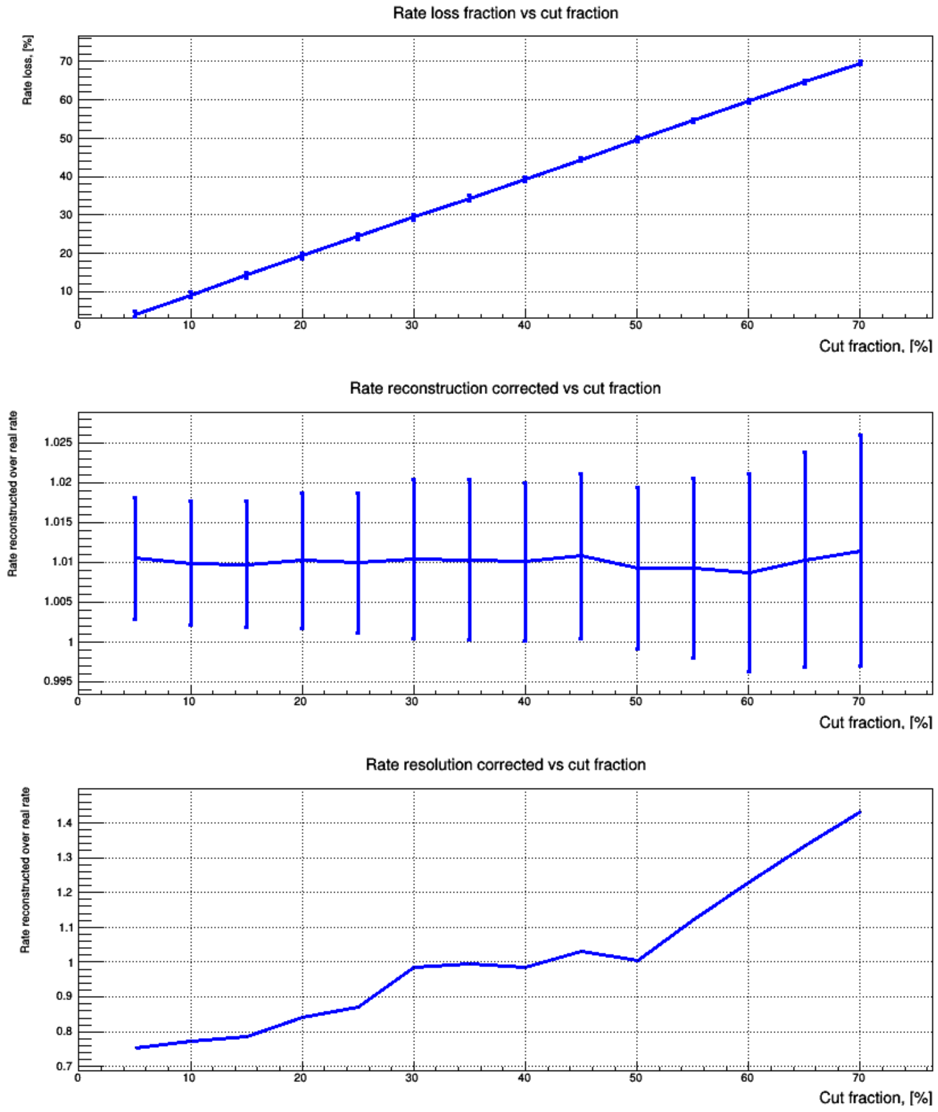

Figure 4.34: *Rate reconstruction of a positron beam. The detector is without mask. The sample is composed of* 10^7 *events.*

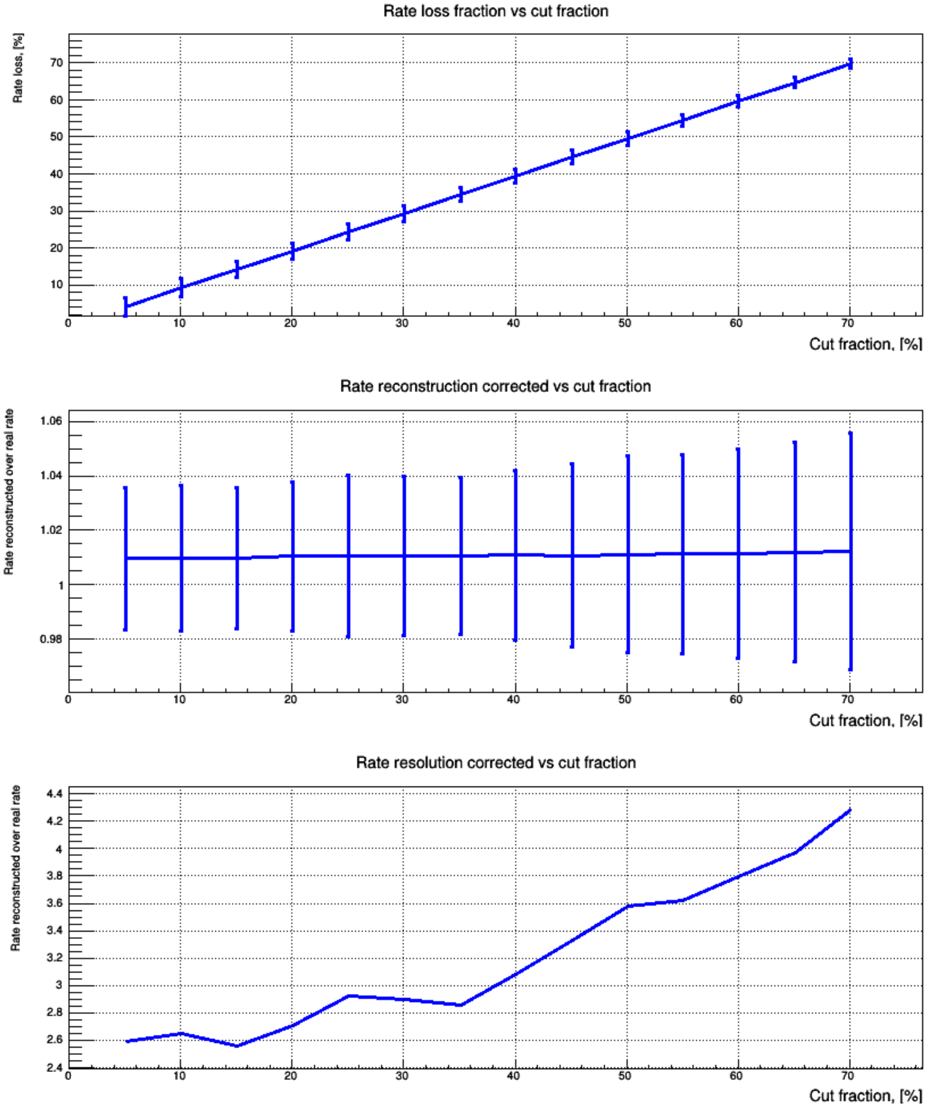

Figure 4.35: *Rate reconstruction of a positron beam. The detector is without mask. The sample is composed of* 10^6 *events.*

The rate reconstruction is consistent using muon and positron beams at COBRA center (10 and 8 mm wide): the reconstruction plot are collected in Ap. D. Given the considerations above, there is no actual gain using a mask on MatriX, and the effect vary with the beam type: unless it's needed for mechanical configuration, the final version of the detector will be without any mask.

4.4.3 Beam reconstruction: skew beam

By design, MatriX is able to measure the correlation between the x and y direction of the beams. Fig. 4.36 shows an example of beam reconstruction performed in presence of correlation. Correlation has been introduced by sampling two uncorrelated gaussian distributions: one with a 15 mm sigma, the other with a 25 mm sigma. Then they are mixed applying a rotation of 45 deg. The number of events simulated is 10^6.
The expected sigmas and correlation factor are collected in Tab. 4.9.

σ_x [mm]	σ_y [mm]	ρ
20.62	20.62	-0.471

Table 4.9: Expected parameters for the correlated beam in Fig. 4.36.

Tab. 4.10 collects the results of the fit.

μ_x [mm]	σ_x [mm]	μ_y [mm]	σ_y [mm]
-0.16 $\pm$ 0.11	20.42 $\pm$ 0.16	0.06 $\pm$ 0.11	20.68 $\pm$ 0.16
A [mm^2]	ρ	χ^2	ndof
(4.04 $\pm$ 0.03) 10^6	-0.473 $\pm$ 0.006	65.7	75

Table 4.10: Fit parameters for correlated beam reconstruction example in Fig. 4.36.

The reconstructed rate is:

$$R = (1.01 \pm 0.03)10^7 \mu/s$$

The fit results are compatible with the expected values.

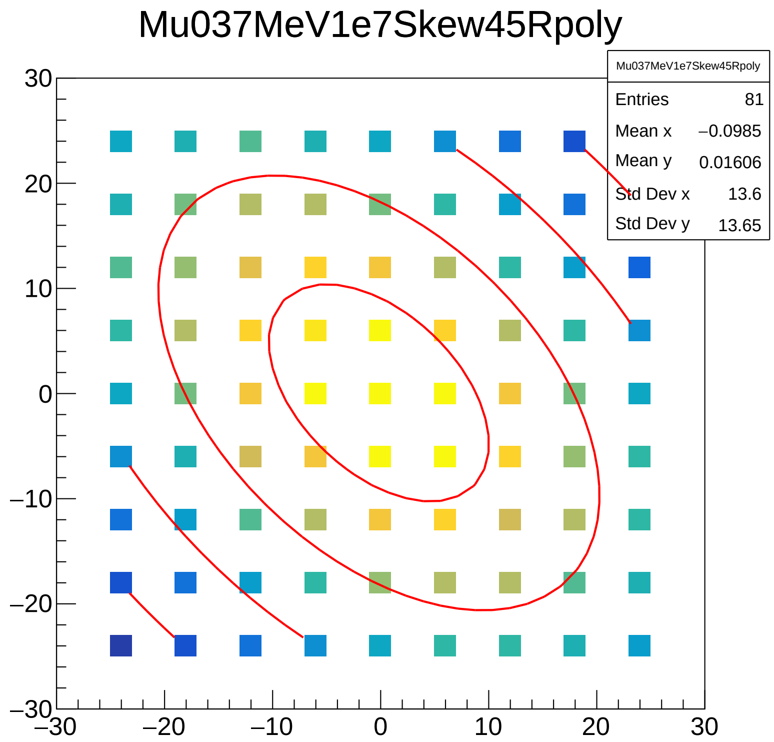

(a) comparison between fit and histogram.

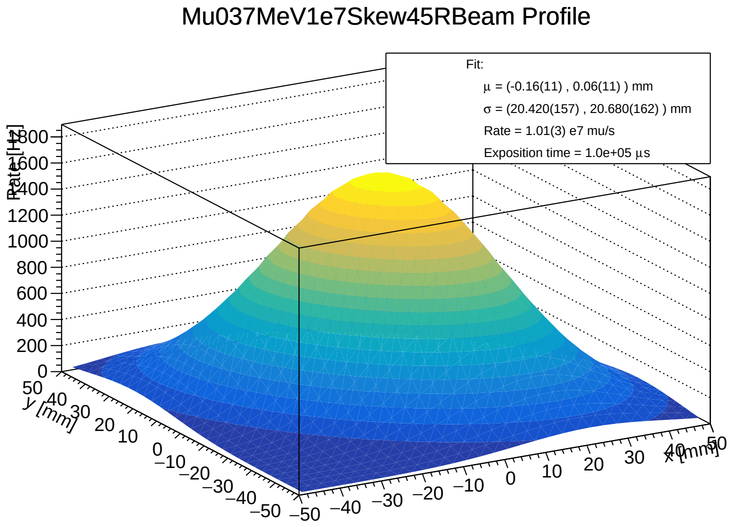

(b) Fitting function profile.

Figure 4.36: *Correlated muon beam reconstruction without the mask. The beam widths and correlation are collected in Tab. 4.9, centered along the detector axis. In this case the beam rate is* 10^7 *μ/s. The threshold chosen is 300 a.u..*

4.5 Degradation of the crystals

In the sections above, only simulations of a ”perfect” detector are reported: even in the single element simulations, the crystals were perfectly aligned with the SiPMs, the elements were perfectly positioned and the surfaces of the crystals were perfectly polished. Actually, MatriX is composed of 81 independent detector that have to be calibrated and inter-calibrated.

Three effects that could introduce a loss in performances are considered:

- *ground*: this effect consists in introducing non-polished surfaces. This is done through the GLISUR model for the optical modeling of surfaces in Geant4[21, 22, 23];
- *shift*: this effect consists in a displacement of the crystal with respect to the center of the SiPMs;
- *tilt*: it consists in an angle between the crystal and the SiPM.

In the next paragraph, a preliminary study on these degrading effects is shown: firstly on the single element; secondly on the complete detector.

4.5.1 Single element simulation

The three effects listed above in the single element simulations have been introduced separately. Fig. 4.37 shows the spectrum of a monochromatic, perfectly aligned along the axis of the SiPM, 28 MeV/c momentum muon beam. Fig. 4.38 shows the same simulations but with a 52.8 MeV kinetic energy positron beam. In the case of the *ground* effect, the percentage values represent the *polish* variable of the GLISUR model[21, 22, 23].

When the crystals are tilted an empty space arises between the crystal and the SiPM: this space is filled with optical grease[35]. It is described as an empty space with a refractive index 1.465.

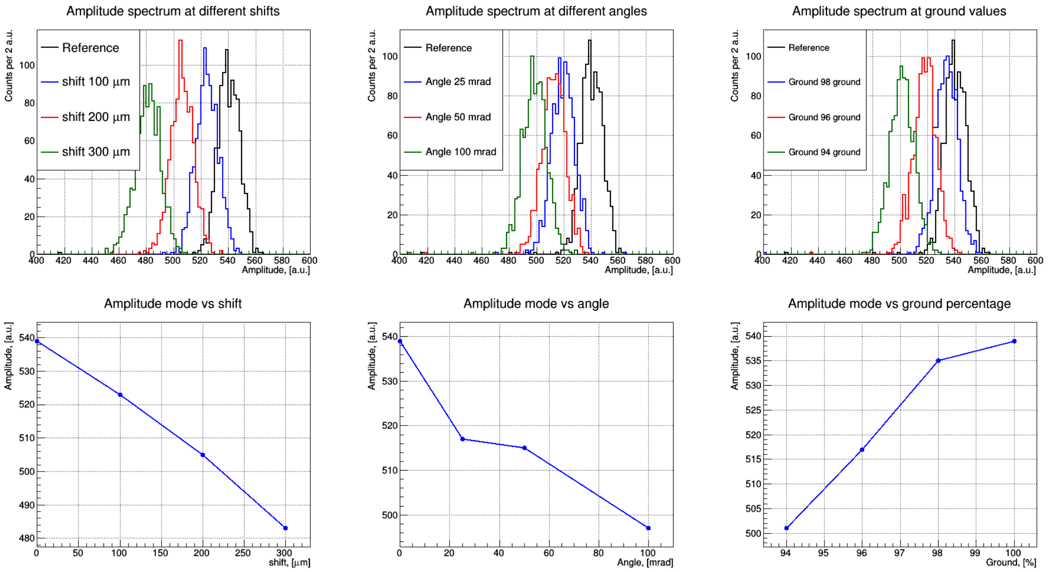

Figure 4.37: *Effect of degrading conditions on the MatriX elements. The beam is a 28 MeV/c momentum muon one, monochromatic, perfectly aligned along the SiPM axis.*

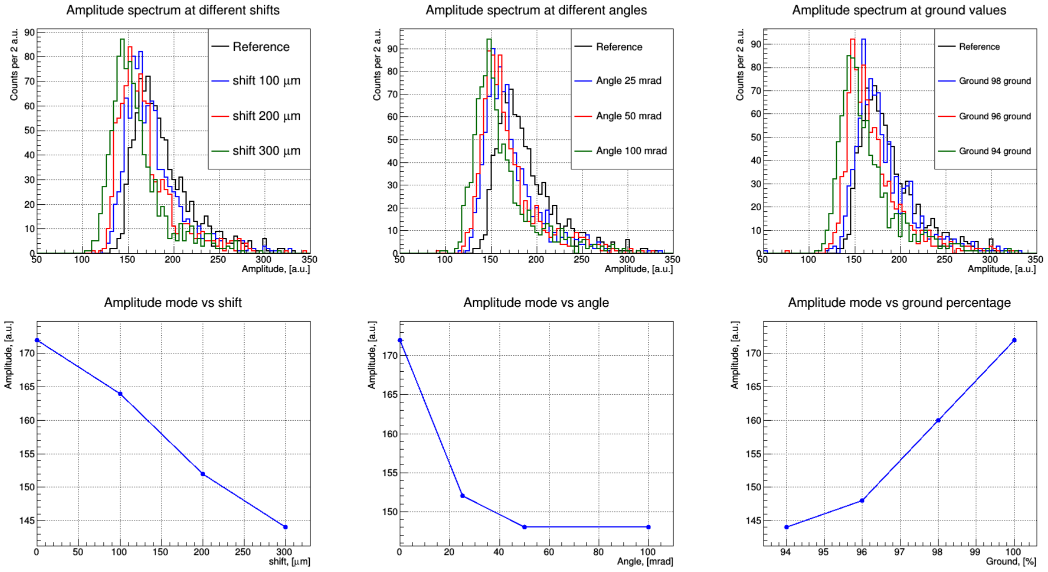

Figure 4.38: *Effect of degrading conditions on the MatriX elements. The beam is a 52.8 MeV kinetic energy positron one, monochromatic, perfectly aligned along the SiPM axis.*

4.5.2 Complete detector simulation

To evaluate the effects of degradation on the complete detector, simulations with mixed degradation effects have been run using:

- 21 perfect elements;
- 20 elements with just one type of degradation. The values used for the effects are: 100 μm *shifts*, all in the same direction; 25 mrad *tilts*; 98% *ground*;
- 20 elements with two types of degradation, rotating among the three shown above;
- 20 elements with all three types of effects.

Fig. 4.39 the comparison between the amplitude distribution by channel of the ”degraded” MatriX and the same amplitude distribution scaled channel by channel by a factor equal to the mode: this way all the channels share the same mode equal to 1. The number of generated events is 10^6, and the beam is 20 mm wide. The beam rate is 10^7 μ/s.

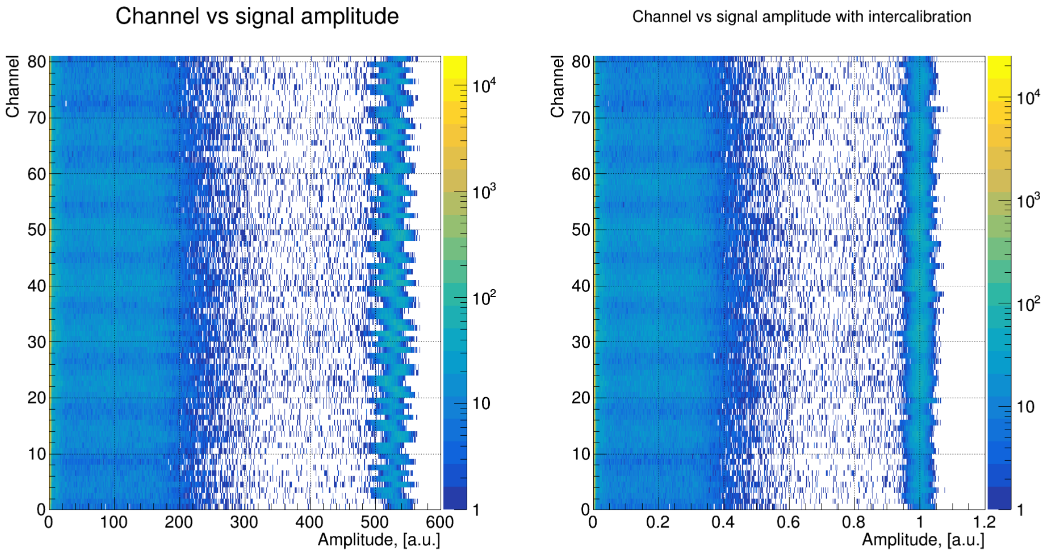

Figure 4.39: *Comparison of the amplitude spectra by channel measured by the ”degraded” MatriX and the same spectra inter-calibrated by scaling channel by channel by a factor equal to the channel amplitude mode.*

Even if it is possible to distinguish the channels clearly because of the different positions of the muon peak, it is clear that a fine tuning on the positioning of the crystals or on their performances is not needed. It must be underlined that the conditions used represent a situation extreme and more similar to the current configuration: a *tilt* of 25 mrad is $\sim$ 1 deg, quite big. Moreover the crystals are produced together and the polishing is expected to be almost the same for all the crystals.

It is sufficient to use one threshold for all the channels in order to obtain a good measurement of the beam properties. Fig. 4.40 shows the reconstruction using a 300 a.u. threshold.

Tab. 4.11 collects the results of the fit.

μ_x [mm]	σ_x [mm]	μ_y [mm]	σ_y [mm]
-0.10 $\pm$ 0.10	20.28 $\pm$ 0.14	-0.02 $\pm$ 0.10	19.98 $\pm$ 0.14

A [mm^2]	ρ	χ^2	ndof
(4.02 $\pm$ 0.02) 10^6	0.025 $\pm$ 0.007	60.7	75

Table 4.11: Fit parameters for beam reconstruction with ”degraded” MatriX example in Fig. 4.40.

The reconstructed rate is:

$$R = (1.00 \pm 0.02)10^7 \mu/s$$

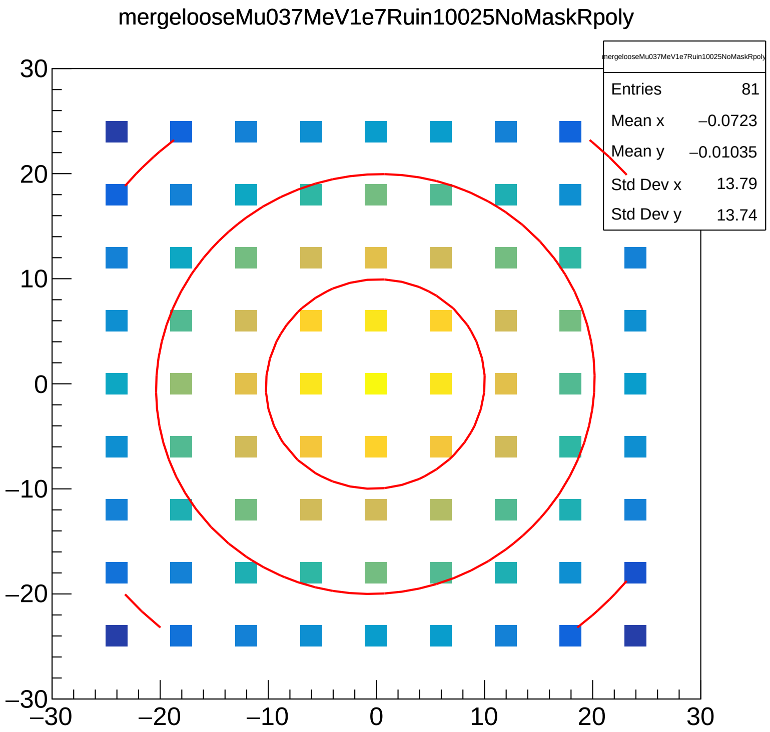

(a) comparison between fit and histogram.

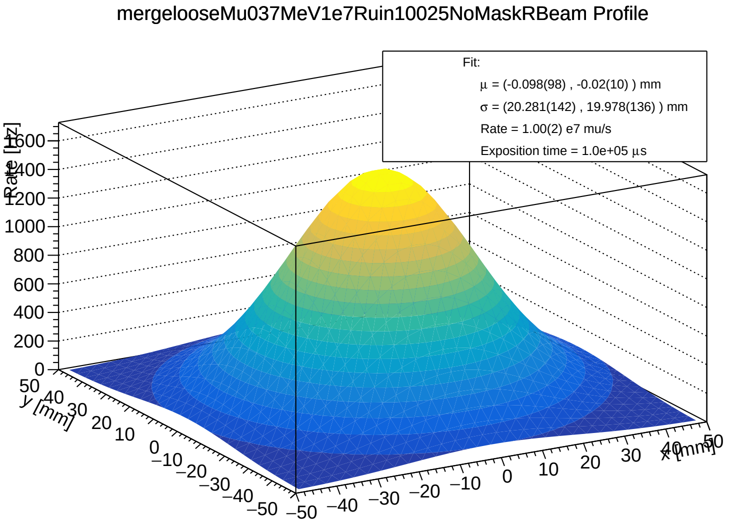

(b) Fitting function profile.

Figure 4.40: *Beam measured with ”degraded” MatriX. MatriX is without mask. The beam is 20 mm wide in both direction, centered along the detector axis. The beam rate is* 10^7 μ*/s. The threshold is 300 a.u.*

4.6 First proof of principle

During summer 2019 I spent two months at PSI laboratories as a summer student. During the summer program I could participate to the first tests of the MatriX detector. Fig. 4.41 shows the first measurement with MatriX on the ΠE5 muon beam, while positioned at collimator. The measurement was taken on September the 18^{th}. Due to the absence of a trigger for the MatriX detector, we used the scalers measured by the WDBs: the rates at which each connected channel passes over threshold. The beam profile and rate turned out to be consistent with what measured by another independent detector.

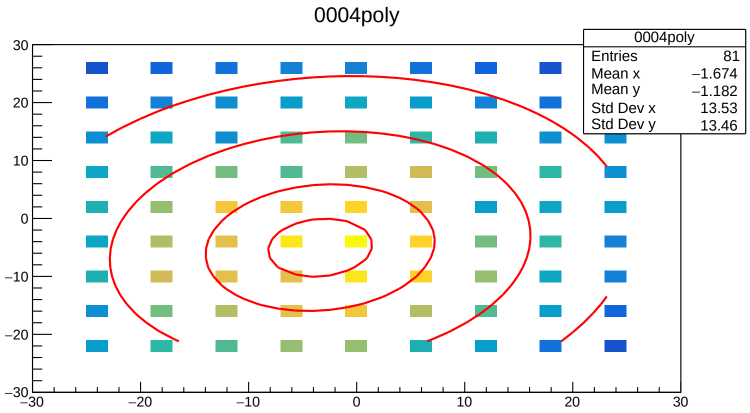

(a) comparison between fit and histogram.

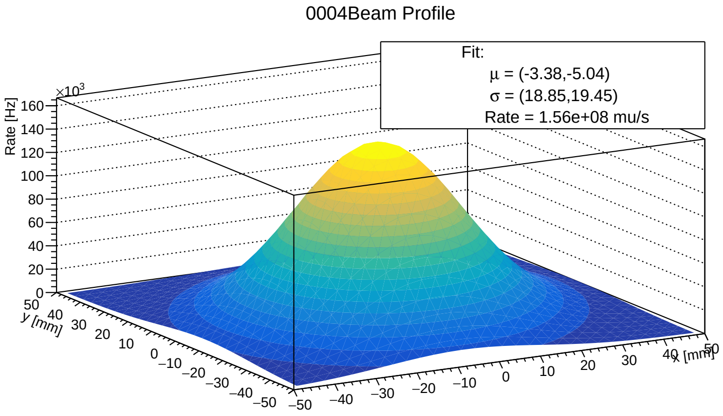

(b) Fitting function profile.

Figure 4.41: *First beam measurement performed with MatriX prototype on the ΠE5 muon beam at PSI laboratories. data taken on September 18^{th}, 2019.*

Chapter 5

Calibration tool: Liquid Hydrogen target

There are many methods and instruments developed for calibrating the MEGII apparatus. Several are dedicated to the LXe calorimeter. One crucial thing to be done, to check the functioning and the performances of a detector, is to have a data-driven check on the performances of the detector and a data-driven analysis near the signal region. In the case of the LXe calorimeter, an important calibration method is the Charge EXchange reaction (CEX) p(π^-, π^0)n[5]: the π^0 decays in two γ with energies uniformly distributed between 54.9 and 82.8 MeV. Cutting on the angle between the two photons it is possible to select energies near the signal region ($\sim$ 52.8 MeV).

In the following sections the basic principles involved will be briefly exposed as well as the first considerations arising from a simple Monte Carlo simulation of the apparatus. The first aim of this chapter is to point out the preferable sizing of the new liquid Hydrogen (LH2) target cell, in order to keep the stopping fraction of π^- over an 80$\%$ level. The performances of a possible CH2 substitute will also be discussed.

Fig. 5.1 shows the new LH2 target cell design.

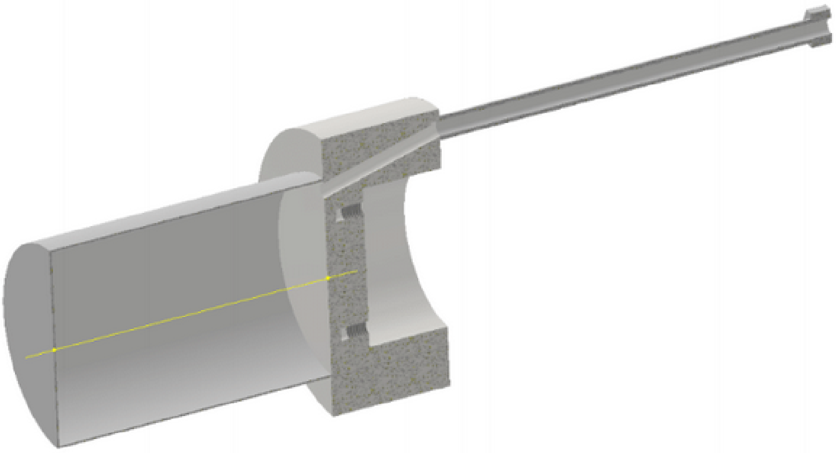

Figure 5.1: *New LH2 target cell.*

5.1 Basic principles: the charge exchange reaction

The CEX reaction is a useful process, which takes a very important role in the MEGII experiment. Pions are produced by the protons impinging on the target E (see Ch. 2). The pions are collected along the ΠE5 beam line setting a momentum of 70.5 MeV/c with a $\sim 3\%$ HWHM. Then the π^- are captured by protons at rest. When the pion is at rest, there are two possible capture reactions:

- CEX: $\pi^- + p \rightarrow \pi^0 + n$
- Radiative Capture (RC): $\pi^- + p \rightarrow \gamma + n$ (used for LXe calibration in the high energy region, E_γ ~129 MeV)

The relative probability for these two process to happen is called Panofsky ratio, and its value is[49]:

$$P = \frac{\Gamma(\pi^- + p \rightarrow \pi^0 + n)}{\Gamma(\pi^- + p \rightarrow \gamma + n)} = 1.533 \pm 0.021 \tag{5.1}$$

Considering the proton and the pion to be at rest, after CEX reaction, the boost of the π^0 is $\beta_{\pi^0} \simeq 0.2$. Then the π^0 decays in two γ: in the π^0 center of mass system (CM) the energy of the two γ is monochromatic and equal to $m_{\pi^0}/2$ = 67.5 MeV, and they are produced back to back uniformly distributed in the solid angle. In the laboratory system (LAB), the energies of the two photons are uniformly distributed between a minimum (E_{min}) and a maximum energy (E_{max}):

$$E_{min} = \gamma \frac{m_{\pi^0}}{2}(1 - \beta_{\pi^0}) = 54.9 MeV \tag{5.2}$$

$$E_{max} = \gamma \frac{m_{\pi^0}}{2}(1 + \beta_{\pi^0}) = 82.9 MeV \tag{5.3}$$

Cutting on the relative angle $\Delta\Theta_{\gamma\gamma}$ between the two photons, it is possible to select photons in the near-signal region: cutting $\Delta\Theta_{\gamma\gamma} < 5$ deg results in an energy bite $\Delta E/E < 1\%$[50].

5.2 The new LH2 target cell

With respect to the old version of the LH2 target, the new one consists in a thicker stainless steel wall and in the use of stainless steel window for the front panel of the cell.

The old version consisted in a stainless steel cylinder, with 0.25 mm thick walls, with a 175 μm mylar window in the upstream direction (front window), using degraders placed before of the target.

The new walls are 0.5 mm thick, and the mylar window is substituted with a stainless steel window playing the role of degrader as well. In the following paragraphs The results obtained simulating the target with different sizes are shown. The specifications of the current project version are collected in Tab. 5.1.

length [mm]	inner radius [mm]	cell front window thickness [mm]	entrance window thickness [mm]
69.5	24.5	0.5	0.5

Table 5.1: New LH2 target cell sizes.

The simulation is Geant4 based and the materials used are taken from the Geant4 material database[51].

Fig. 5.2 shows the simulated LH2 target.

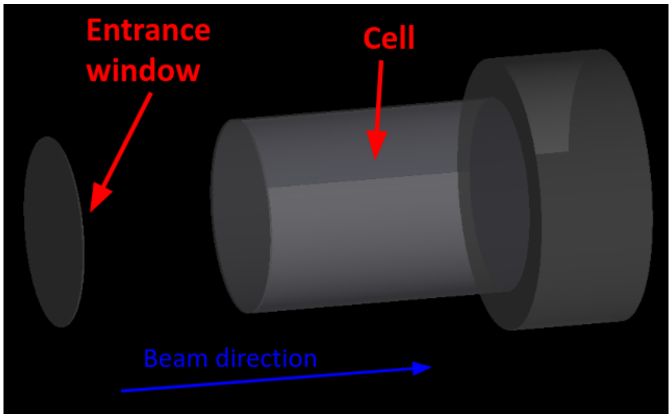

Figure 5.2: *Simulated LH2 target cell view.*

5.2.1 Interacting pion fraction

The fraction of pions captured in hydrogen dependence on the cell inner radius are evaluated, maintaining fixed the other values reported in Tab. 5.1. The pion beam used is generated along the target axis, with no divergence and a sigma equal to 8 mm. The energy of the generated π^- is 70.5 MeV. Fig. 5.3 shows the results of the simulation. Each point is evaluated using samples of 10^5 events.

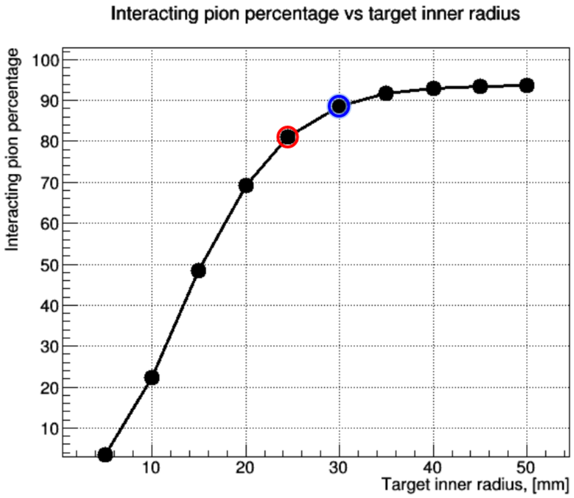

Figure 5.3: *Fraction of pions captured in hydrogen vs the cell inner radius. The error on each point is negligible and can not be appreciated by the plot. The red circle indicates the configuration of the current project. The blue circle indicates a possible alternative. Using a 30 mm inner radius cell would lead to a 89 % capture fraction, near the value of the plateau on the left.*

The highlighted values represent the current project configuration (red, see Tab. 5.1) and a possible alternative (blue). The first configuration leads to a fraction equal to 81.12 ± 0.12 %, while the second one would lead to a fraction equal to 88.65 ± 0.10 %.

5.2.2 Pion range and thickness of the windows

In order to calibrate the LXe calorimeter, another detector is necessary: both of the γ coming from π^0 decay have to be measured, in order to identify the near-signal region (54.9 MeV). The experimental set-up consists of the LH2 target, the LXe calorimeter and an NaI tagging detector: combining the measurements of the NaI tagging detector and of the LXe calorimeter, it is possible to measure the angle between the two γ. Further details are summarized in [50].

It is important to know the position of the decay vertex in order to reconstruct the trajectories of the two γ. Fig. 5.4 shows the range of the π^- beam inside the target as obtained from simulation. The set-up is the same resumed in Tab. 5.1 and the number of generated events is 10^5. The front of the cell is positioned at 0 mm, while the back is at 70 mm.

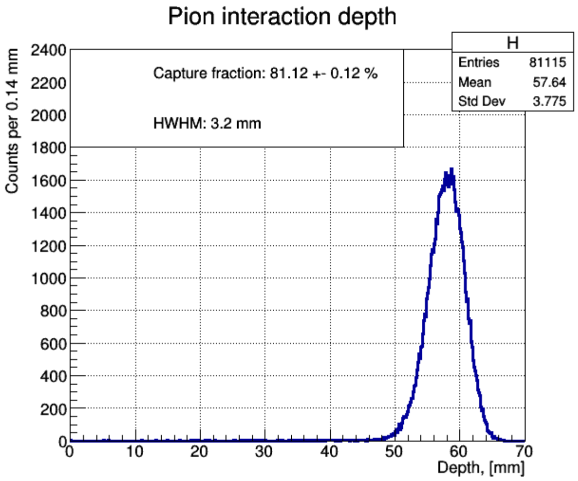

Figure 5.4: *Range of 70.5 MeV/c momentum π^- inside the LH2 target. The stainless steel entrance window is 0.5 mm thick. The stainless steel front panel of the LH2 target cell is 0.5 mm thick.*

Fig. 5.5 shows the range distribution of the π^- beam in different configurations: varying the thickness of the entrance window (1.0 or 2.0 mm), and varying the front plate thickness (1.0 or 2.0 mm). As expected, the distribution remains the same for the same total stainless steel thickness, the only change is the number of events registered: more material results in a higher Multiple Scattering deviation, meaning that it is preferable to increase the amount of material in a region near to the LH2. In fact, the increase of thickness of the entrance window leads to a decrease in the capture fraction.

Moreover it is preferable to make the two γ pass through the minimum amount of matter. This means that a configuration in which the peak of the range distribution is far from the rear part of the cell, where the cell is soldered to a 3.5 cm radius 5 cm thick copper cylinder, is preferable.

The best configuration, fixing the inner radius of the cell at 24.5 mm, would be with a 0.5 mm thick entrance window and a 1.0 mm thick front panel.

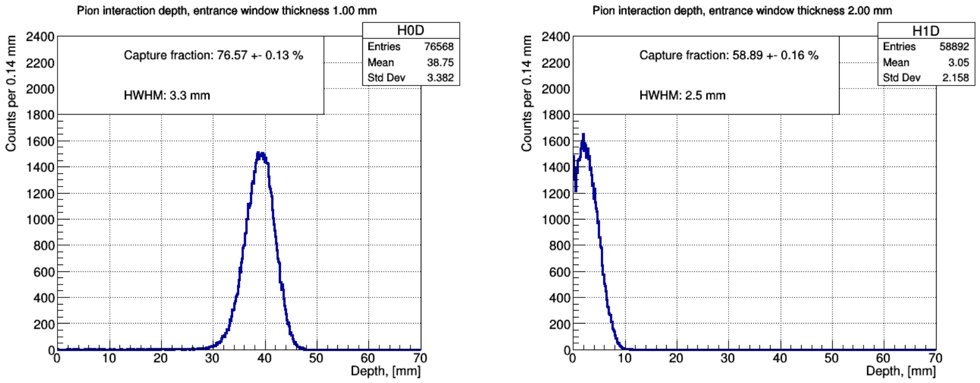

(a) 1.0 mm thick entrance window

(b) 2.0 mm thick entrance window

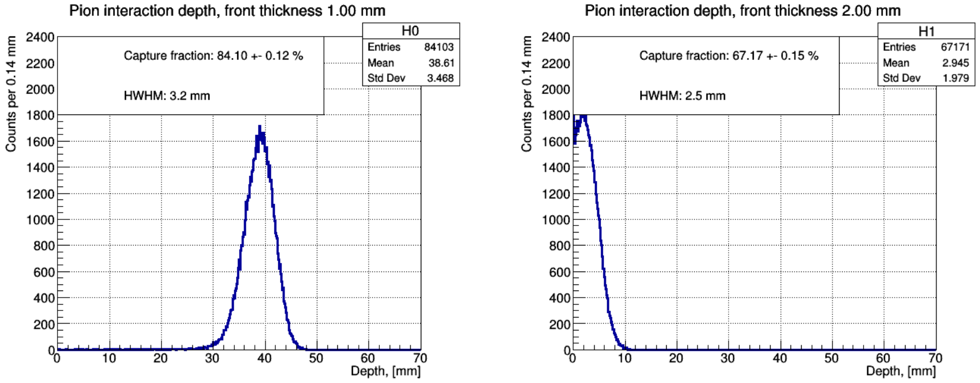

(c) 1.0 mm thick front panel

(d) 2.0 mm thick front panel

Figure 5.5: *Pion range distribution in different set-up. The inner radius of the cell is 24.5 mm and the number of generated events is* 10^5 *in each sample.*

Fig. 5.6 shows the range distribution using the specifications in Tab. 5.2.

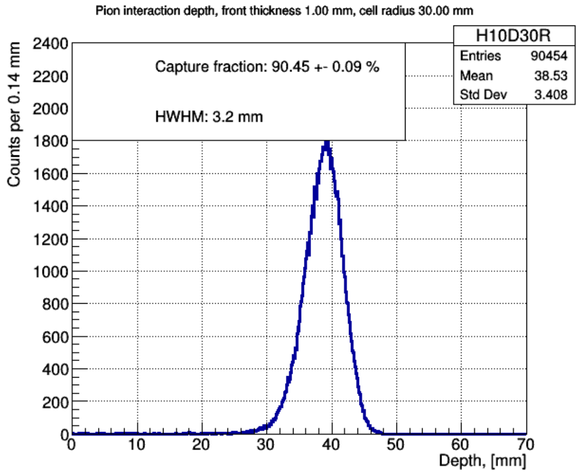

Figure 5.6: *Pion range distribution using Tab. 5.2 set-up. The number of generated events is 10^5.*

length [mm]	inner radius [mm]	cell front window thickness [mm]	entrance window thickness [mm]
69.5	29.5	1.0	0.5

Table 5.2: New LH2 target cell sizes.

In conclusion, the best configuration would be the one in Tab. 5.2: it is the configuration with the higher capture fraction, the decay vertex is far from the rear of the cell and the peak of the distribution is well localized (HWHM = 3.2 mm). Of course further simulations and measurements are needed to confirm this statement. A precautionary measure in this sense would be to produce two cells with 0.5 mm walls and entrance windows: one with a 24.5 mm radius and one with 29.5 mm radius. Than an 0.5 mm thick stainless steel panel could be designed to fit the front part of the cell, in order to increase the amount of stainless steel before the LH2 target if needed.

5.2.3 CH2 version

A simulation substituting the whole target with a 16.5 mm thick, 25 mm radius polyethylene cylinder has been run. The beam has the same specifications as in the previous paragraphs. The material used is taken from the Geant4 material database[51]. The Fig. 5.7 shows the range inside the CH2 target for the captured pions.

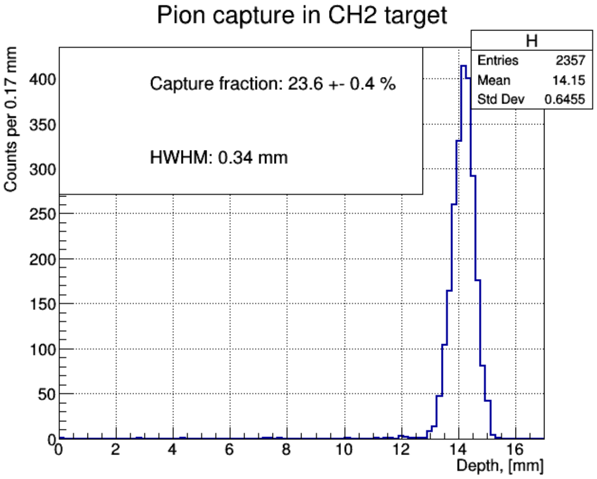

Figure 5.7: *Pion range distribution using inside CH2. The number of generated events is* 10^4.

There is a high gain in terms of vertex position resolution (0.34 mm, an order of magnitude smaller) and in terms of measurement feasibility: it only necessitates a support, but no cryogenic circuit is needed. The only drawback is a drop in pion capture rate by a factor $\sim$ 3-4: the capture fraction is 23.6 $\pm$ 0.4%. This would currently translate in longer data-taking period used for calibrations. While during pre-eng runs and commissioning periods there are not stringent requirements on the DAQ, during physics runs short and fast calibration method solutions are preferred.

Conclusions

The work presented in this thesis is focused on the design, construction, test of two new beam monitoring devices that will be used for the MEGII experiment, SciFi and MatriX, including their detailed MC simulation implementation for a full understanding of the involved processes and possible optimization. Furthermore the design of the new Liquid Hydrogen target has been studied, supported by dedicated MC simulations. The main results, regarding the beam monitors, can be summarised as follows:

1. the SciFi detector has been successfully tested and used extensively along all the PSI beam line. The beam characteristics and rate turned out to be consistent at the level of few percentages with a reference one;
2. the MatriX detector has been assembled and tested for the first time in ΠE5. The measurements have been performed at the collimator and at the COBRA center;
3. some upgrades from hardware side (the WaveDream) will be implemented for the pre-eng 2020, allowing for an higher current and online rate information;
4. MC simulations suggest that correlation measurements can be performed by SciFi using coincidences between fibers on different layers and that a MatriX version without a mask is preferable. For both the detectors, a resolution better than percent is expected to be achievable in a few seconds of beam time and mouns and Michel positrons are expected to be well separated. A data-driven tuning and validation of the simulations is necessary in order to check, and eventually improve, the reliability of the signal waveform shaping and the resulting amplitude spectra estimation;
5. a possible alternative for the MatriX detector components could be the use of 25 μm pitch

SiPMs[34], in order to avoid the non-linearity induced by SiPM saturation. Further studies are needed in order to evaluate the use of LYSO[19] crystals instead of BC-400[38].

Regarding the new Liquid Hydrogen target, the project sizes fit the requested performances: based on the MC simulation, a capture fraction above 80 % can be achieved using a target radius of 29.5 mm for an 89 % capture ratio.
Two major considerations arise:

1. it could be preferable to increase the material budget along the pions path in order to both shift the interaction vertex away from the rear of the target and increase the capture fraction. Adding a 0.5 mm thick stainless steel panel in front of the target, the peak position would be at 3 cm from the rear of the target and the capture ratio would be 90% using a 29.5 mm inner radius target;
2. a possible alternative, that can be considered in special cases, such as pre-eng periods, could be a polyethylene target, leading to an increase in vertex depth resolution from 3 mm (LH2) to 0.3 mm but decreasing the capture ratio to 24 %, extending the measurement duration by a factor 4.

Appendices

Appendix A

Fibers light output

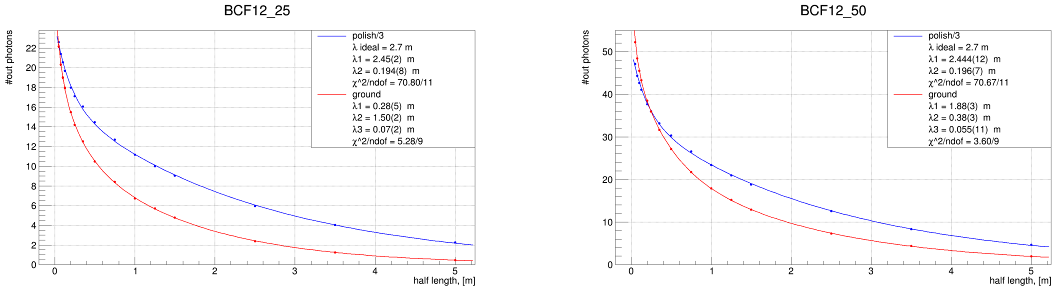

(a) 0.25 mm wide

(b) 0.50 mm wide

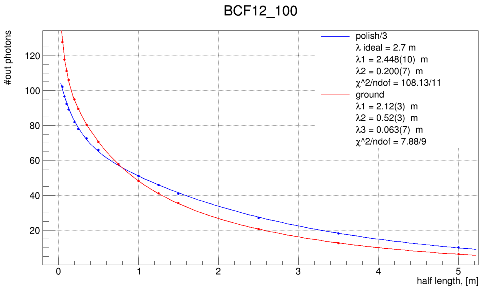

(c) 1.00 mm wide

Figure A.1: *Light output of BCF-12 fibers as a function of fiber length. In blue the values related to the polished version of the fibers, while in red the values related to the non-polished version of the fibers. The blue fitting function is the sum of two exponentials. The red fitting function is the sum of three exponentials.*

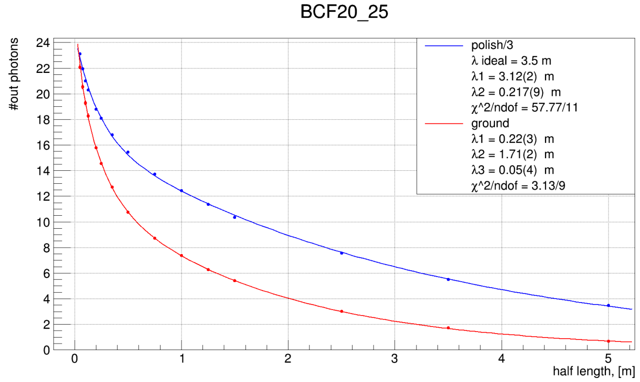

(a) 0.25 mm wide

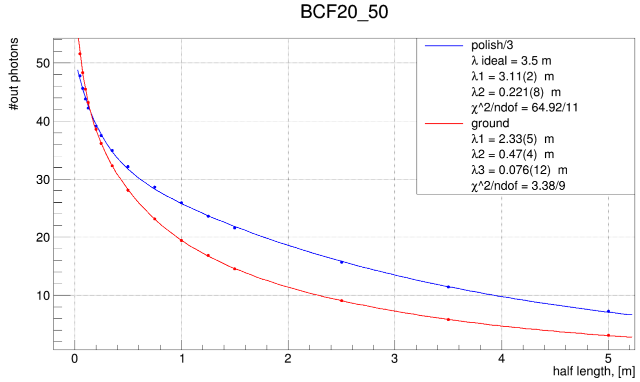

(b) 0.50 mm wide

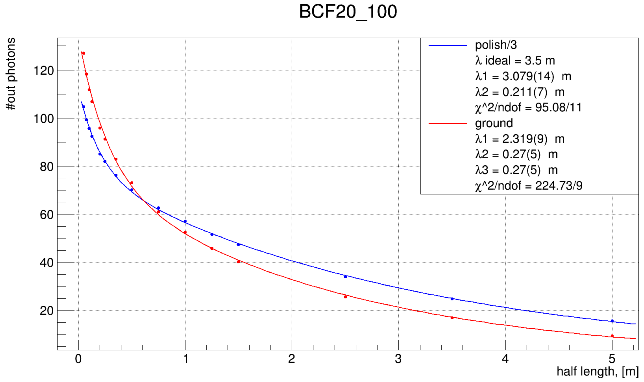

(c) 1.00 mm wide

Figure A.2: *Light output of BCF-20 fibers as a function of fiber length. In blue the values related to the polished version of the fibers, while in red the values related to the non-polished version of the fibers. The blue fitting function is the sum of two exponentials. The red fitting function is the sum of three exponentials.*

Appendix B

MatriX sanity checks

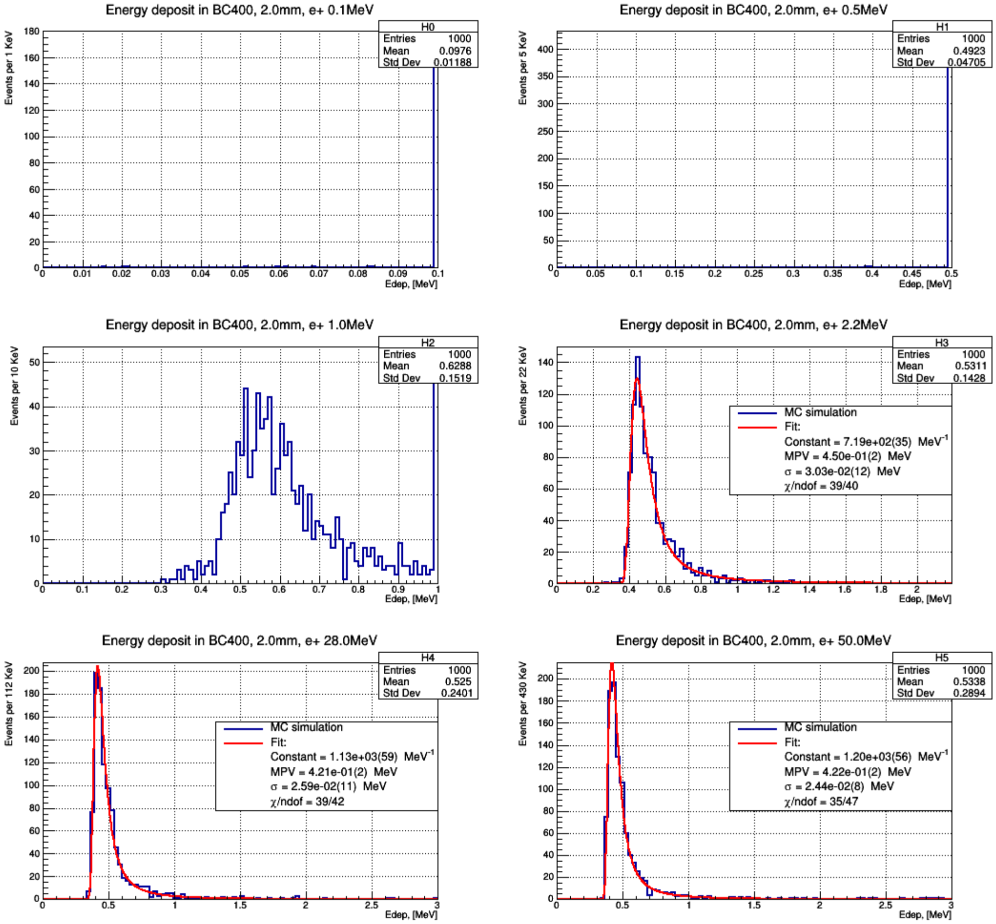

Figure B.1: *Energy deposit in a 2×2×2 mm^3 BC-400 crystal[38] from positrons at different initial kinetic energies. In order from top to bottom, from left to right: 0.1, 0.5, 1, 2.2, 28 and 50 MeV.*

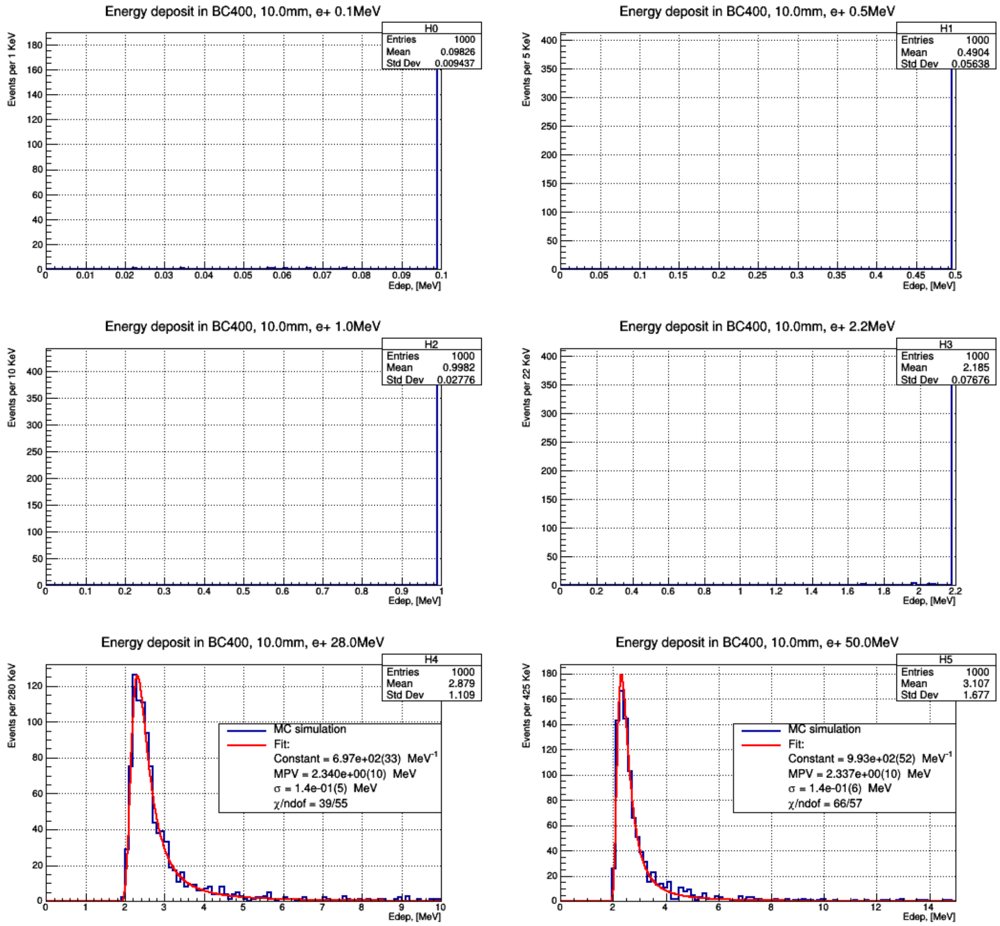

Figure B.2: *Energy deposit in a 10×10×10 mm^3 BC-400 crystal[38] from positrons at different initial kinetic energies. In order from top to bottom, from left to right: 0.1, 0.5, 1, 2.2, 28 and 50 MeV.*

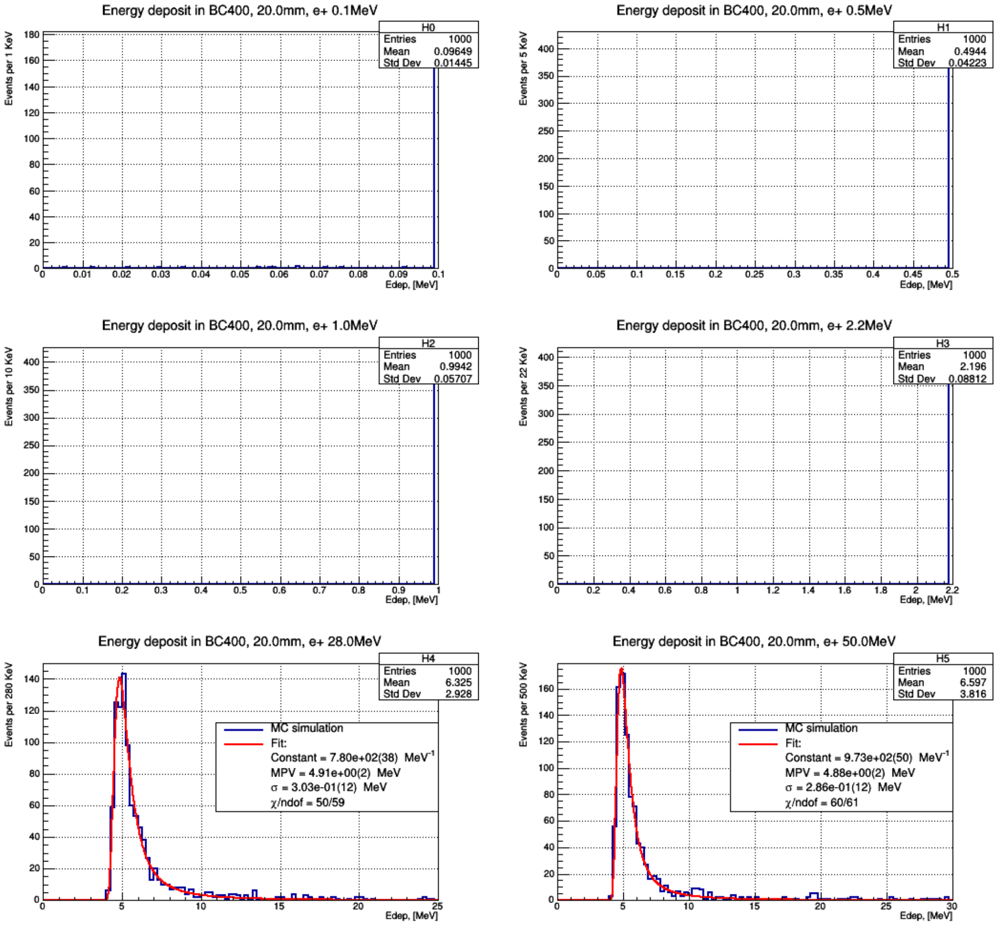

Figure B.3: *Energy deposit in a 20×20×20 mm^3 BC-400 crystal[38] from positrons at different initial kinetic energies. In order from top to bottom, from left to right: 0.1, 0.5, 1, 2.2, 28 and 50 MeV.*

Appendix C

Covariance Matrices of the parameters obtained by fitting number of pixels fired in a SiPM coupled to LYSO crystals

2.2 MeV positrons through LYSO coupled to 50 μm pitch SiPM		
	offset	coefficient
offset	10	-76
coefficient	-76	6.4 10^2

Table C.1: Covariance matrix of the fit reported in Fig.4.19.

2.2 MeV positrons through LYSO coupled to 25 μm pitch SiPM		
	offset	coefficient
offset	5.0	-41
coefficient	-41	3.6 10^2

Table C.2: Covariance matrix of the fit reported in Fig.4.20.

52.8 MeV positrons through LYSO coupled to 50 μm pitch SiPM			
	offset	linear coefficient	quadratic coefficient
offset	10	-78	1.2 10^2
linear coefficient	-78	6.8 10^2	-1.1 10^3
quadratic coefficient	1.2 10^2	-1.1 10^3	1.8 10^3

Table C.3: Covariance matrix of the fit reported in Fig.4.19.

52.8 MeV positrons through LYSO coupled to 25 μm pitch SiPM			
	offset	linear coefficient	quadratic coefficient
offset	5.0	-60	1.2 10^2
linear coefficient	-60	6.7 10^2	-1.4 10^3
quadratic coefficient	1.2 10^2	-1.4 10^3	2.9 10^3

Table C.4: Covariance matrix of the fit reported in Fig.4.20.

Appendix D

Rate reconstruction at COBRA center

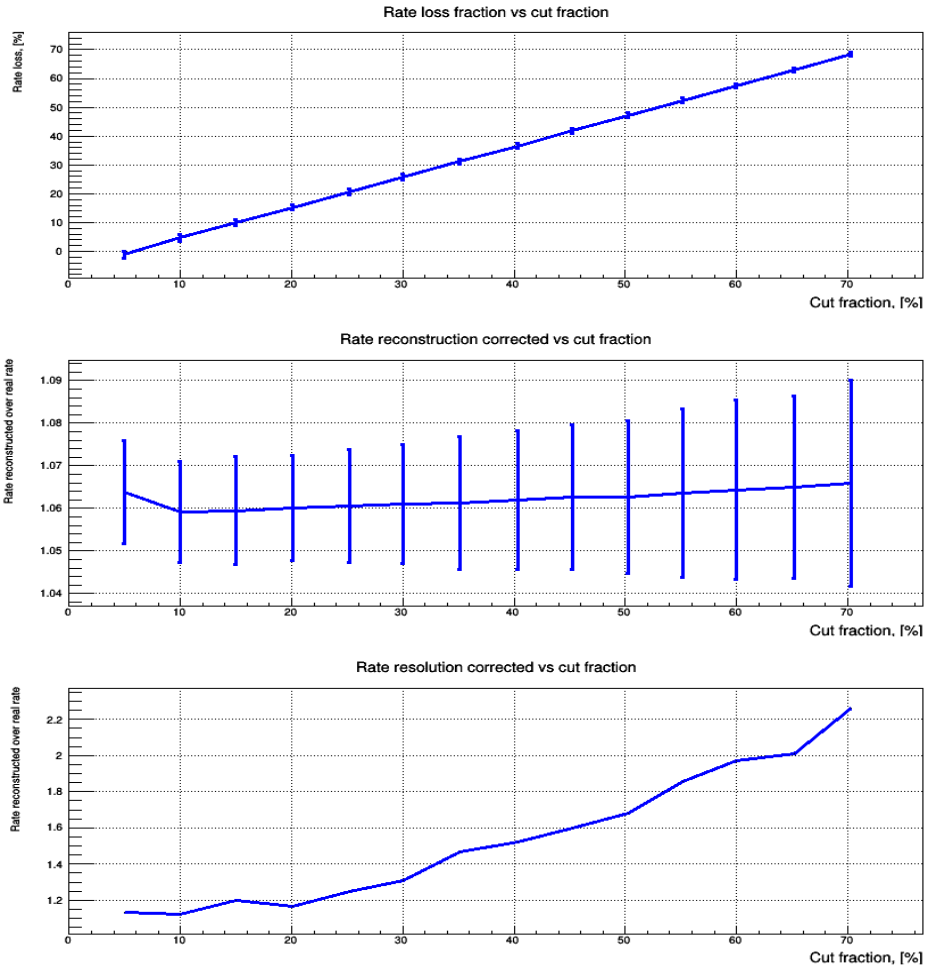

Rate loss fraction vs cut fraction

Rate reconstruction corrected vs cut fraction

Rate resolution corrected vs cut fraction

Figure D.1: *Rate reconstruction of a 10 mm muon beam. A polyethylene mask is mounted on MatriX. The sample is composed of* 10^6 *events.*

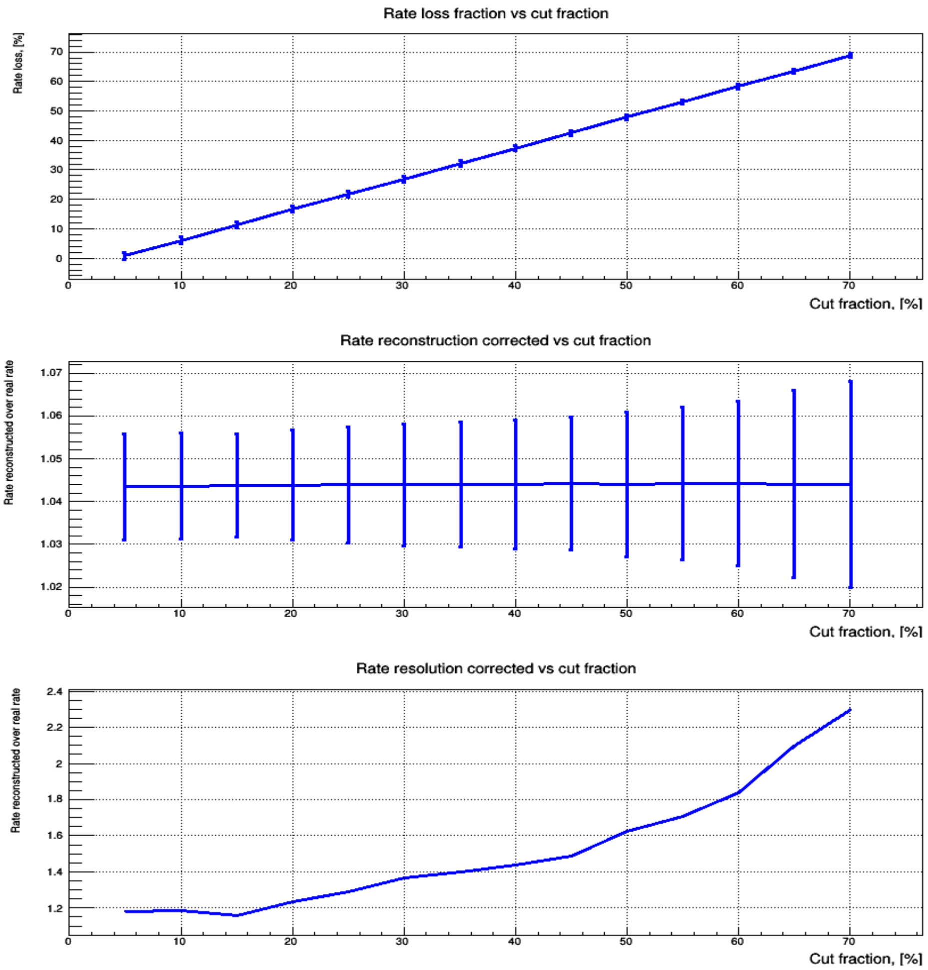

Rate loss fraction vs cut fraction

Rate reconstruction corrected vs cut fraction

Rate resolution corrected vs cut fraction

Figure D.2: *Rate reconstruction of an 8 mm positron beam. A polyethylene mask is mounted on MatriX. The sample is composed of* 10^6 *events.*

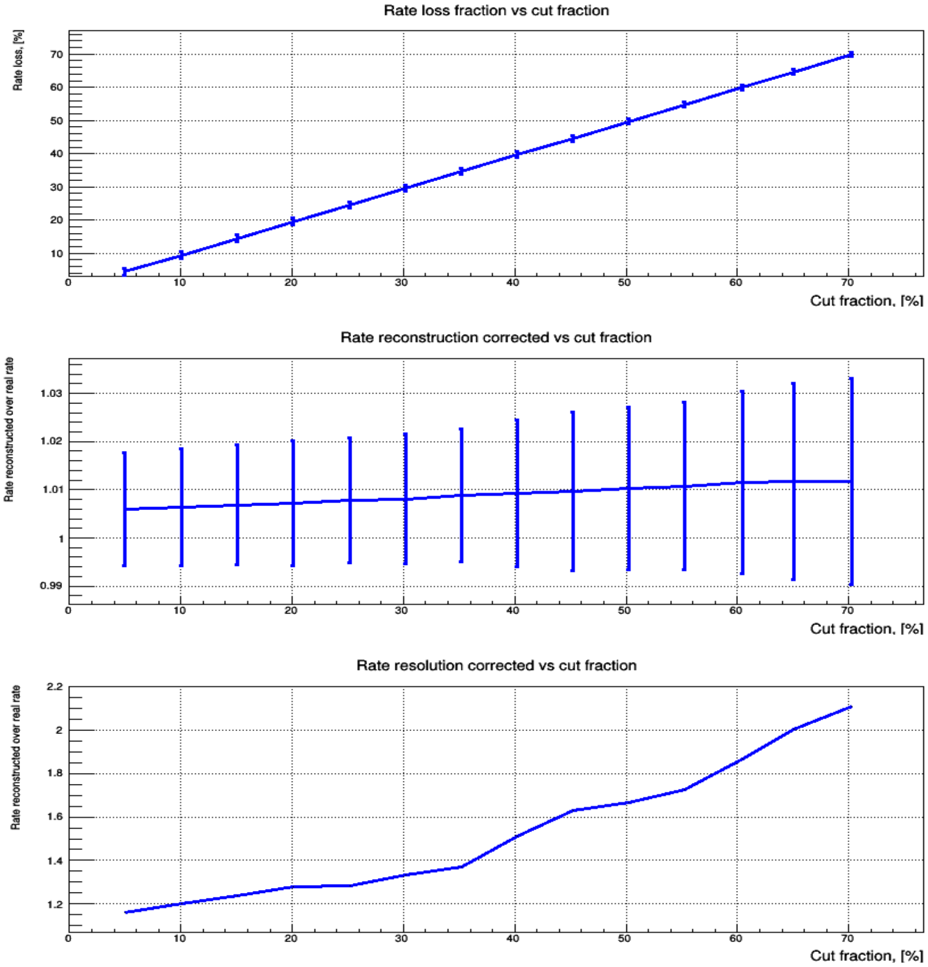

Figure D.3: *Rate reconstruction of a 10 mm muon beam. The detector is without mask. The sample is composed of* 10^6 *events.*

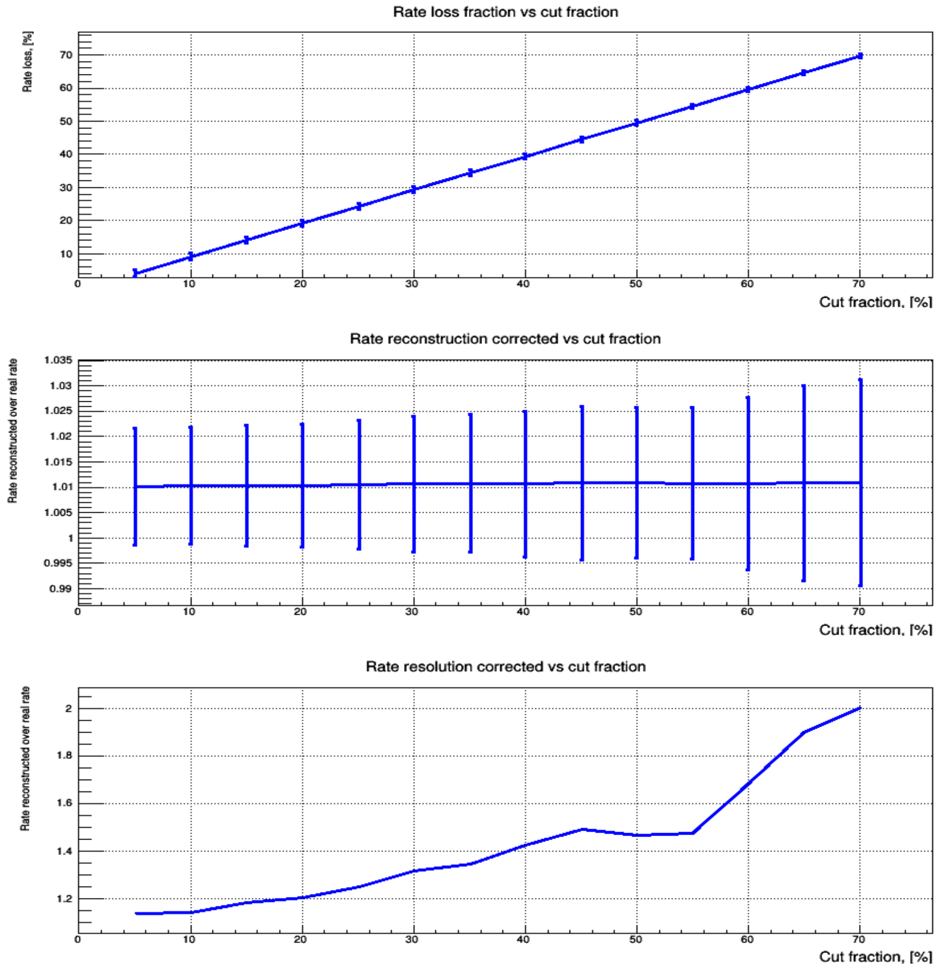

Figure D.4: *Rate reconstruction of an 8 mm positron beam. The detector is without mask. The sample is composed of 10^6 events.*

Bibliography

[1] Riccardo Barbieri, Lawrence Hall, and Alessandro Strumia. Hadronic flavor and CP-violating signals of superunification. *Nuclear Physics B*, 449(3):437 – 461, 1995. URL: `http://www.sciencedirect.com/science/article/pii/055032139500311F`, `doi:https://doi.org/10.1016/0550-3213(95)00311-F`.

[2] Riccardo Barbieri, Lawrence Hall, and Alessandro Strumia. Violations of lepton flavour and CP in supersymmetric unified theories. *Nuclear Physics B*, 445(2):219 – 251, 1995. URL: `http://www.sciencedirect.com/science/article/pii/055032139500208A`, `doi:https://doi.org/10.1016/0550-3213(95)00208-A`.

[3] Francesca Borzumati and Antonio Masiero. Large Muon- and Electron-Number Nonconservation in Supergravity Theories. *Phys. Rev. Lett.*, 57:961–964, Aug 1986. URL: `https://link.aps.org/doi/10.1103/PhysRevLett.57.961`, `doi:10.1103/PhysRevLett.57.961`.

[4] The MEG Collaboration. Search for the Lepton Flavour Violating Decay $\mu^+ \to e^+\gamma$ with the Full Dataset of the MEG experiment, 2016. `arXiv:1605.05081`.

[5] A.M. Baldini et al. The design of the MEG II experiment. *Eur. Phys. Journal C*, 78(380), 2016. URL: `https://doi.org/10.1140/epjc/s10052-018-5845-6`.

[6] A. Papa, G. Rutar, F. Barchetti, M. Hildebrandt, and P.-R. Kettle. A fast and quasi non-invasive muon beam monitor working at the intensity frontier. *Nucl. Instrum. Meth. A*, 936:634–635, 2019. `doi:10.1016/j.nima.2018.10.145`.

[7] Emanuele Ripiccini, Angela Papa, and Giada Rutar. High granularity scintillating fiber trackers based on Silicon Photomultiplier. page 009, 06 2016. `doi:10.22323/1.252.0009`.

[8] F. Rademakers R. Brun. ROOT — An object oriented data analysis framework. *Nuclear Instruments and Methods in Physics Research Section A: Accelerators, Spectrometers, Detectors and Associated Equipment*, 389(1-2):81 – 86, 1997. Frontier Detectors for Frontier Physics. URL: `https://www.sciencedirect.com/science/article/pii/S016890029700048X`, `doi:https://doi.org/10.1016/S0168-9002(97)00048-X`.

[9] David J Griffiths. *Introduction to elementary particles; 2nd rev. version*. Physics textbook. Wiley, New York, NY, 2008. URL: `https://cds.cern.ch/record/111880`.

[10] Peter W. Higgs. Broken Symmetries and the Masses of Gauge Bosons. *Phys. Rev. Lett.*, 13:508–509, Oct 1964. URL: `https://link.aps.org/doi/10.1103/PhysRevLett.13.508`, `doi:10.1103/PhysRevLett.13.508`.

[11] Yoshitaka Kuno and Yasuhiro Okada. Muon decay and physics beyond the standard model. *Rev. Mod. Phys.*, 73:151–202, Jan 2001. URL: `https://link.aps.org/doi/10.1103/RevModPhys.73.151`, `doi:10.1103/RevModPhys.73.151`.

[12] M. Tanabashi, K. Hagiwara, K. Hikasa, K. Nakamura, Y. Sumino, F. Takahashi, J. Tanaka, K. Agashe, G. Aielli, C. Amsler, M. Antonelli, D. M. Asner, H. Baer, Sw. Banerjee, R. M. Barnett, T. Basaglia, C. W. Bauer, J. J. Beatty, V. I. Belousov, J. Beringer, S. Bethke, A. Bettini, H. Bichsel, O. Biebel, K. M. Black, E. Blucher, O. Buchmuller, V. Burkert, M. A. Bychkov, R. N. Cahn, M. Carena, A. Ceccucci, A. Cerri, D. Chakraborty, M.-C. Chen, R. S. Chivukula, G. Cowan, O. Dahl, G. D'Ambrosio, T. Damour, D. de Florian, A. de Gouvêa, T. DeGrand, P. de Jong, G. Dissertori, B. A. Dobrescu, M. D'Onofrio, M. Doser, M. Drees, H. K. Dreiner, D. A. Dwyer, P. Eerola, S. Eidelman, J. Ellis, J. Erler, V. V. Ezhela, W. Fetscher, B. D. Fields, R. Firestone, B. Foster, A. Freitas, H. Gallagher, L. Garren, H.-J. Gerber, G. Gerbier, T. Gershon, Y. Gershtein, T. Gherghetta, A. A. Godizov, M. Goodman, C. Grab, A. V. Gritsan,

C. Grojean, D. E. Groom, M. Grünewald, A. Gurtu, T. Gutsche, H. E. Haber, C. Hanhart, S. Hashimoto, Y. Hayato, K. G. Hayes, A. Hebecker, S. Heinemeyer, B. Heltsley, J. J. Hernández-Rey, J. Hisano, A. Höcker, J. Holder, A. Holtkamp, T. Hyodo, K. D. Irwin, K. F. Johnson, M. Kado, M. Karliner, U. F. Katz, S. R. Klein, E. Klempt, R. V. Kowalewski, F. Krauss, M. Kreps, B. Krusche, Yu. V. Kuyanov, Y. Kwon, O. Lahav, J. Laiho, J. Lesgourgues, A. Liddle, Z. Ligeti, C.-J. Lin, C. Lippmann, T. M. Liss, L. Littenberg, K. S. Lugovsky, S. B. Lugovsky, A. Lusiani, Y. Makida, F. Maltoni, T. Mannel, A. V. Manohar, W. J. Marciano, A. D. Martin, A. Masoni, J. Matthews, U.-G. Meißner, D. Milstead, R. E. Mitchell, K. Mönig, P. Molaro, F. Moortgat, M. Moskovic, H. Murayama, M. Narain, P. Nason, S. Navas, M. Neubert, P. Nevski, Y. Nir, K. A. Olive, S. Pagan Griso, J. Parsons, C. Patrignani, J. A. Peacock, M. Pennington, S. T. Petcov, V. A. Petrov, E. Pianori, A. Piepke, A. Pomarol, A. Quadt, J. Rademacker, G. Raffelt, B. N. Ratcliff, P. Richardson, A. Ringwald, S. Roesler, S. Rolli, A. Romaniouk, L. J. Rosenberg, J. L. Rosner, G. Rybka, R. A. Ryutin, C. T. Sachrajda, Y. Sakai, G. P. Salam, S. Sarkar, F. Sauli, O. Schneider, K. Scholberg, A. J. Schwartz, D. Scott, V. Sharma, S. R. Sharpe, T. Shutt, M. Silari, T. Sjöstrand, P. Skands, T. Skwarnicki, J. G. Smith, G. F. Smoot, S. Spanier, H. Spieler, C. Spiering, A. Stahl, S. L. Stone, T. Sumiyoshi, M. J. Syphers, K. Terashi, J. Terning, U. Thoma, R. S. Thorne, L. Tiator, M. Titov, N. P. Tkachenko, N. A. Törnqvist, D. R. Tovey, G. Valencia, R. Van de Water, N. Varelas, G. Venanzoni, L. Verde, M. G. Vincter, P. Vogel, A. Vogt, S. P. Wakely, W. Walkowiak, C. W. Walter, D. Wands, D. R. Ward, M. O. Wascko, G. Weiglein, D. H. Weinberg, E. J. Weinberg, M. White, L. R. Wiencke, S. Willocq, C. G. Wohl, J. Womersley, C. L. Woody, R. L. Workman, W.-M. Yao, G. P. Zeller, O. V. Zenin, R.-Y. Zhu, S.-L. Zhu, F. Zimmermann, P. A. Zyla, J. Anderson, L. Fuller, V. S. Lugovsky, and P. Schaffner. Review of Particle Physics. *Phys. Rev. D*, 98:030001, Aug 2018. URL: `https://link.aps.org/doi/10.1103/PhysRevD.98.030001`, `doi:10.1103/PhysRevD.98.030001`.

[13] B. Pontecorvo. Mesonium and anti-mesonium. *Sov. Phys. JETP*, 6:429, 1957.

[14] Ziro Maki, Masami Nakagawa, and Shoichi Sakata. Remarks on the unified model of elementary particles. *Prog. Theor. Phys.*, 28:870–880, 1962. `doi:10.1143/PTP.28.`

870.

[15] Lorenzo Calibbi and Giovanni Signorelli. Charged Lepton Flavour Violation: An Experimental and Theoretical Introduction. *Riv. Nuovo Cim.*, 41(2):71–174, 2018. `arXiv:1709.00294`, `doi:10.1393/ncr/i2018-10144-0`.

[16] Daisuke Kaneko. Upgrade of the Liquid Xenon γ-ray detector in the MEG experiment. *Nuclear Instruments and Methods in Physics Research Section A: Accelerators, Spectrometers, Detectors and Associated Equipment*, 732:457 – 462, 2013. Vienna Conference on Instrumentation 2013. URL: `http://www.sciencedirect.com/science/article/pii/S0168900213008280`, `doi:https://doi.org/10.1016/j.nima.2013.06.008`.

[17] A.M. Baldini, E. Baracchini, L. Berretta, S. Bianucci, G. Cavoto, G. Chiarello, C. Chiri, F. Cei, A. Corvaglia, S. Dussoni, D. Fahrni, L. Galli, F. Grancagnolo, M. Grassi, A. Hofer, M. Hildebrandt, F. Ignatov, A. Miccoli, D. Nicolò, A. Orsini, M. Panareo, A. Pepino, C. Pinto, G. Piredda, G. Signorelli, F. Raffaelli, L. Recchia, F. Renga, E. Ripiccini, G. Tassielli, A. Tazzioli, F. Tenchini, M. Venturini, C. Voena, and A. Zullo. A new cylindrical drift chamber for the MEG II experiment. *Nuclear Instruments and Methods in Physics Research Section A: Accelerators, Spectrometers, Detectors and Associated Equipment*, 824:589 – 591, 2016. Frontier Detectors for Frontier Physics: Proceedings of the 13th Pisa Meeting on Advanced Detectors. URL: `http://www.sciencedirect.com/science/article/pii/S016890021501342X`, `doi:https://doi.org/10.1016/j.nima.2015.10.103`.

[18] Matteo De Gerone, Flavio Gatti, Wataru Ootani, Yusuke Uchiyama, M. Nishimura, S. Shirabe, Paolo Walter Cattaneo, and M. Rossella. Design and test of an extremely high resolution Timing Counter for the MEG II experiment: Preliminary results. *Journal of Instrumentation*, 9, 12 2013. `doi:10.1088/1748-0221/9/02/C02035`.

[19] Saint Gobain Crystals. *LYSO Scintillation Material. Lu1.8Y.2SiO5:Ce.* URL: `https://www.crystals.saint-gobain.com/sites/imdf.crystals.com/files/documents/lyso-material-data-sheet1.pdf`.

[20] Stefan Ritt. The DRS chip: cheap waveform digitizing in the GHz range. *Nuclear Instruments and Methods in Physics Research Section A: Accelerators, Spectrometers, Detectors and Associated Equipment*, 518(1):470 – 471, 2004. Frontier Detectors for Frontier Physics: Proceedin. URL: `http://www.sciencedirect.com/science/article/pii/S016890020302922X`, `doi:https://doi.org/10.1016/j.nima.2003.11.059`.

[21] (Geant4 collaboration) S.Agostinelli et al. Geant4–a simulation toolkit. *Nucl. Instrum. Methods A*, 506:250–303, 2003. URL: `https://doi.org/10.1016/S0168-9002(03)01368-8`.

[22] J. Allison et al. Geant4 developments and applications. *IEEE Trans. Nucl. Sci.*, 53:270–278, 2006. URL: `https://doi.org/10.1109/TNS.2006.869826`.

[23] J. Allison et al. Recent develpments in Geant4. *Nucl. Instrum. Methods A*, 835:186–225, 2016. URL: `https://doi.org/10.1016/j.nima.2016.06.125`.

[24] Christian Baumgarten, M. Seidel, A. Adelmann, Y.J. Bi, R. Doelling, Hansruedi Fitze, A. Fuchs, M. Humbel, J. Grillenberger, D. Kiselev, A. Mezger, Davide Reggiani, M. Schneider, Jianjun Yang, H. Zhang, and Tianjue Zhang. Production of a 1.3 MW proton beam at PSI. 06 2010.

[25] F. Berg et al. Target Studies for Surface Muon Production. *Phys. Rev. Accel. Beams*, 19(2):024701, 2016. `arXiv:1511.01288`, `doi:10.1103/PhysRevAccelBeams.19.024701`.

[26] G. Heidenreich. Carbon and Beryllium Targets at PSI. *AIP Conf. Proc.*, 642(1):122–124, 2002. `doi:10.1063/1.1522602`.

[27] A.E. Pifer, T. Bowen, and K.R. Kendall. A high stopping density μ^+ beam. *Nuclear Instruments and Methods*, 135(1):39 – 46, 1976. URL: `http://www.sciencedirect.com/science/article/pii/0029554X76908235`, `doi:https://doi.org/10.1016/0029-554X(76)90823-5`.

[28] Rafael Abela, F. Foroughi, and Dieter Renker. Muon beams at PSI. *Zeitschrift für Physik C Particles and Fields*, 56:S240–S242, 03 1992. `doi:10.1007/BF02426803`.

[29] J. Adam, X. Bai, A. Baldini, Elisabetta Baracchini, Carlo Bemporad, Gianluigi Boca, Paolo Walter Cattaneo, Gianluca Cavoto, Fabrizio Cei, C. Cerri, Matteo Corbo, N. Curalli, A. Bari, Matteo De Gerone, L. Frate, S. Doke, S. Dussoni, J. Egger, K. Fratini, and D. Zanello. The MEG detector for $\mu^+ \to e^+\gamma$ decay search. 03 2013.

[30] J.B. Birks. *The Theory and Practice of Scintillation Counting*. Pergamon Press, Oxford, 1964. URL: `https://scholar.google.com/scholar?q=Birks,+J.B.+(1964)+The+Theory+and+Practice+of+Scintillation+Counting.+Pergamon+Press,+Oxford`.

[31] W. R. Leo. *Techniques for Nuclear and Particle Physics Experiments: A How-to Approach*. Springer, 1992. URL: `https://scholar.google.com/scholar?hl=it&assdt=0%2C5&q=William+R.+Leo+-+Techniques+for+nuclear+and+particle+physics+experiments+%281992%29%2C+Springer&btnG=`.

[32] A. Einstein. Über einen dir Erzeugung und Versandlung des Lichtes betreffenden heuristischen Gesichtspunkt - Concerning an heuristic point of view toward the emission and transformation of light. *American Journal of Physics*, 33(5):1–16, 1905.

[33] Saint Gobain Crystals. *Plastic Scintillating Fibers*. URL: `https://www.crystals.saint-gobain.com/sites/imdf.crystals.com/files/documents/fiber-product-sheet.pdf`.

[34] Hamamatsu. *MPPC (Multi-Pixel Photon Countes) S13360 series*, 8 2016. URL: `https://www.hamamatsu.com/resources/pdf/ssd/s13360 serieskapd1052e.pdf`.

[35] Saint Gobain Crystals. *Detector Assembly Materials*. URL: `https://www.crystals.saint-gobain.com/sites/imdf.crystals.com/files/documents/detector-assembly-materials.pdf`.

[36] Particle Data Group. Atomic and Nuclear Properties of Materials, 2019. URL: `http://pdg.lbl.gov/2019/AtomicNuclearProperties/`.

[37] Zhang Jian-Fu, Ruan Xi-Chao, Hou Long, Li Xia, Bao Jie, Zhang Guo-Guang, Huang Han-Xiong, and Song Chao-Hong. Measurements of the light output functions of plastic scintillator using 9 Be(d, n) 10 B reaction neutron source. *Chinese Physics C*, 34(7):988–992, jul 2010. URL: `https://doi.org/10.1088%2F1674-1137%2F34%2F7%2F011`, `doi:10.1088/1674-1137/34/7/011`.

[38] Saint Gobain Crystals. *BC-400, BC-404, BC-408, BC-412, BC-416. Premium Plastic Scintillators.* URL: `https://www.crystals.saint-gobain.com/sites/imdf.crystals.com/files/documents/bc400-404-408-412-416-data-sheet.pdf`.

[39] Ankit Rohatgi. WebPlotDigitizer. URL: `https://automeris.io/WebPlotDigitizer/`.

[40] R. Ywai, A. Papa, E. Ripiccini, and G. Rutar. SciFi detectors, Scintillating Fibers - Mass quality checks, MEG collaboration Meeting, Tokyo, 03 2016. URL: `https://indico.psi.ch/event/4597/contributions/9001/attachments/8339/10636/SciFiDetectorsAttenuationLengthTokyoMarch2016.pdf`.

[41] Huangshan Chen. *A Silicon Photomultiplier Readout ASIC for the Mu3e Experiment.* PhD thesis, U. Heidelberg (main), 2018. `doi:10.11588/heidok.00024727`.

[42] Patrick Eckert, Hans-Christian Schultz-Coulon, Wei Shen, Rainer Stamen, and Alexander Tadday. Characterisation studies of silicon photomultipliers. *Nuclear Instruments and Methods in Physics Research Section A: Accelerators, Spectrometers, Detectors and Associated Equipment*, 620(2-3):217–226, Aug 2010. URL: `http://dx.doi.org/10.1016/j.nima.2010.03.169`, `doi:10.1016/j.nima.2010.03.169`.

[43] Hamamatsu Corporation New Jersey Institute of Technology Slawomir S. Piatek. Physics and Operation of an MPPC. 2 2014.

[44] F. Corsi, A. Dragone, C. Marzocca, A. [Del Guerra], P. Delizia, N. Dinu, C. Piemonte, M. Boscardin, and G.F. [Dalla Betta]. Modelling a silicon photomultiplier (SiPM) as a signal source for optimum front-end design. *Nuclear Instruments and Methods in Physics Research Section A: Accelerators, Spectrometers, Detectors and Associated Equipment*, 572(1):416 – 418, 2007. Frontier Detectors for Frontier Physics. URL: `http://www.sciencedirect.com/science/article/pii/S0168900206021449`, `doi:https://doi.org/10.1016/j.nima.2006.10.219`.

[45] K. Kobayashi A. Ghassemi, K. Sato. *MPPC technical notes.* Hamamatsu, 3 2017. URL: `https://www.hamamatsu.com/resources/pdf/ssd/mppc kapd9005e.pdf`.

[46] Ignazio Vilardi, A. Braem, E. Chesi, F. Ciocia, N. Colonna, Francesco Corsi, F. Cusanno, R. De Leo, Angelo Dragone, F. Garibaldi, C. Joram, L. Lagamba, S. Marrone, E. Nappi, Jacques Seguinot, Giuseppe Tagliente, Antonio Valentini, Peter Weilhammer, and Habib Zaidi. Optimization of the effective light attenuation length of YAP:Ce and LYSO:Ce crystals for a novel geometrical PET concept. *Nuclear Instruments and Methods in Physics Research Section A: Accelerators, Spectrometers, Detectors and Associated Equipment*, 564:506–514, 08 2006. `doi:10.1016/j.nima.2006.04.079`.

[47] Aarti Kriplani, S. P. Stoll, David J. Schlyer, S. K. Sadat Shokouhi, Paul Vaska, A. Jr. Villanueva, and C. Woody. Light output measurements of LSO single crystals and 4×8 arrays: comparison of experiment with Monte Carlo simulations. *2003 IEEE Nuclear Science Symposium. Conference Record (IEEE Cat. No.03CH37515)*, 5:3036–3040 Vol.5, 2003.

[48] Saint Gobain Crystals. *BC-600 Optical Cement.* URL: `https://www.crystals.saint-gobain.com/sites/imdf.crystals.com/files/documents/bc600-data-sheet.pdf`.

[49] J. Spuller, D. Berghofer, M.D. Hasinoff, R. Macdonald, D.F. Measday, M. Salomon, T. Suzuki, J.-M. Poutissou, R. Poutissou, and J.K.P. Lee. A remeasurement of the Panofsky ratio. *Physics Letters B*, 67(4):479 – 482, 1977. URL: `http://www.`

sciencedirect.com/science/article/pii/037026937790449X, doi:https://doi.org/10.1016/0370-2693(77)90449-X.

[50] A. Papa. Search for the Lepton Flavour Violation in $\mu^+ \to e^+\gamma$. The calibration methods for the MEG experiment. 2009.

[51] Geant4 collaboration. Geant4 Material Database, 2018. URL: http://geant4-userdoc.web.cern.ch/geant4-userdoc/UsersGuides/ForApplicationDeveloper/html/Appendix/materialNames.html.